THESIS

This is to certify that the

thesis entitled

AN EXPERIMENTAL STUDY OF BLADE-TO-BLADE
STATIC PRESSURE DIFFERENCES AND
OPERATING CHARACTERISTICS OF A CENTRIFUGAL COMPRESSOR

presented by

NEIL WHITBECK

has been accepted towards fulfillment
of the requirements for

M.S. degree in MECHANICAL ENGINEERING

Major professor

Date 04-04-94

AN EXPERIMENTAL STUDY OF BLADE-TO-BLADE PRESSURE DIFFERENCES AND OPERATING CHARACTERISTICS OF A CENTRIFUGAL COMPRESSOR

By

Neil Glenn Whitbeck

A THESIS

Submitted to
Michigan State University
in partial fulfillment of the requirements
for the degree of

MASTER OF SCIENCE

Department of Mechanical Engineering

1994

ABSTRACT

AN EXPERIMENTAL STUDY OF BLADE-TO-BLADE PRESSURE DIFFERENCES AND OPERATING CHARACTERISTICS OF A CENTRIFUGAL COMPRESSOR

By

Neil Glenn Whitbeck

A centrifugal compressor with a 10+10, radial-outlet impeller and vaned diffuser was run at N_{red}=10,000 rpm, 12,000 rpm, 14,000 rpm, and 16,500 rpm. Measurements of shroud-side static pressures were obtained, together with temperature and pressure readings at rotor outlet and stage exit for several operating points for both normal and unsteady operation. Characteristic performance data for the normal operation were plotted to show variations in stagnation pressure rise and efficiency for the rotor and the stage. Stable operation was also characterized by plotting blade-to-blade pressure oscillation amplitudes against flowrate and meridional position. Such plots provided convenient formats for possibly tracking the extent of reverse flow through impeller passages. In addition, unstable operation was characterized according to instability type (rotating stall or surge), stall zone number, and stall velocity.

ACKNOWLEDGMENTS

From February to August 1993, I participated in a student exchange between the *Institut für Strömungsmaschinen , Universität Hannover* (Hannover, Germany) and Michigan State University's Department of Mechanical Engineering (E. Lansing, Michigan, USA). This thesis grows out of the work I performed in Germany. I thank Dr. A. Engeda and Dr. J. Lloyd for facilitating the student exchange. I especially thank Prof. Dr.-Ing. M. Rautenberg for his invitation to me to study at the *Institut* and for his gracious hospitality once I arrived.

I also thank Dipl.-Ing. U. Seidel, who acted as guide and counselor through my entire tenure at the *Institut.* Without his patience and guidance, this work could never have been produced. Most of what I know about flow instabilities in centrifugal compressors, I learned from him. Thanks also go to Dr.-Ing. D. Jin and Dr.-Ing. U. Haupt. Dr. Jin offered valuable instruction on the experimental detection and characterization of rotating stall and surge. Dr. Haupt helped deepen my conceptual understanding of these phenomena.

Messrs. Seidel, Weber, Clevenot, and Wichmann gave me hands on training with data acquisition and analysis equipment. Mr. Tanneberg ran the compressor rig. I thank them all.

I wish to thank my thesis examiners: Drs. A. Engeda, J. McGrath, and M. Koochesfahani. I also appreciate the support of the German Research Association (DFG) for the support of this research.

TABLE OF CONTENTS

LIST OF TABLES

LIST OF FIGURES

NOMENCLATURE

Symbol	Signification	Dimensions
AR	Area ratio $AR = \frac{A_5}{A_4}$	[-]
AS	Diffuser channel throat aspect ratio	[-]
b	Impeller blade height (hub to tip)	[m]
b_i	Average impeller width	[m]
c	Absolute velocity	[m/s]
D	Diameter	[m]
D_f	Diffusion factor $D_f = \left[1 - \frac{w_{2,avg}}{w_{1,rms}}\right] + \left[\frac{\pi \cdot r_2 \cdot \mu \cdot u_2}{Z \cdot s \cdot w_{1,rms}}\right] + 0.1\left(\frac{b_i}{r_s}\right) + \left[1 + \frac{w_{2,avg}}{w_{1,rms}}\right]$	[-]
f, *f*	Frequency	[Hz]
h	Enthalpy	[kJ/kg]
h	Diffuser channel width	[m]
l_{ax}	Axial length of blade	[m]
L	Diffuser blade length	[m]
LWR	Length to width ratio $LWR = \frac{L}{h_4}$	[-]
m	Number of stall cells	[-]
m, $\dot{m}$	Mass flowrate	[kg/s]
m_{red}	Reduced mass flowrate $m_{red}=[T_K/288K]\cdot m$	[kg/s]
N	Shaft rotational speed	[rev/min]
N_{red}	Reduced shaft speed $N_{red}=[288K/T_K]^{0.5}\cdot N$	[rev/min]
P, p	Static Pressure	[Pa]

Symbol	Signification	Dimensions
p_b	Blade-to-blade static pressure difference	[Pa]
P_o	Stagnation Pressure	[Pa]
phi	Flow coefficient (Mizuki, 1976) $\text{phi} = \left(\frac{c_r}{u}\right)_2$	[-]
PR	Pressure ratio	[-]
Q	Volumetric flowrate	[m^3/s]
r	Radius	[m]
r_s	Mean radius of curvature	[m]
s	Blade length along tip	[-]
T	Temperature	[K]
T	Period (1/f)	[s]
T_o	Stagnation Temperature	[K]
u	Blade velocity	[m/s]
w	Relative velocity	[m/s]
x	Distance from blade leading edge along blade tip	[m]
Z	Number of impeller blades	[-]
β	Blade angle or relative fluid angle	[deg]
ϕ	Flow coefficient $\phi = \left[\frac{4V}{\pi D_2^2 u_2}\right]$	[-]
ϕ_g	Circumferential position of transducer	[deg]
$\Delta\phi_{st}$	Phase angle between two pressure signals	[deg]
η	Efficiency	[-]
λ	Diffuser radius ratio $\lambda = \frac{D_3}{D_2}$	[-]
π	Pressure ratio	[-]
ρ	Fluid density	[kg/m^3]
μ	Slip factor	[-]
ω	Rotational speed	[rad/s]
ω	Rotational velocity	[rad/s]
Ω	Shaft rotational speed	[rad/s]

Symbol	Signification	
ψ_b	Blade-to-blade pressure coeff.	[-]

$$\psi_b = \left(\frac{2p_b}{\rho_1 u_2^2} \right)$$

Subscripts and Superscripts

abs	in the absolute frame
atm	atmospheric
avg	average
b	of the blade(s), of the blade passes
isen	isentropic
K	of settling chamber
m	midway between hub and shroud
p	of the pressure
r	radial component
rel	in the relative frame
rel/abs	of the relative frame with respect to the absolute frame
rms	root-mean-square average
s	at shroud
s	of the shaft
st	of the rotating stall
tot	total or stagnation value
1	at rotor inlet
2	at rotor exit
3	at leading edge of diffusor vanes
4	at diffuser vane channel throat
5	at trailing edge of diffusor vanes

CHAPTER 1--INTRODUCTION

1.1 Scope of Work

Characterizing machine operation beyond simple performance curves can prove difficult to investigators interested in developing a deeper understanding of flow phenomena and operational characteristics of centrifugal compressors. The following study seeks to characterize the operation of a centrifugal compressor running at N_{red}=10,000, 12,000, 14,000, and 16,500 rpm during both normal and unstable operation. Over the normal operating range--from the choking limit to the point where significant instabilities are felt--blade-to-blade static pressure oscillations at the shroud are evaluated to determine if they provide a reliable means for tracking reverse flow in impeller channels. At the instability limits, FFT analyses are performed using both a bench top analyzer and signal analysis software to determine the character of instabilities felt.

Blade-to-blade static pressure difference data were obtained using a bench top FFT analyzer for several positions along the meridional extent of the shroud for several operating points. These data were then processed and displayed three-dimensionally as blade-to-blade static pressure difference amplitudes versus both flowrate and meridional position. This provided a convenient way of detecting trends in blade-to-blade pressure differences and assessing the possibility of tracking reverse flow along the shroud wall by means of its effect on these pressure differences.

Using a bench top FFT analyzer to capture and analyze instabilities at part load operation proved much more difficult. Surge events and instances of intermittent rotating stall occur for very brief periods (approximately 125 rotor rotations) before dying out. Analyzing these events using a bench top FFT analyzer required the investigator to correctly guess the advent of stall and activate analyzer scanning within a very narrow time window to produce meaningful results on the analyzer. This method proved cumbersome and difficult. Therefore, in addition to analyses using the bench top analyzer, static pressure and blade vibration signals were digitized and analyzed using signal analysis software. The software approach offered a convenient way to conduct analyses into the character of the specific instabilities encountered. The resulting characterizations of rotating stall found at 14,000 rpm extended the findings of Seidel, et al. (1991b) and revealed the presence of instabilities giving rise to unusual blade vibration characteristics.

1.2 Rotating Stall and Surge in Centrifugal Compressors

1.2.1 Rotating Stall

Rotating stall is a flow phenomenon characterized by rotating circumferential distortions in the flow field. Such distortions are marked by equidistant rotating zones (stall cells) of low flow surrounded by zones of relatively high flow, as shown schematically in Figure 1.1. [Note: In Figure 1.1, cell rotational sense is indicated for rotation of cells in a coordinate frame rotating with the shaft.] In rotating stall, flow in impeller passages takes turns stalling, then recovering. Specific instances of rotating stalls are usually characterized by the number of stall cells they contain

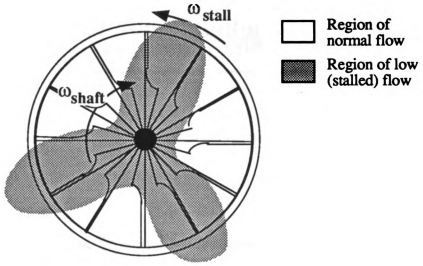

Fig.1.1. Rotating stall pattern with m=-3

(m), the rotational sense of these cells (m<0 against impeller rotation; m>0 with the impeller rotation), and their propagational speed (ω_{st}/Ω). In contrast to surge, which can be marked by massive system flow reversals, the time-mean mass flow through the compressor does not drop when the compressor operates under rotating stall (Fringe & Van Den Braembussche, 1983).

At a set flowrate, rotating stall may emerge as an intermittent series of local, low frequency static pressure oscillations or it may occur continuously. Figure 1.2 schematically illustrates the difference between these two modes of rotating stall. Static pressure patterns for the normal flow show only sawtooth signals produced by blade passes. However, rotating stall produces the roughly sinusoidal pressure oscillations shown. This investigation found instances of intermittent rotating stall for operation at N_{red}=14,000 rpm. Intermittent rotating stall often precedes continuous rotating stall or surge.

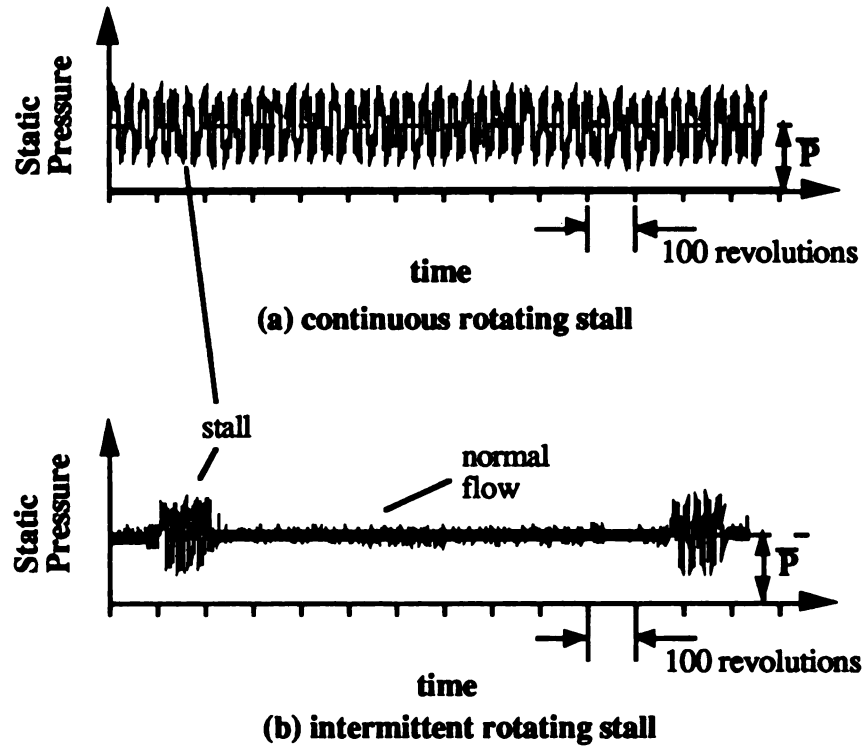

Fig. 1.2. Continuous and intermittent rotating stall

The precise physical mechanisms instigating and controlling rotating stall in centrifugal compressors are not well known. For axial machines, authors most frequently explain the propagation of stall cells around the inlet annulus as arising from boundary layer separation and excessive incidence at the leading edge of blade leading edges.

According to this model, perturbations in incoming flow approaching the leading edges of inducer blades at excessive incidence cause a group of blades to stall, as depicted in Figure 1.3. This stall acts to block the incoming flow and divert it to nearby flow passages. As a result, flow incidence with the blades on one side of the blocked cell increases; while on the other side, incidence drops. Blades with the increased incidence will tend to stall, while the previously stalled blades will tend to recover. In this way, the stall cell moves to a new location in the direction

for which blade incidence was increased. Cells always propagate at speeds less than the rotational speed of the rotor. Experimental evidence suggests that rotating stall in centrifugal machines is much more complex than that occurring in axial machines (Pampreen, 1993).

Although the exact mechanisms controlling the inception and character of rotating stall remain largely unexplained, it appears that rotating stall in centrifugal compressors can result from destabilization of flow in either the rotor or the diffuser. The former is called impeller rotating stall; the latter is called diffuser rotating stall. For impeller rotating stall, pressure fluctuations occur throughout the entire meridional extent of blade channels. Kämmer & Rautenberg (1985) report maximum pressure fluctuations occurring at x/s=0.8.

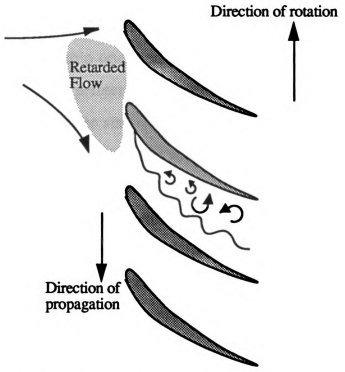

Fig. 1.3. Propagation of stall cell in axial compresso
(from Pampreen, 1993)

Authors usually suggest that impeller rotating stall results from boundary layer separation either at the inducer inlet, along impeller blades, or along either the hub or shroud walls (Chen, et al., 1989). Flow separation serves to block the forward flow of fluid, thereby producing cells of stalled flow. When boundary layer separation occurs progressively as flow rate is reduced, the resulting stall is called progressive stall. Progressive stall is usually marked by relatively mild velocity fluctuations and smooth variation in velocity fluctuation amplitude with flowrate (Fringe & Van Den Braembusche, 1983). In contrast, abrupt stall occurs much more abruptly and is marked by relatively strong velocity fluctuations.

Lennemann & Howard (1970) provided experimental evidence of how boundary layer separation can produce stall in impeller passages. They used the hydrogen bubble technique to visualize stall patterns produced in pump passages with the pump operated at part load. The patterns drawn in Figure 1.4 in four passages reflect the sequence of events occurring in a single passage during impeller stall. First, boundary layer separation occurs on the pressure side of the blade with subsequent backflow strongly supported by eddying (1). It appears that clearance flow passing over the blade to the adjoining suction side helps stagnate flow on the pressure side, leading to boundary layer separation. Relative eddies then block flow through the passage (2) causing flow to move out of the passage into the inlet (3). Hence, over part of the cycle, the passage acts briefly as a turbine passage. During recovery, the suction side may separate briefly (4). For shrouded impellers, Lennemann & Howard found the patterns to differ from that described above. However, both patterns showed the occurrence of flow separation, followed by blocked flow and regurgitation into the

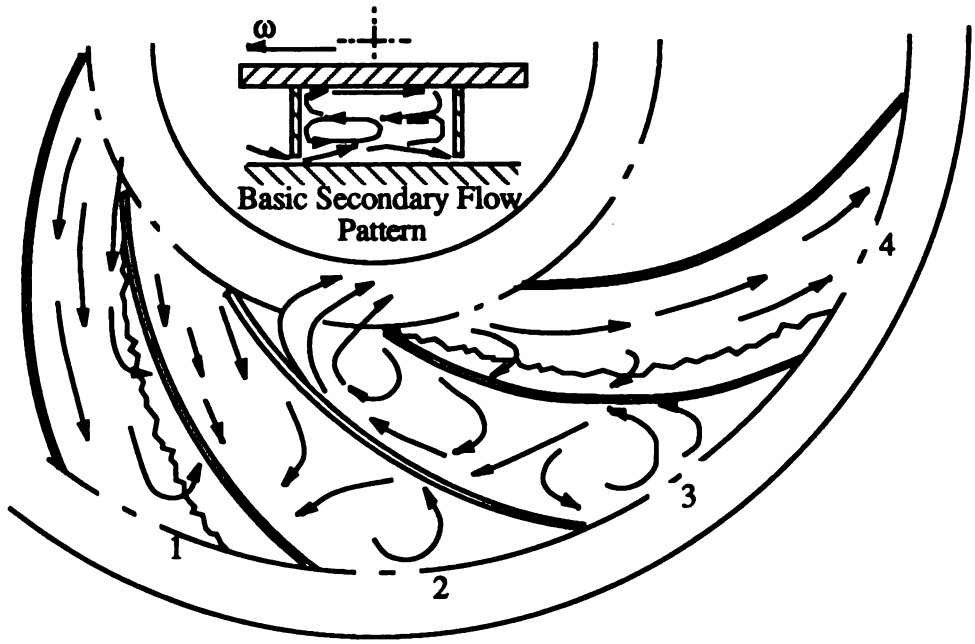

Fig. 1.4. Sequence of passage stall for an unshrouded impeller,
(from Lennemann & Howard, 1970)

impeller inlet. Pressure ratio usually rises as flowrate drops in centrifugal turbomachines. As flowrate drops, pressure gradients increase until a point is reached where boundary layers separate.

Diffuser rotating stall has been explained as resulting from the interaction between unsteady boundary layers along diffuser walls and the inviscid core flow. The boundary layers presumably provide perturbations that induce a hydrodynamic instability in the diffuser core flow. (Fringe & Van Den Braembussche, 1983; Kämmer & Rautenberg, 1985). In vaneless diffusers, stall is always associated with a reversal in the radial component of diffuser flow and with three-dimensional boundary layer separation. However, no one knows how rotating stall is initiated from the separation ring. For vaned diffusers, conditions in the semi-vaneless space appear to initiate stall. In this area, both increasing static pressure recovery and increasing diffuser vane incidence with decreasing flowrates have been

implicated in the initiation of stall. Also, rotating stalls initiated in vaned diffusers rotate opposite to rotor rotation (Pampreen, 1993).

The location of rotating stall inception appears related to the operating conditions of a compressor. Fringe & Van Den Braembussche (1983) found that initiation of impeller rotating stall will completely suppress diffuser rotating stall. However, diffuser rotating stall does not automatically suppress impeller rotating stall arising from critical inducer incidence. Kämmer & Rautenberg (1985), taking inducer incidence angle and diffuser inlet flow angles as stall criteria, constructed Figure 1.5. As illustrated in the figure, they predict that at low rotational speeds, the inducer determines stall limit. As speed increases, the diffuser load increases until it eventually becomes the critical component.

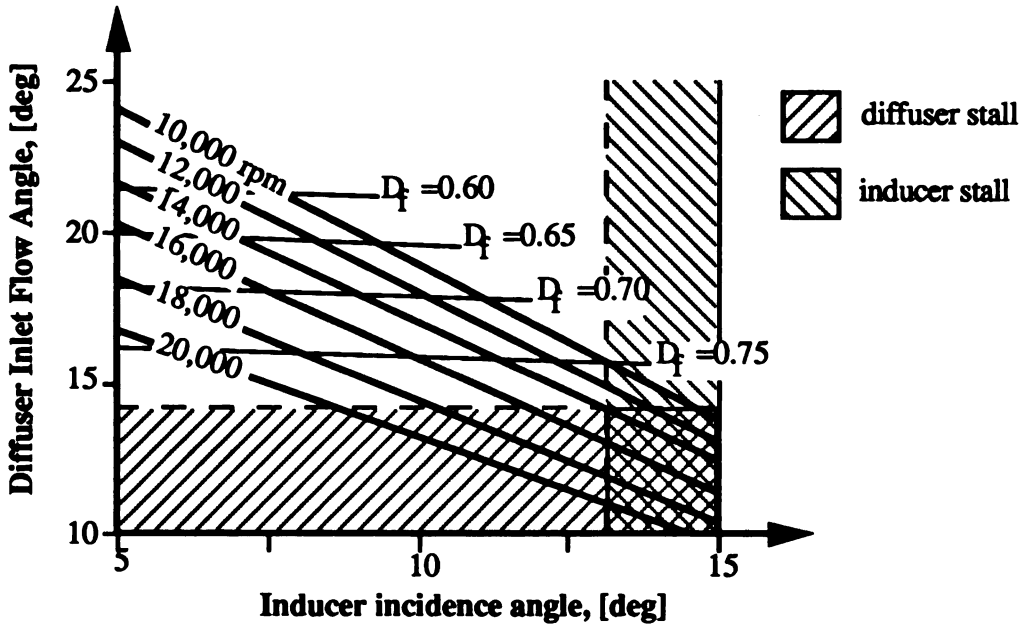

Fig. 1.5. Influence of Rotor Speed on Critical Stage Element
(from Kämmer & Rautenberg, 1985)

Table 1.1 Reported Rotating Stalls (Vaneless Diffusers)

Authors	u_2 [m/s]	Lobe Number	ω_2/Ω	Attributed to
Kubo & Murata (1976)	30.7	+1	0.25-0.3	
Fringe &	43.5-130.5	+4, +5	0.15	Rotor
Van Den	43.5-130.5	+1, +2, +3	0.25-0.3	Rotor
Braembussche (1983)	43.5-130.5	+1 (with harmonics of +2 & +3)	0.5-0.8	Rotor
	43.5-130.5	+2	0.13-0.16	Diffuser
	43.5-130.5	+3	0.17-0.21	Diffuser
Ariga, et al.	54.2	-1, -2, -3	0.435	Rotor
(1986)	54.2	-3, -4	0.625	Rotor
	54.2	-4	0.667	Rotor
	54.2	-1	0.333	Diffuser
Mizuki, et al. (1978)	60.8		0.48-1.0	
Ligrani, et al. (1982)	136	2	0.23	
Kämmer & Rautenberg (1982)	293	2	0.44	Rotor
Kämmer &	293	(varied)	0.89	Rotor
Rautenberg	314	+3	0.128	Diffuser
(1985)	335	+3	0.155	Diffuser
Haupt, et al.	335	-2		0.039
(1988)	335	+3	0.159	

Table 1.2 Reported Rotating Stalls (Vaned Diffusers)

Authors	u2 [m/s]	Lobe Number	ω2 /Ω	Diffuser Geometry
Roth (1992)	146	2, 3		Cambered Airfoil
Haupt, et al. (1990)	168	+5	0.015	Twisted Vane
	168	+6	0.035	Twisted Vane
	189	+5	0.021	Twisted Vane
	189	+6	0.035	Twisted Vane
	226	+4	0.01	Twisted Vane
	226	+5	0.02	Twisted Vane
	293	-2	0.22	Twisted Vane
	304	-2	0.15	Cambered Airfoil
	262	-3	0.06	Straight Channel
Abdel-Hamid, et al. (1987)	226-283	-3	0.04-0.06	Cambered Airfoil
	304	-2	0.11-0.17	Cambered Airfoil
Seidel, et al. (1991a,b)	251	-3	0.026-0.29, 0.047, 0.067	Cambered Airfoil
	251	+4	0.052	Cambered Airfoil
	251	+5	0.068-0.084	Cambered Airfoil
	251	+6	0.050, 0.097	Cambered Airfoil
	251	-2	0.129, 0.146	Cambered Airfoil
	251	-4	0.013	Cambered Airfoil
	251	+7	0.03-0.09	Cambered Airfoil
	293	-2	0.129-0.231	Cambered Airfoil
	293	-3	0.020	Cambered Airfoil
	293	-4	0.013	Cambered Airfoil
	293	+4	0.05	Cambered Airfoil
	293	+5	0.014	Cambered Airfoil
	293	+6	0.042-0.092	Cambered Airfoil
	335	-2	0.098, 0.18	Cambered Airfoil
	335	+5	0.034	Cambered Airfoil
Haupt, et al. (1988)	260-283	-3	0.04-0.06	Cambered Airfoil
	283-304	-2	0.15-0.17	Cambered Airfoil
	272-304	-2	0.157-0.214	Straight Channel
	226-262	-3	0.061-0.096	Straight Channel
	226-272	-4	0.01-0.02	Straight Channel

Experimental investigations have revealed the existence of rotating stalls of varying character, including stalls of different lobe number occurring in series at a single operating point (Haupt, et al, 1986, 1988). Investigators have reported rotating stalls composed of from one to seven cells occurring in centrifugal compressors. Generally, stall cell speed lies well under the rotational speed of the impeller, particularly with high lobe numbers. For centrifugal compressors outfitted with vaneless diffusers, Haupt, et al. (1988) have also established the occurrence of non-rotating pressure oscillations occurring at the same point where rotating stalls have occurred. Tables 1.1 and 1.2 list rotating stalls reported by researchers.

1.2.2 Surge

In contrast with rotating stall, surge produces significant flowrate fluctuations in the entire system. The amplitude of flowrate fluctuations can vary. In deep surge, the pressure differences between compression system inlet and system outlet are sufficiently great to force the fluid in the reverse direction through the machine. Compressor surging sometimes causes the entire compression system and foundation to vibrate and can result in serious damage. Whereas most axial compressors manifest rotating stall behavior before surge occurs, centrifugal compressors often start surging without preliminary rotating stall. This is particularly true for centrifugal compressors operating at high speeds (Wachter & Rohne, 1984).

Surge occurs in a cycle, which includes a breakdown in pressure rise and reduction in mass flow through the compressor, followed by a phase of pressure recovery with an increase in mass flow up to the initial point of departure. The cycle then begins again. The operating point for a compressor in surge thus describes a hysteresis loop such as those

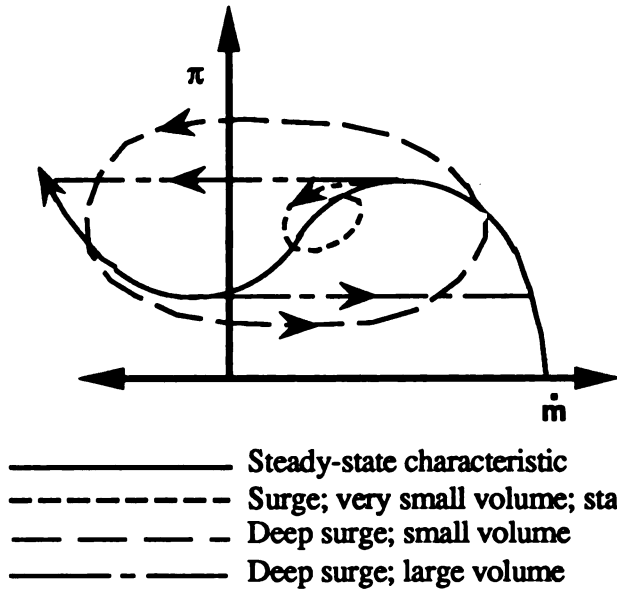

Fig. 1.6. Simplified surge paths and their variation with connected discharge volume,
(adapted from Wachter & Rohne, 1984)

illustrated in Figure 1.6. The size of these hysteresis loops gives some indication of the intensity of particular instances of surge. When flowrate variation is dramatic, the operating point traces a large loop as shown. In contrast, surge may be so mild that the operating point merely circles around the top of the performance curve. Generally, surge intensity increases with increases in stage pressure ratio (Cumpsty, 1989).

The frequency of flow fluctuations associated with surge usually lies below those for velocity fluctuations associated with rotating stall. The time scale associated with rotating stall depends on the propagational speed of stall cells. However, the time scale associated with surge depends on the size of the compressor exhaust volume. The larger the discharge volume of the compressor system, the larger the time scale for surge (i.e., the lower the surge frequency). Figure 1.6 shows the influence of discharge volume on operating point behavior under surge.

Surge usually occurs due to flow instabilities when the compression system is operating near maximum pressure ratios for a given rotor speed. Two such instabilities include (1) abrupt stall and (2) progressive stall. Surge resulting from abrupt stall generally produces violent flow reversals and is audible. Abrupt stall results in a sudden, apparently discontinuous drop in the compressor pressure rise and efficiency. It appears that single cell rotating stall patterns correlate with the occurrence of abrupt surge. Alternately, surge due to progressive stall is relatively mild and frequently inaudible. It gradually reduces stage pressure ratio and efficiency with decreasing flowrate. It appears that multi-cell rotating stall patterns correlate with the occurrence of surge due to progressive stall (Pampreen, 1994).

Studies concerning the nature of centrifugal compressor surge have demonstrated that surge consists almost entirely of rotating stall events of m=+1 (Jin, et al., 1992b). Brief periods of other modes of rotating stall may immediately precede surge but not in every case. For example, Jin, et al. (1992b) report finding m=+5 and +6 rotating stalls immediately preceding surge events at N_{red}=10,800 rpm and 8,000 rpm respectively and m=-2 stalls preceding surge events at N_{red}=14,000 rpm and 14,500 rpm. However, for operating speeds between 8,000 and 14,000 rpm they found no instances of rotating stall preceding surge.

1.3 Relation between Reverse Flow and Rotating Stall

Chen, et al. (1987; 1989; 1991a,b,c; 1992) has proposed that rotating stall be explained in terms of Rossby waves, which link baroclinic instabilities through secondary reverse flows in impeller channels. According to this model, and verified by Haupt, et al. (1987b), reverse flow travels as vortex filaments from the impeller outlet along the suction

surface/shroud side corner. At the inlet, it turns over the leading edge of the blade in the direction of the impeller rotation and into the adjoining impeller channel. There it joins the forward flow, traveling along the pressure surface/hub side corner. A free-swirl flow field arising on the suction surface of the blade in the rotating stall cell then allows the pressure gradient at the impeller outlet to bend fluid exiting from the pressure/hub corner over the blade trailing edge. This fluid then travels back down the adjoining impeller passage as the secondary reverse flow, as explained.

Briefly, rotating stall occurring in machines with vaned diffusers (as in the present investigation) is explained as follows. As a result of flow reversal at the outlet plane of the impeller channel, the flow in the semi-vaneless annular space between impeller outlet and diffuser vane inlet has non-uniform temperature and velocity fields. The same occurs at the impeller inlet, where reverse flow meets the low temperature/low entropy incoming flow. These temperature non-uniformities result in a baroclinic wave for each of these regions. These two baroclinic waves are linked together by rotating Rossby waves through the impeller channels. Karman vortices as lows and highs reside on the flanks of the Rossby waves. The Karman vortex "lows" travel with the Rossby waves and represent the active cells of rotating stall. Figure 1.7 shows the Rossby wave pattern, together with vortex lows and highs (cyclones and anticyclones).

The occurrence and character of rotating stall patterns does appear to correlate with the existence and character of reverse flow in some cases. During the occurrence of rotating stall in a compressor with vaned diffuser, Haupt, et al. (1988) conducted oil injection experiments and verified the existence of reverse flow originating near the impeller outlet.

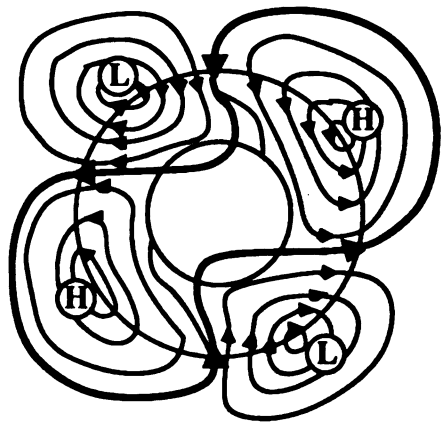

Fig. 1.7 Velocity pattern of Rossby waves together with vortices highs (H) and lows (L),
(adapted from Chen, et al., 1991)

They found that for a 2-cell pattern, reverse flow extended to the leading edge of the splitter blades. With 3-cell rotating stall, the reverse flow extended all the way to the inducer inlet and mixed with the forward flow there. As evidence of reverse flow associated with the inception and occurrence of rotating stall, Chen, et al. (1988) present blade-to-blade pressure variation data extracted from Mizuki, et al. (1976) for x/s=0.7.

Figure 1.8 represents the pressure-time traces presented by Chen, et al. (1988) for four different flowrates and operation at N=4150 rpm. Pressure-time data for the highest flowrate (the design flowrate) shows sharp pressure pulses residing along the suction sides of the signal. Chen, et al. interpret this to represent the high-pressure fluid from the outlet annulus passing through the core of the reverse flow vortex tube. As flowrate drops, the sharp pressure pulse disappears. Instead, the average pressure increases, and the blade-to-blade pressure differences diminish. Chen, et al. interprets this as an indication that the vortex tube, formerly restricted to the shroud/suction side corner for φ_m=0.330, widens over the

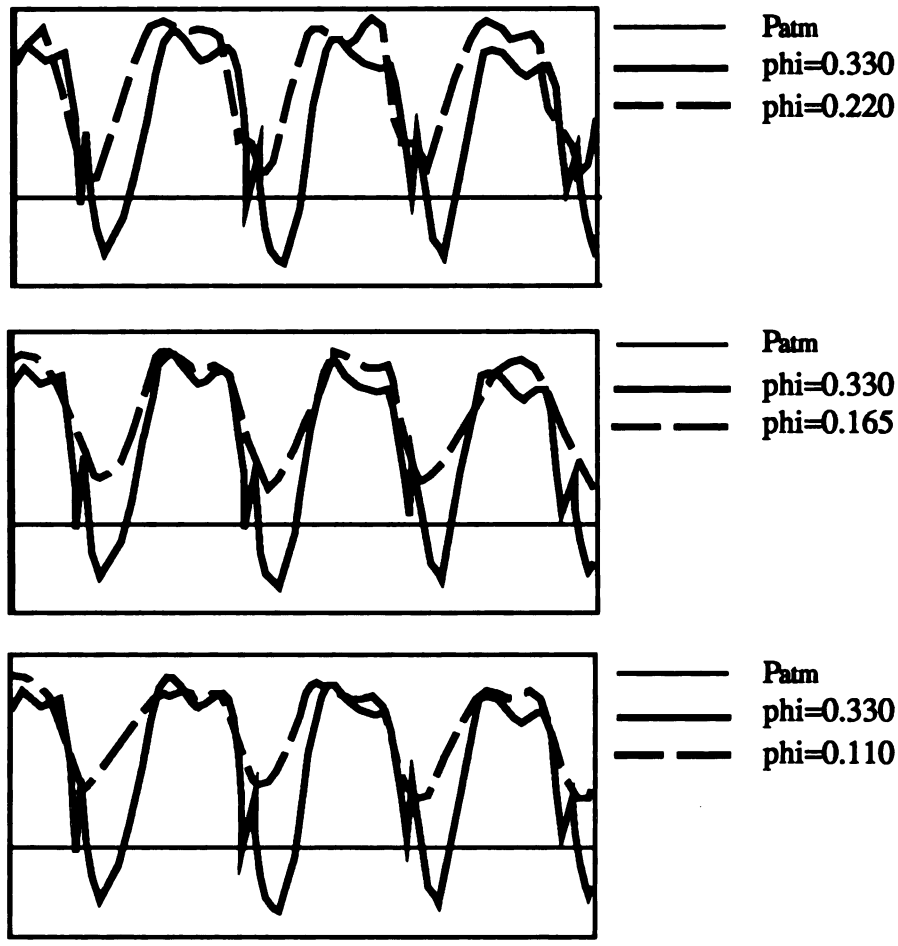

Fig. 1.8. Pressure-time signal for various flowrates,
(adapted from Chen, et al., 1988)

entire surface of the shroud. Figure 1.9 shows how blade-to-blade pressure differences vary as flowrate drops for this data. As flowrate drops, reverse flow not only widens, but also penetrates further upstream, apparently triggering rotating stall once it reaches the blades' leading edges (Haupt, et al.,1988).

The linkage between reverse flow and blade-to-blade pressure difference variations is not conclusive. Nevertheless, Chen, et al.'s interpretation of Mizuki's data suggests that under conditions of reverse flow, the blade-to-blade static pressure rise will drop as flowrate is reduced. Furthermore, their analysis indicates that as flowrate drops and reverse flow intensity increases, the influence of the reverse flow should be felt further and further upstream in the impeller passages. If this occurs, then it should be possible to track reverse flow from the rotor exit along the shroud wall by tracking the meridional positions over which a drop in blade-to-blade static pressure difference occurs.

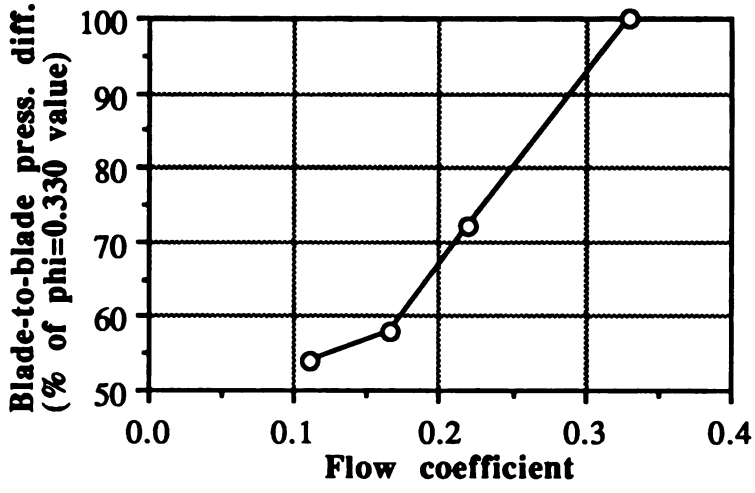

Fig. 1.9. Blade-to-blade pressure variation with flow, x/s=0.7 (adapted from Chen, et al. 1988)

CHAPTER 2--EXPERIMENTAL EQUIPMENT

2.1 Compressor Test Facility

Pressure measurements were taken for a single-stage compressor with the basic dimensions shown in Figure 2.1. The compressor was driven by a 1350 kW DC-motor coupled to a gear box with a shaft speed ratio of 1:16.2. Readers unfamiliar with centrifugal compressors are encouraged to view the contents of Appendix A.

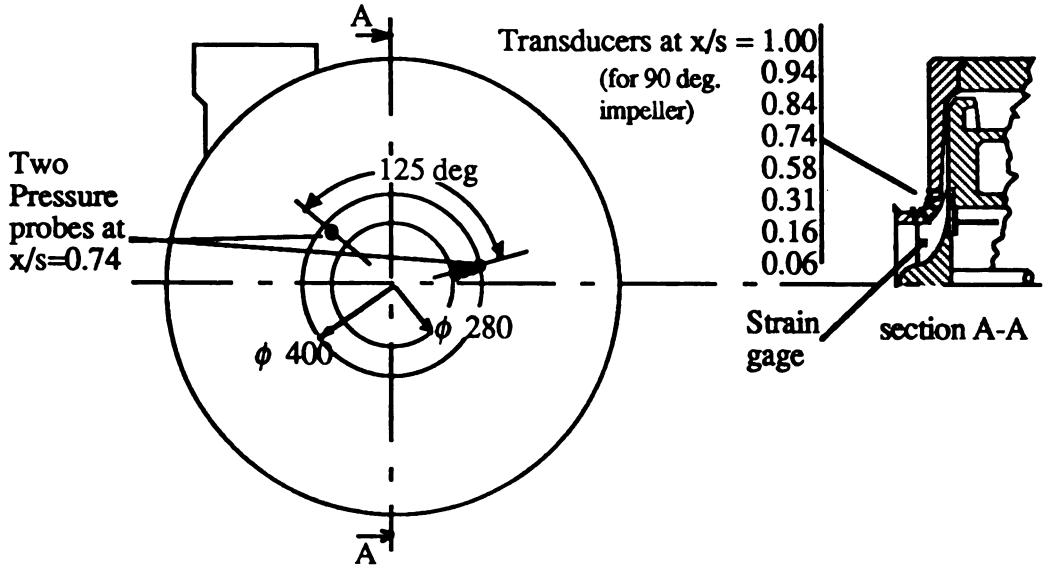

Fig. 2.1 Compressor Test Rig

Figure 2.2 gives compressor characteristic curves obtained for this investigation and also shows the measuring points for each speed line. Chapter 4 contains more complete characteristic curves for both the stage and the rotor. Surge formed the instability limitation for part-load

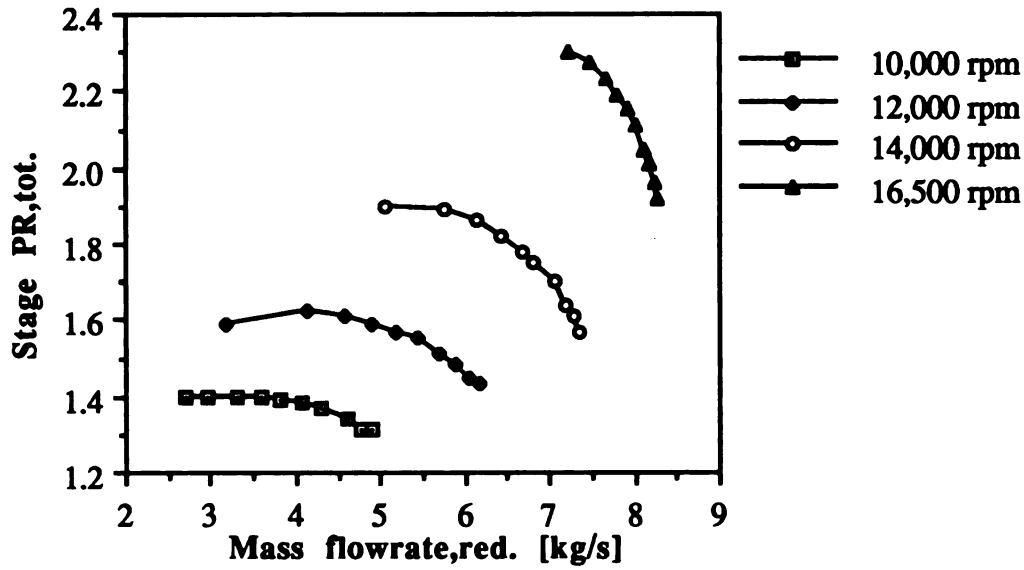

Fig. 2.2 Characteristic curves for test compressor

operation at N_{red}=10,000 and 12,000 rpm. However, intermittent rotating stall events with m=-3, m=+5, and m=+4 limited part-load operation at N_{red}=14,000 rpm. At N_{red}=16,500 rpm, the compressor was not run to the instability limit in order to avoid machine damage.

2.1.1 Rotor

This investigation employed a 20-bladed radial outlet rotor with every other blade cut back to x/s=0.25. For purposes of comparison,

Table 2.1 Geometric Data for Compressor Rotors

90-degree Impeller	**60-degree Impeller**
β_2=90 deg.	β_2=60 deg.
β_{1m}=27 deg.	β_{1m}=27 deg.
Z_i=10+10	Z_i=10+10
D_2=400 mm	D_2=400 mm
D_{1s}=280 mm	D_{1s}=280 mm
D_{1h}=90 mm	D_{1h}=90 mm
l_{ax}=130 mm	l_{ax}=130 mm
b_2=26 mm	b_2=26 mm

blade-to-blade static pressure difference measurements were also obtained for both the radial outlet rotor mentioned and a 20-bladed backswept impeller with every other blade cut back to x/s=0.34. Table 2.1 gives further information on the geometries of both impellers.

Previous testing at the Institutue of Turbomachinery (University of Hannover) found the blade vibration characteristics for the impellers used in this investigation. Table 2.2 presents these data.

Table 2.2 Natural Blade Modes for Impellers Used

Blade Mode	90-degree Impeller	60-degree Impeller
I.	1300 Hz	1300 Hz
II.	3305 Hz	2600 Hz
III.	4300 Hz	3950 Hz
IV.	5450 Hz	4400 Hz

These values represent approximate values for the impeller blades as a set. In actuality each blade has its own natural vibration frequencies, which may deviate from those given above. Also, the vibration of other blades is transmitted through the hub to any blade under consideration. Consequently, under the experimental conditions of this investigation, vibration measurements from one blade will show not only its own distinct blade vibration frequency but also vibration frequencies from the other blades. This produces fairly wide frequency band (say, of 60 Hz) for vibrations due to excitation of natural vibration modes, instead of one distinct vibration frequency for each mode.

2.1.2 Diffuser

A vaned diffuser fitted with nineteen cambered airfoil vanes was used for all tests. Table 2.3 gives the various geometric configuration

Table 2.3 Parameter Values for Diffuser Geometry

λ_3=1.15	LWR=2.37
β_3=27 deg.	AR=1.45
β_5=37 deg.	AS=0.61

parameters for the placement and orientation of diffuser blades. Appendix A contains a schematic representation of diffuser blade geometry and orientation.

2.2 Data Collection System

Results of this investigation are based upon measurements of flowrate, temperature, and pressure taken for several operating points, illustrated in Figure 2.2. Table 2.4 gives further information regarding measured quantities for this investigation.

Stagnation temperature and pressure readings were read and recorded manually. Analog voltage-time signals representing pressure history of operation at the different operation settings were recorded on 14 channels on magnetic tape. Transducer output was calibrated so that one bar of pressure corresponded to 1 volt of received output, with no offset.

2.2.1 Flowrate measurement

Flowrate was measured using a venturi-type flow meter located far downstream of the compressor exit. Throttle valves located downstream of the flow meter allowed for fine control of flowrate.

2.2.2 Rotor speed measurement

A tachometer measured shaft rotational speed. In addition, rotor speed could be obtained by identifying a peak in the blade strain frequency spectra corresponding to blade excitation due to the presence of the system exit.

Table 2.4 Measured Quantities

Parameter	Symbol	Measured at	Measured with	Processed by
Static pressure (unsteady)	P(t)	Shroud wall for several x/s positions	Kulite XCQ-080-050 dynamic press. transducer	HP-3582A FFT Analyzer & DIA/ DAGO™ (software)
Static pressure (steady)	P	Rotor exit at diffuser wall, stage exit (in exit pipe), & in plenum	Mercury manometers	
Total pressure	P_o	Midway between diffuser walls at rotor exit, diffuser exit, stage exit, & plenum	Kiel probes	Revue Thommen *Feindruckmesser* , type 19A2.10.02 & in-house software
Blade strain	e(t)	Inducer, approx. midway between hub & shroud	Strain gage with telemetry system	HP-3582A FFT Analyzer & DIA/ DAGO™ (software)
Mass flowrate	m	Far downstream of compressor exit	Venturi-type flow meter	In-house software
Total temperature	T_o	Midway between diffuser walls at rotor exit, stage exit, & plenum	Shadow probes	In-house software

2.2.3 Pressure measurement

Steady pressure measurements were taken (1) in a settling chamber located approximately 2.4 m. upstream of the impeller inlet, (2) at the rotor exit and at various other positions in the diffuser, and (3) at the stage exit. For total pressure measurements, flexible tubing routed pressures to a *Feindruckmesser* type 19A2.10.02 manufactured by Revue Thommen A.G. This measuring device was able to display pressures from 0 to 10,000 mm of water with a resolution of 10 mm of water. Static pressures were routed to mercury manometers with a resolution of 1 mm. Figure 2.3 shows measurement sites in the diffuser. Measurements were also read and displayed using pre-calibrated software.

Unsteady pressure measurements along the shroud wall were performed by means of several Kulite XCG-080-050 high-frequency response pressure transducers flush-mounted into the shroud wall. Appendix A contains further information on these transducers. The transducers resided at meridional positions in such a way as to follow the blade edge contour of the 60-degree impeller mentioned previously. This contour deviated slightly from that of the 90-degree impeller. Meridional position of the transducers for both rotors was determined by hand using a stiff wire. Figure 2.1 indicates these transducer positions for the blade contour of the 90-degree impeller. In order to allow phase analysis determination of the character of rotating stall events, a second transducer at x/s=0.74 was placed circumferentially 125 degrees from the first. For the 60-degree impeller, unsteady pressure measurements were taken along the shroud line at x/s=-0.02, 0.15, 0.4, 0.55, 0.70, 0.80, 0.95, and 1.03.

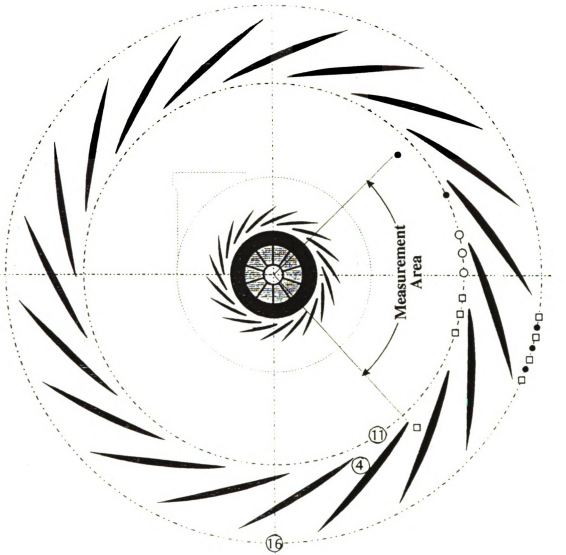

11 Measurement plane: Diffuser blade entrance, D/D2=1.10.
4 Measurement plane: Diffuser blade channel throat.
16 Measurement plane: Diffuser blade exit, D/D2=1.55.

□ Total pressure midway between diffuser walls.
● Static pressure along diffuser wall.
○ Total temperature midway between diffuser walls.

Fig. 2.3 Measurement sites in the diffuser

2.2.4 Temperature measurement

Temperature measurements allow for calculation of stage efficiencies. Total temperatures were read in the settling chamber located upstream of the impeller inlet. Also, total temperature measurements were obtained for several locations in the diffuser and at the stage outlet located just past the collector exit. Figure 2.3 shows the sites of temperature measurement in the diffuser.

2.2.5 Blade vibration measurement

Blade vibration measured simultaneously with shroud side static pressure gives insight into the character of unstable flow. This study used blade vibration data from a single strain gage mounted on a rotor blade at the site indicated in Figure 2.1. Previous tests and calculations on a 28-bladed radial impeller (β_2=90 deg.) determined that this is the zone of maximum stresses for vibrations in the I. and II. blade modes for a 28-bladed radial impeller used in earlier investigations (Haupt, 1985a, 1985b).

Vibrating blades flex, thereby elongating mounted strain gages. In this way strain gages prove useful for measuring blade vibration. In the present investigation, the mounted strain gage transmitted its vibration-dependent blade strain signals through a FM-telemetry system. A telemetry transmitter resided in the hollow impeller shaft and received power from an inductive power supply consisting of a coil system located between the gear box and the compressor. Transmitted signals were picked up by a permanently installed receiver near the test rig and then routed to data recording equipment.

2.3 Data Analysis Equipment

This investigation analyzed unsteady pressure signals in both the frequency and time domains and blade vibration signals in the frequency

domain. Digitizing data converted it into a form digestible to computer programs, useful in the detailed analysis of some signals. Electronic filters were used only to block very high frequencies (above 96,000 Hz) from recorded data during playback of that data. Figure 2.4 shows the signal processing pathway for unsteady blade vibration and shroud-side pressure signals.

Time signals were analyzed for evidence of pressure instability and provided the means for identifying problems in data recording and playback. In addition, time signal displays helped the investigator identify specific instances of pressure unsteadiness so that these could be classified as either rotating stall or surge.

Time signals were analyzed using a bench top FFT signal analyzer and a signal analysis software package. These allowed the investigator to

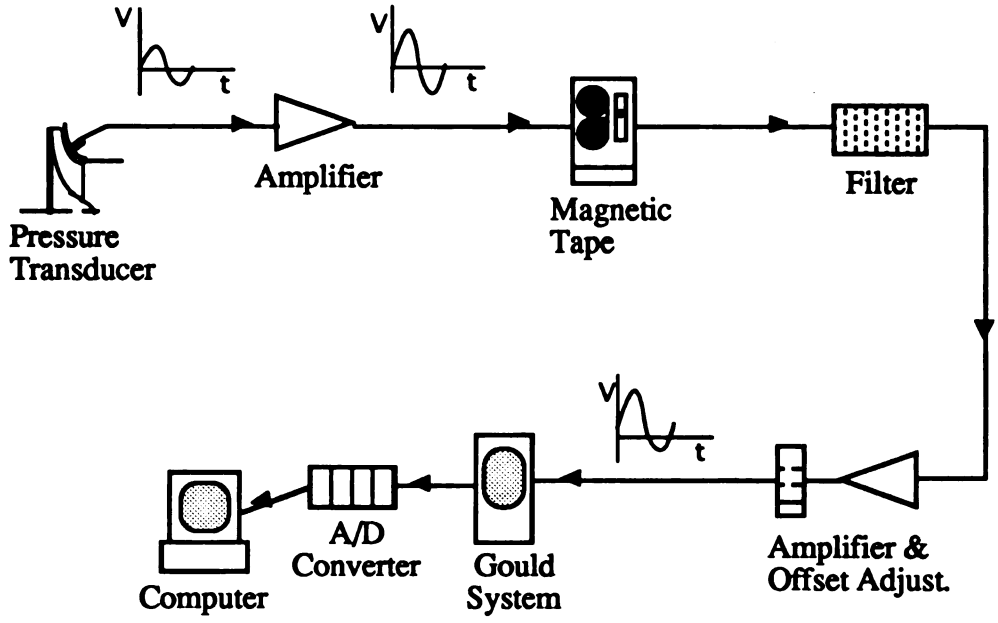

Fig. 2.4. Data processing pathway for analysis of unsteady pressure and blade vibration signals

determine peaks in pressure and blade vibration spectra, as well as phase transfer angles between unsteady pressure signals taken at two different circumferential positions.

2.3.1 Time-domain analysis equipment

Two principal tools were used to visualize pressure and blade vibration signals in the time domain: (1) an electrostatic recorder and (2) analog oscilloscopes. This investigation employed Gould Electronics' model ES2000 electrostatic recorder for visualizing several pressure signals simultaneously. This recorder consisted of an acquisition and control unit, a plotter, and a display screen. It received and displayed analog signals. Users can select individual signal amplification and arrangements for the display. Analog oscilloscopes used were of the usual type and were equipped with trigger and amplification settings.

2.3.2 Frequency-domain analysis equipment

Analysis of signals in the frequency domain provided a means for characterizing rotating stall regimes encountered and measuring the rms averaged blade-to-blade pressure difference at particular speed and flowrate settings. Conversion from the time domain to the frequency domain was performed via FFT analyses using (1) a Hewlett-Packard model 3582A spectrum analyzer and (2) DIA/DAGO™, a software package specifically designed for signal analysis. Both instruments converted pressure time signals to pressure-frequency signals. When two signals were analyzed and compared, both instruments could also provide phase angle spectra. However, only the HP analyzer could provide Coherence readings.

The Hewlett-Packard model 3582A spectrum analyzer accepted analog signals in the time domain, performed an FFT analysis on these signals and displayed the amplitude and frequency of oscillations embedded

in the original analog signal. Users could specify frequency ranges of interest for display (max: 0-25 kHz). For two channel FFT analysis, the bench top analyzer also provided information on amplitudes of Coherence (a statistical measure of the power in one signal caused by that of a reference signal) and phase shift between the two signals. Appendix A contains further technical details for this device.

In addition to a bench top FFT analyzer, this investigation made extensive use of DIA/DAGO™, a signal analysis software package for use on IBM compatible microcomputers. After converting digitized data to a format compatible with the software, it could be analyzed using the specific procedures dictated by the software. By this means any portion of the digitized signal could be displayed in the time domain. For further analysis, this software provided a means for performing either single signal or double signal FFT analyses to determine frequency characteristics of the recorded signal. In addition to providing the location and amplitude of discrete signal peaks in the frequency domain, the software also displayed the phase transfer angle for each frequency under consideration. However, it provided no information on coherence. Terminal displays could be saved to memory and/or printed.

Both the bench top analyzer and the software package allowed the user to specify passband windows for use in the FFT analysis. All FFT analyses in this study used a Hanning passband window.

CHAPTER 3--DATA ANALYSIS PROCEDURES

Analyzing measured quantities listed in chapter 2 allowed for (1) determination of characteristic curves showing pressure and efficiency variation with flowrate, (2) determination of variation in blade-to-blade pressure differences with both flowrate and meridional position, and (3) identification of the character of instabilities occurring at the part-load operation limit. These three results are covered in chapter 4. This chapter details how collected data were analyzed to produce the results presented in chapter 4. Table 3.1 shows the most important derived quantities.

Table 3.1 Derived Quantities

Parameter	Symbol	From	Analysis
Pressure frequency	f_p	FFT analysis	
Phase angle	$\Delta\phi_{st}$	FFT analysis	
Blade vib. frequency	f_b	FFT analysis	
Blade-to-blade static pressure difference	p_b	FFT analysis	
Shaft frequency	f_s		$f_s=N/60$
Blade passing freq.	f_{bp}		f_s/Z
Lobe number	m		$m=(\Delta\phi_{st}\pm k\cdot 2\pi)/\Delta\phi_g$ or $m=(f_b+\varepsilon\cdot f_p)/f_s$
Propagational speed	ω_{st}/Ω		$\omega_{st}/\Omega=f_p/(f_s\cdot m)$
Total pressure ratio	π_o		$\pi_o=P_{o2}/P_{o1}$
Isentropic efficiency	η_{isen}		$\eta_{isen}=[\pi_o^{(\gamma-1/\gamma)}-1]/(\tau-1)$

3.1 Data Processing

Careful records were kept for each operating point to keep track of pressures, temperatures, flowrate, amplification factors used to boost the transducer signals, etc. Appendix C shows these data. Temperature and pressure values were entered by hand into a computer; pressure ratios and efficiencies were then computed using an in-house program.

Determining the character of the instabilities forming the limit to part-load operation required the use of both analog and digitized signals. The bench top analyzer can perform FFT analyses on analog signals routed directly from the tape player. But, in order to more readily visualize the signals, the output from the magnetic tape player was routed first to the Gould visualization system , then to the FFT analyzer. The Gould visualization system displayed several signals at once and was easier to see and manipulate than oscilloscopes. However, an oscilloscope was also connected to the benchtop analyzer to provide a means of checking the

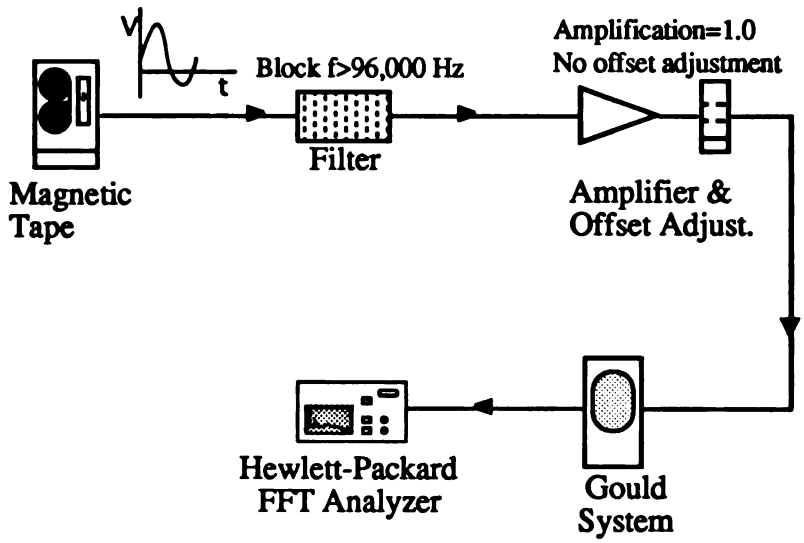

Fig. 3.1. Data processing pathway for use of Hewlett-Packard FFT analyzer

signal the analyzer received. Figure 3.1 shows the data processing set up used when using the FFT analyzer.

In addition to using the FFT analyzer for characterizing instabilities, DIA/DAGO™, a signal analysis software package, was also used. However, to use this software, portions of the analog signal recorded on magnetic tape had to be digitized and archived in computer memory or on floppy disks. To do this, analog signal output from the tape recorder was routed to the Gould system for visualization purposes, then to a digitizer, where the analog signal was digitized at a sampling rate of 33474 Hz and recorded in computer memory. Figure 2.5 shows this data processing pathway. A pre-written computer program managed data storage and digitizer control.

To digitize a section of the analog signal, the section was first observed on the Gould system. Next, investigators decided how large a section of the signal was of interest and what kind of resolution the investigation required. Because this investigation concerned surge and rotating stall, with frequencies below 200 Hz, investigators determined that digitizing 15,000 points with the tape run at 1/4 normal speed would adequately capture each event of interest with sufficient resolution. Thus, 1.04 seconds (1.04 seconds = [15,000 pts/3600 pts. per second] X 1/4)]) of each event of interest were digitized and recorded.

To more easily visualize signals for digitizing, voltage-time signals from the tape recorder were manipulated to have large amplitudes before they were digitized. This was accomplished by adjusting amplification and offset settings on the amplifier located between the tape player and the Gould system. Signals from the tape recorder were adjusted to give maximum signal values near but not exceeding 9 Volts. At the same time, minimum signal values were adjusted to be near but below -1 Volts.

After digitizing the data, investigators checked to make certain that signal maximum and minimum values all resided within the window required by the digitizer (-1V to 9 V). The digitized signal was then checked visually to make certain that it was continuous and resembled the analog signal. If so, then the digital data stored in computer memory was transferred to floppy disks and reloaded in a computer equipped with the signal analysis software. The digitized data, existing in ASCII format was then converted to a format required by the signal analysis software and analyzed according to the rules and procedures of the software.

The bench top FFT analyzer was used to determine the blade-to-blade pressure difference values over the normal operating range. The data processing stream was identical to that shown in Figure 3.1.

3.2 Analysis of Steady Operation

3.2.1 Pressure ratio and efficiency

Determination of pressure ratio and isentropic efficiency was straightforward. The stage and rotor total pressure ratio compares the total pressures recorded at the stage exit and rotor exit, respectively, with the total pressure recorded in a settling chamber upstream of the impeller inlet. As such, they are

$$\pi_{o,rotor} = \frac{P_{o,2}}{P_{o,K}} \text{ and} \qquad (3\text{-}1)$$

$$\pi_{o,stage} = \frac{P_{o,7}}{P_{o,K}}, \text{ where} \qquad (3\text{-}2)$$

$P_{o,2}$ is the impeller exit total pressure,
$P_{o,7}$ is the stage exit total pressure, and
$P_{o,K}$ is the total pressure in the settling chamber.

Isentropic efficiency can likewise be calculated for both the rotor and the stage exits. Efficiency is a ratio of actual work compared to work done in an ideal process. For compression between states 1 and 2, this can be expressed as a ratio of the isentropic work (representing the ideal process) and the real work. In terms of enthalpy, this becomes

$$\eta_{isen} = \frac{w_{isen}}{w_{real}} = \frac{h_{o,2isen} - h_{o,1}}{h_{o,2} - h_{o,1}} \tag{3-3}$$

For an ideal gas, the relation $dh=c_p \cdot (dT)$ can be used to rewrite equation (3-3) in terms of temperature.

$$\eta_{isen} = \frac{w_{isen}}{w_{real}} = \frac{T_{o,2isen} - T_{o,1}}{T_{o,2} - T_{o,1}} \tag{3-4}$$

For an isentropic process, pressure and temperatures are related according to $\frac{P_{o,2}}{P_{o,1}} = \left(\frac{T_{o,2isen}}{T_{o,1}} \right)^{\left(\frac{\gamma}{\gamma-1}\right)}$. Therefore, substituting into equation (3-4), the isentropic efficiency for a compression process between states 1 and 2 can be written as

$$\eta_{isen} = \frac{\left(\frac{P_{o,2}}{P_{o,1}} \right)^{\left(\frac{\gamma-1}{\gamma}\right)} - 1}{\frac{T_{o,2}}{T_{o,1}} - 1} \tag{3-5}$$

For this investigation, equation (3-5) can be used to find values for the isentropic efficiency for the rotor and for the stage. The appropriate expressions are

$$\text{Rotor isentropic efficiency } \eta_{o,rotor} = \frac{\left(\pi_{o,2}\right)^{\left(\frac{\gamma-1}{\gamma}\right)} - 1}{\tau_{o,2} - 1} \qquad (3\text{-}6)$$

$$\text{Stage isentropic efficiency } \eta_{o,stage} = \frac{\left(\pi_{o,7}\right)^{\left(\frac{\gamma-1}{\gamma}\right)} - 1}{\tau_{o,7} - 1}. \qquad (3\text{-}7)$$

Values for rotor and stage isentropic efficiencies were computed for each measuring point.

3.2.2 Blade-to-blade pressure difference

For the normal operating range, a transducer mounted on a compressor shroud wall will give a pressure signal similar to that represented in Figure 3.2. The signal has a sawtooth nature due to the passing of the impeller blades. Pressure builds up in an impeller channel from the suction side to the pressure side. The pressure reaches a maximum as the pressure side of a blade passes, then drops rapidly when the blade passes the transducer and the transducer senses pressure on the suction side of the blade. Pressure then rises again, dropping when the next blade passes. The blade passing frequency gives the number of pressure peaks produced by the passing of the impeller blades per unit time. For a single blade pass, $f_{bp}=1/T_b$. Blade passing frequency is always much higher than the frequencies associated with rotating stall and surge.

Blade-to-blade static pressure differences can be determined by performing a FFT analysis of a recorded signal and observing the magnitude of the resulting pressure spike at the blade passing frequency. This blade passing frequency can be determined using the rotational speed using the equation

$$f_{bp} = \frac{N \cdot Z}{60}, \text{ where N is given in revolutions per minute.} \quad (3\text{-}8)$$

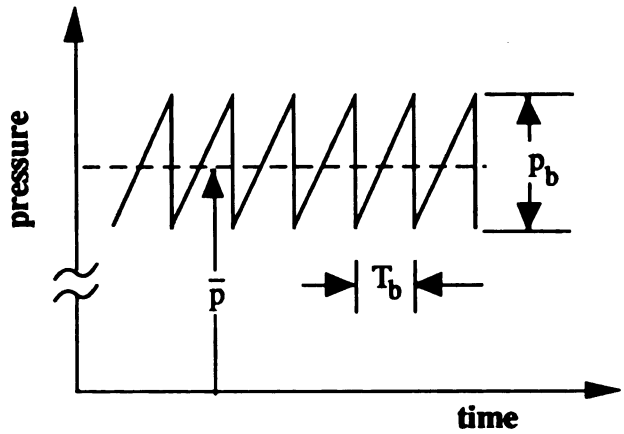

p_b = blade-to-blade pressure rise
$\bar{p}$ = mean pressure
T_b = blade pressure rise period

Fig. 3.2. Sawtooth signal sensed by pressure transducer in shroud wall

Since we investigated operation at 10,000 rpm, 12,000 rpm, 14,000 rpm, and 16,500 rpm, the blade passing frequencies listed in table 3.2 were of interest

TABLE 3.2 Blade Passing Frequencies of Interest

Speed [rpm]	Before Splitter (x/s<0.25)	After Splitter (x/s≥0.25)
10,000	1,667 Hz	3,333 Hz
12,000	2,000 Hz	4,000 Hz
14,000	2,333 Hz	4,667 Hz
16,500	2,750 Hz	5,000 Hz

Once blade passing frequency was determined, bench top analyzer settings were adjusted to display the expected blade passing frequency and the recorded signal was sampled and averaged by the FFT analyzer using a

32-sample RMS mode with a Hanning passband window. The last portion of the recorded signal for the measurement point corresponding to the lowest flowrate at N_{red}=12,000 rpm contained surge events, and a 32-sample average could not be used for this point. Instead, 16-sample RMS averaging was used. The amplitude of the blade-to-blade pressure differences appeared as spikes in the pressure spectra near the calculated blade passing frequency. Because shaft speed varied slightly at each operating point, it was necessary to set the range setting to 0-5000 Hz.

Selection of the frequency range played a critical role in obtaining useful values for blade-to-blade pressure rise. At any measuring point, rotor speed fluctuates slightly. This, in turn, makes the blade passing frequency fluctuate slightly. If investigators use a small frequency range in their investigation, the analyzer resolution becomes small enough to detect each of these variations in rotor speed. On the analyzer display, they will observe several peaks occurring in a small frequency band (e.g., three major peaks between 1669 and 1674). Since this investigation used RMS averaging, pressure peaks occurring at non-identical frequencies affect the amplitude of each other. For example, suppose the first sample picked up a pressure peak occurring at 1670 Hz with an amplitude of 55 mV. Now, what happens if the second sample picks up a pressure peak at 1674 Hz with a similar amplitude? The analyzer computes new RMS averages for both 1670 Hz and 1674 Hz. Since the peaks did not occur at identical frequencies, the RMS average amplitudes drop for both frequencies. To avoid this problem, the frequency range must be set to produce a sufficiently grainy resolution so that minor rotor speed variations do not affect the amplitude of the pressure spike occurring at the blade passing frequency.

Readings of blade-to-blade pressure amplitude for several meridional positions for each measuring point (a compressor operation point at which measurements were taken) were recorded by hand in measurement charts. Since transducer signals were amplified before being recorded on magnetic tape, the values obtained for blade-to-blade pressure rise from the FFT analysis still retain the influence of this amplification. To find the true value measured by the transducers, these raw blade-to-blade values were divided by the appropriate amplification coefficients. For example, suppose a transducer registers a pressure rise corresponding to an output of 4.2 mV. Suppose further that before being recorded this was amplified by 8 (i.e., amplification coefficient=8.0). Then, the blade to blade pressure difference detected by the bench top analyzer would be 4.2 mV X 8=33.6 mV. To get back to the true value of 4.2, the blade-to-blade pressure value obtained from the FFT analyzer (viz., 33.6) must be devided by the amplification coefficient (viz., 8). This procedure was performed for all measurement points for all working probes. Appendix C contains the values of both the raw and adjusted pressure rise data and the values of the amplification coefficients used.

As one might expect, blade-to-blade pressure difference amplitudes for operation at high speeds exceed those of lower speeds. Two means were used to account for the influence of blade speed on blade-to-blade pressure difference to make the data more comparable with one another. First, blade-to-blade pressure values were non-dimensionalized using the rotor exit static pressure. These non-dimensionalized values were then plotted against both meridional position and mass flowrate. Appendix D contains the resulting graphs. A second means to account for the effect of operating speed on

blade-to-blade pressure rise data consisted of converting these data into pressure coefficients using the following formula:

$$\psi_b = \left(\frac{2 \cdot p_b}{\rho_K \cdot u_2^2} \right). \qquad (3\text{-}9)$$

This strategy successfully collapsed the data into the same approximate range while retaining the overall trends observed in the unadjusted data.

Blade-to-blade pressure coefficient data were plotted against both meridional position and flow coefficient using Mathematica™, a mathematics software package. Chapter 4 contains these results. To convert the pressure coefficient data into a form digestible to Mathematica, data were first plotted and interpolated using CricketGraph™ (a software package for creating 2-D plots). Values needed for Mathematica were then read from these graphs visually, manually recorded, then transferred to Mathematica.

3.3 Analysis of Unsteady Flow/Operation

Determination of the specific character of unsteady operation required analysis of unsteady pressure and blade vibration data in both the time and frequency domains.

3.3.1 Analysis of the time domain

Unsteady pressure-time signals were analyzed in the time domain by first printing hard copies of the signals, then measuring distances corresponding to the wavelengths of principal frequencies present. Hard copy representations of signals of interest were obtained using either the Gould system plotter or the signal analysis software together with a laser quality computer printer. Events were classified as either rotating stall or surge according to how their time histories resembled those of rotating stall and surge events from past investigations.

3.3.2 Analysis of the frequency domain.

Most insights into the nature of unsteady flow in this investigation occurred through FFT analysis, which converts signals in the time domain to signals in the frequency domain.

Rotating stall in centrifugal compressors can be characterized in terms of stall cell (lobe) number, rotational speed, and rotational sense. Two types of analysis are commonly used to measure the stall propagation and lobe number (1) Analysis of pressure measurements taken from two pressure transducers placed at different circumferential, but identical radial positions, and (2) Analysis of pressure signals along the shroud wall, together with blade vibration frequencies. The following explains these two methods.

3.3.2.1 Pressure/phase angle analysis

The first method finds the lobe number by comparing the phase angle between pressure signals of two peripherally placed transducers. Figure 3.3 shows two such pressure signals and indicates the phase difference between them. Lobe number can be obtained by applying the following expression:

$$m = \frac{(\Delta\phi_{st} \pm k \cdot 2\pi)}{\Delta\phi_g}, k = 0,1,2,3,... \qquad (3\text{-}10)$$

Here, $\Delta\phi_{st}$ is the angular phase difference between the two pressure signals and $\Delta\phi_g$ is the physical angle separating the two circumferential spaced transducers. The direction of rotation is found by noting which pressure signal leads the other. Appendix B shows the derivation of this equation. Proper placement of the pressure transducers allows for accurate, distinct determination of lobe number. The present investigation makes use of transducers placed at ϕ_g= 0 degrees and ϕ_g= 125 degrees. Accordingly,

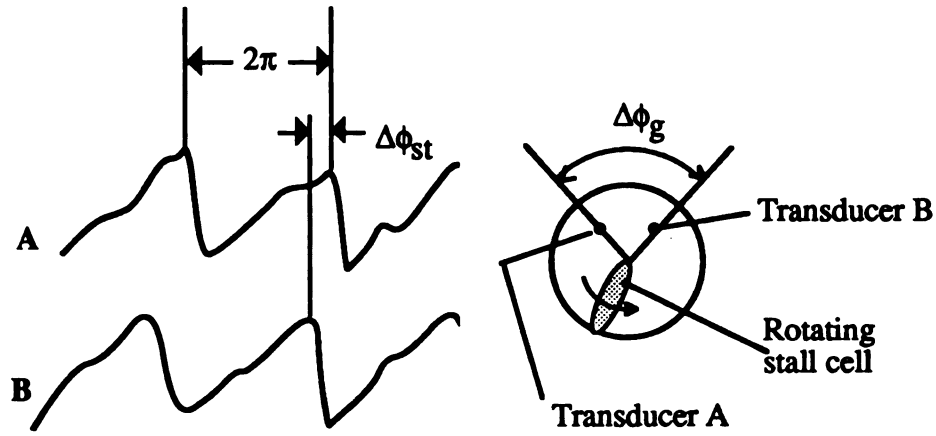

Fig. 3.3. Signals produced by two circumferentially-spaced transducers

$\Delta\phi_g$= 125 degrees, and a m=+3 rotating stall can produce a phase angle of 15 degrees [i.e., 3=(15 deg/125 deg)=(375 deg/125 deg)].

Since $\Delta\phi_g$ is fixed, it follows from equation (3-10) that finding the lobe number for a rotating stall event only requires the determination of phase angle. The only phase angles of interest are those corresponding to pressure pulses produced by rotating stall events. However, the pressure spectra may contain several peaks, not all of which are produced by rotating stall events. To distinguish peaks that may correspond to rotating stall from those peaks that do not requires the use of the coherence function. Coherence is a statistical function relating the amount of power in one measured signal caused by the other measured signal. If an FFT analysis of two measured static pressure signals produces peaks at the same frequency (f_p) and the Coherence at this frequency is high (0.95<coherence≤1.0), then the peaks have been produced by the same physical event. If, on the other hand, their coherence is too low (Coherence<0.95), then these peaks may be dismissed from consideration. The bench top analyzer determined coherence, but the signal analysis software did not. On the bench top

analyzer, coherence is found after performing a dual-signal FFT by pushing the COHER button on the display channel and moving the screen marker to the frequency of interest. Examination of phase angles followed the identification of peaks with sufficiently high coherence values.

Signal phase angles could be obtained by using either the bench top analyzer or the signal analysis software after performing a FFT analysis on two signals. On the H-P analyzer, the value of the transfer angle could be obtained by pressing the XFR FCTN button under the PHASE display, then scrolling over to the frequency of interest. Magnitude appeared at the bottom of the display. With the software, one had to adjust computer to a two-channel setting before running the FFT analysis. After the FFT analysis, a graph showing phase angle variation with frequency can be displayed. Amplitudes corresponding to marker position are displayed on the monitor. Thereafter, determining phase angle amplitude simply involved moving the cross-hairs marker to coincide with the graphed value at the frequency of interest.

Both the FFT analyzer and the software displayed phase angle values between -180 degrees and 180 degrees. Any phase angle falling outside of this range can be converted into an equivalent angle within the range by adding or subtracting multiples of 360 degrees. For example, 350 degrees= 350 degrees - 360 degrees = -10 degrees.

So called "deep noise" of the electronic system sometimes also produces a significant peak, which can be dismissed as meaningless. In this investigation, electronic noise sometimes showed up as a peak at 50 Hz. It occasionally produced harmonics at multiples of 50 Hz.

Special problems arise when two or more peaks show up in the pressure spectra. Ordinarily, when these occur, the peaks represent

harmonics of some principal peak and occur at frequencies which correspond to simple multiples of the principal frequency. For example, Figure 3.4 schematically shows three peaks occurring at 35, 70, and 105 Hz; and it appears that the 70 and 105 Hz peaks are simply harmonics of the 35 Hz peak. Although peaks may appear to be related, they may in fact be caused by separate events. To check, the investigator must examine phase angles corresponding to the peaks. If a mode of rotating stall changes speed abruptly, it will give rise to two separate peaks in the pressure spectra. These will have the same phase angle values. However, multiple peaks sometimes appear which do not appear to be simple harmonics of a principal peak and do not share the same phase angle. Yet, these may still be related.

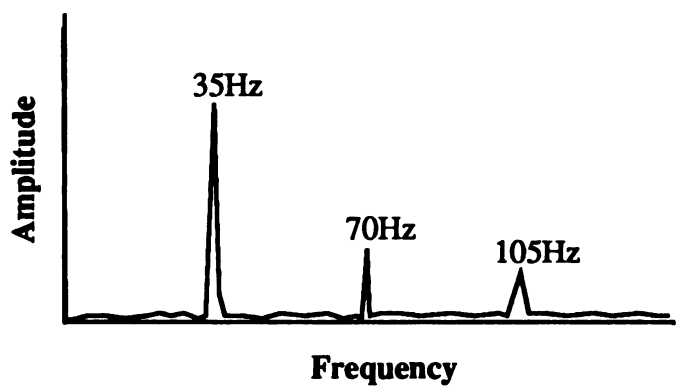

Fig. 3.4. Harmonics produced by principal pressure fluctuation at 35 Hz

To check if two pressure peaks with distinctly different frequencies and phase angles are produced by the same mode of rotating stall, one must check to see if the ratio of the phase angles is the same as the ratio of the frequencies of the pressure peaks. For example, suppose three peaks show up in the pressure spectra at 30, 65, and 98 Hz with phase angles of 100, -138, and -35 degrees respectively. In this case (65 Hz/30 Hz)=2.17 and (222 deg/100deg)=2.22. Since these ratios nearly equal one another, it follows that the 65 Hz peak and the 30 Hz peak both result from the same event.

Notice that in this analysis, -138 degrees was converted to 222 degrees (222=-138+360). A similar analysis reveals that the 98 Hz peak also originates from the same source as the 30 Hz peak.

A loose explanation for this way of relating pressure peaks lies in equation (3-10). Two pressure peaks (in the frequency domain) produced by the same event are analogous to pressure peaks produced by events with identical rotational speed but different lobe numbers. Take, for example, a prominent peak at 30 Hz and a smaller but prominent peak at 60 Hz. If the 30 Hz peak is produced by a m=+2 rotating stall rotating at 1000 rpm, the 60 Hz peak is viewed as being caused by a m=+4 rotating stall rotating at 1000 rpm. Examination of equation (3-10) reveals that for a fixed value of $\Delta\phi_g$, when m doubles, ϕ_{st} must double. If indeed, the phase angle at f_p=60 Hz is found to be double that at f_p=30 Hz, then both peaks are caused by the event producing the more prominent of the two peaks.

Once the phase angle of the principal peaks are found, the corresponding lobe number of the rotating stall causing that peak can be computed using equation (3-10). Rarely do the numbers work out perfectly. In fact, experience suggests that this method for determining lobe number gives ambiguous results unless at least three transducers are used. Since only two circumferentially placed transducers functioned properly under this investigation, results were checked using the method explained next.

3.3.2.2 Blade vibration analysis

Combining information on peaks occurring in the pressure spectra with those occurring in blade strain spectra provides a second means for determining the lobe number of rotating stalls encountered.

When pressure unsteadiness occurs, it acts as a periodic force on impeller blades. This, in turn, produces blade vibrations of significant

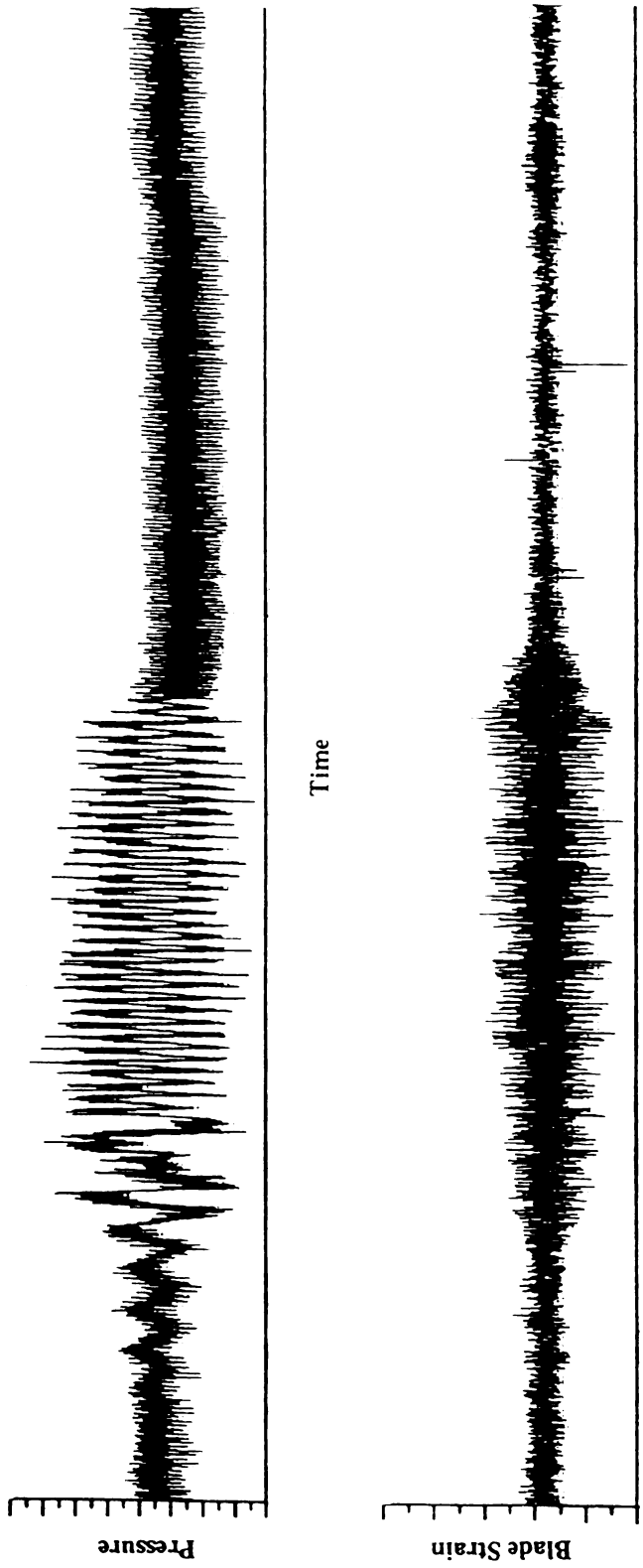

Fig. 3.5. Effect of pressure unsteadiness on blade vibration

magnitude. To illustrate this effect, Figure 3.5 shows pressure unsteadiness measured at x/s=0.74 for N_{red}=14,000 rpm and the resultant effect that it had on blade vibration.

Starting from general considerations of kinematics relating motion in a rotating frame of reference with that in an absolute frame, $\omega_{abs} = \omega_{rel}+\omega_{rel/abs}$, the following expression can be derived:

$$f_b = (m \cdot f_s - \varepsilon \cdot f_p) \qquad (3\text{-}11)$$

Here

f_b is blade vibration frequency,
f_s is the frequency of the rotational speed of the rotor ($f_s = \omega_{shaft} \times 2\pi$),
f_p is the frequency of pressure pulses associated with rotating stall and measured in the absolute frame of reference,
m is the number of stall cells, and
ε = +1 when, in the absolute frame, the rotating stall rotates in the opposite direction as the rotor rotation
= -1 when, in the absolute frame, the rotating stall rotates in the same direction as the rotor.

Appendix B gives a complete derivation of this expression.

Values for f_b are obtained by noting at which frequencies large, distinct peaks in blade strain occur. For example, Figure 3.6 shows one distinct peak plus a band of peaks corresponding to the blades' I. Mode. Shown also is a small peak corresponding to the shaft frequency. In this investigation, only blade peaks lying outside the I. Mode band were examined, unless pressure signal phase analyses predicted a lobe number corresponding to a blade vibration peak inside the band. Using equation (3-11), investigators can find which blade vibration peaks correspond to a mode of rotating stall.

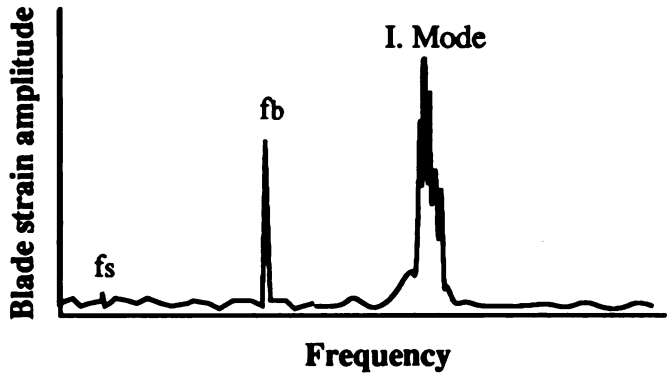

Fig. 3.6. Peaks in blade vibration spectra

At one measuring point, multiple modes of rotating stall may occur in series. When this happens, peaks corresponding to each of these modes of rotating stall show up in the blade vibration spectra . Jin, et al. (1992a) have also shown that a circumferentially asymmetric rotating stall can produce several peaks in blade vibration spectra. According to the authors, the blade frequencies excited under conditions of an asymmetric rotating stall are given by

$$f_b=M(m\cdot f_s\pm f_p)+N\cdot f_s \qquad (3\text{-}12)$$

where M and N are natural numbers.

Although readings for blade vibration could be obtained using both the bench top analyzer and signal analysis software, the software approach proved much more flexible and easier to handle. It proved especially helpful in analyzing very brief events.

Relative propagation speed of the stalls cells can be obtained by applying

$$\frac{\omega_{st}}{\Omega}=\frac{f_p}{m\cdot f_s} \qquad (3\text{-}13)$$

CHAPTER 4--RESULTS AND DISCUSSION

This investigation seeks to characterize the operational characteristics of a compressor operated at four speeds. Describing compressor performance takes the form of (1) illustrating characteristic curve and efficiency data for the rotor and the compressor stage, (2) characterizing the particular forms of instability forming the limit to part load operation, and (3) describing blade-to-blade pressure rise data over the normal operating range of the compressor. The following reports this information.

4.1 Stage and Rotor Performance

As shown in Figure 4.1, several measurement points were taken for each speed: 10,000, 12,000, 14,000 and 16,500 rpm. For the 10,000 rpm, 12,000 rpm, and 14,000 rpm speed lines, tests were conducted from the choke limit to the instability limit. The compressor was not run to the instability limit for the 16,500 rpm speed line in order to avoid potential machine damage which could result from rotating stall or surge at this speed. Data at the instability limits for N_{red}=10,000 and 12,000 rpm were obtained by continuously reducing the flowrate at incipient surge.

Surge constituted the instability limits of operation at both 10,000 rpm and 12,000 rpm. At 10,000 rpm, one instance of intermittent rotating stall was detected before the machine entered recognizable surge. For operation at 12,000 rpm, the compressor entered surge without any instances of either intermittent or continuous rotating stall. At 14,000 rpm, the occurrence of intermittent rotating stall formed the operation limit at low mass flowrate.

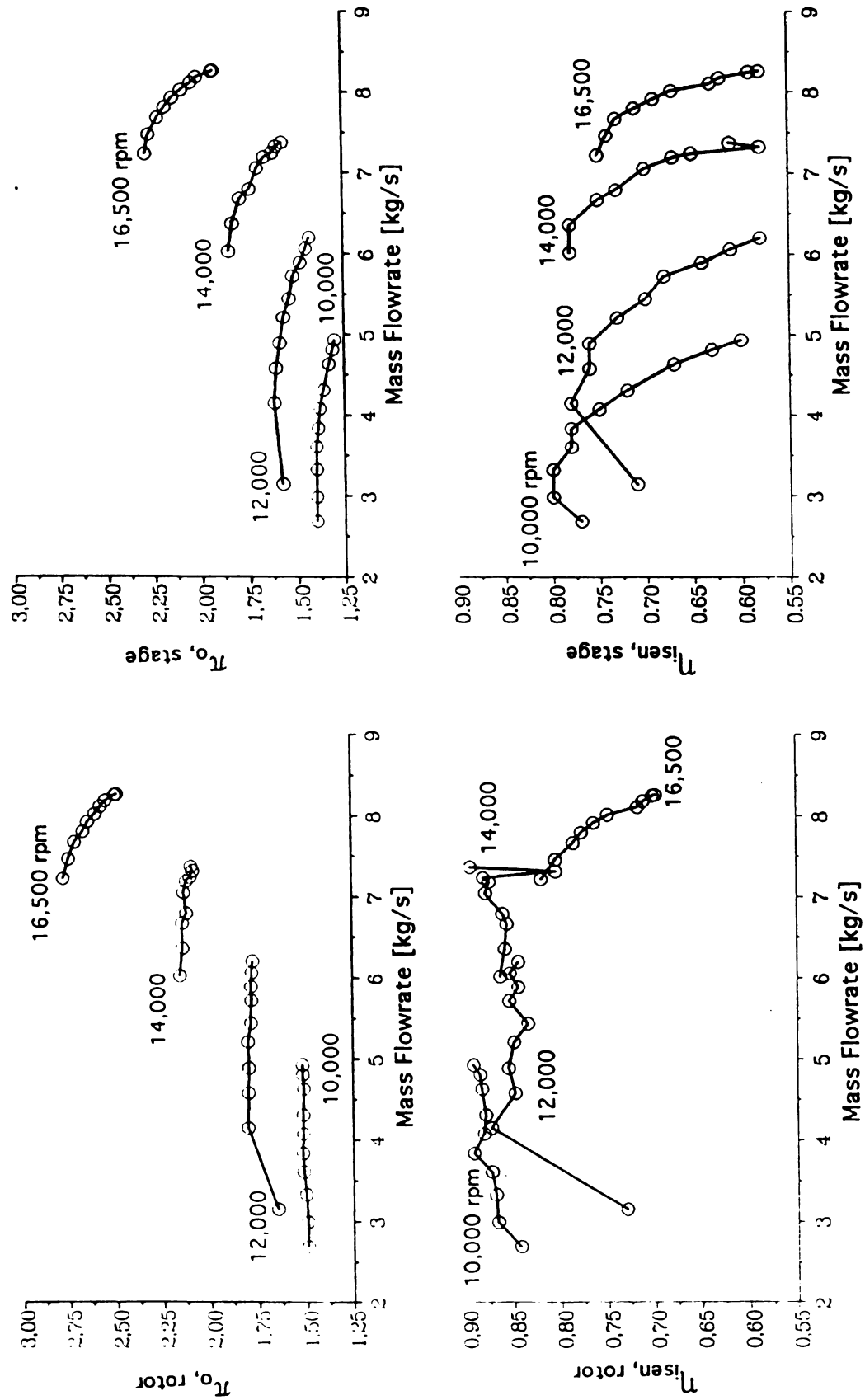

Fig. 4.1. Characteristic curves for rotor and stage

Figure 4.1 shows that total pressure at rotor exit decreased slightly for operation at 10,000 rpm as flowrate was decreased. At 12,000 rpm and 14,000 rpm it generally increased slightly. In contrast, total pressure gains in the rotor at 16,500 rpm, increased boldly as flowrate dropped. Rotor isentropic efficiency partly explains the behavior of total pressure in the rotor. Efficiencies for both 10,000 rpm and 14,000 rpm gradually decline as flowrate drops. The unusual efficiency value for the second highest flowrate at 14,000 rpm agrees with recorded values. Therefore, it probably stems from an incorrectly recorded experimental datum. At 12,000 rpm, the sudden drop in efficiency at incipient surge produced a corresponding drop in total pressure rise. Rotor isentropic efficiency at 16,500 rpm increased significantly over the entire recorded range as flowrate was reduced.

Figure 4.1 also shows stage performance. Losses in the diffuser produce stage pressure ratios and efficiencies below those for the rotor. Low efficiencies at high flowrates serve to decrease the total pressure available at the stage exit. Hence, stage pressure ratios tend to assume their lowest values at high flow operation and generally increase as flowrate drops. Again, the dramatic decrease in isentropic efficiency at incipient surge corresponds to a decrease in total pressure ratio for that point.

4.2 Surge Characteristics

Surge forms the instability limits for operation at both 10,000 rpm and 12,000 rpm for the compressor under investigation. This investigation confirmed earlier findings that a rotating stall with m=+1 forms significant portions of surge events in centrifugal compressors. In addition, an interesting form of rotating stall--forming an initial surge event--was

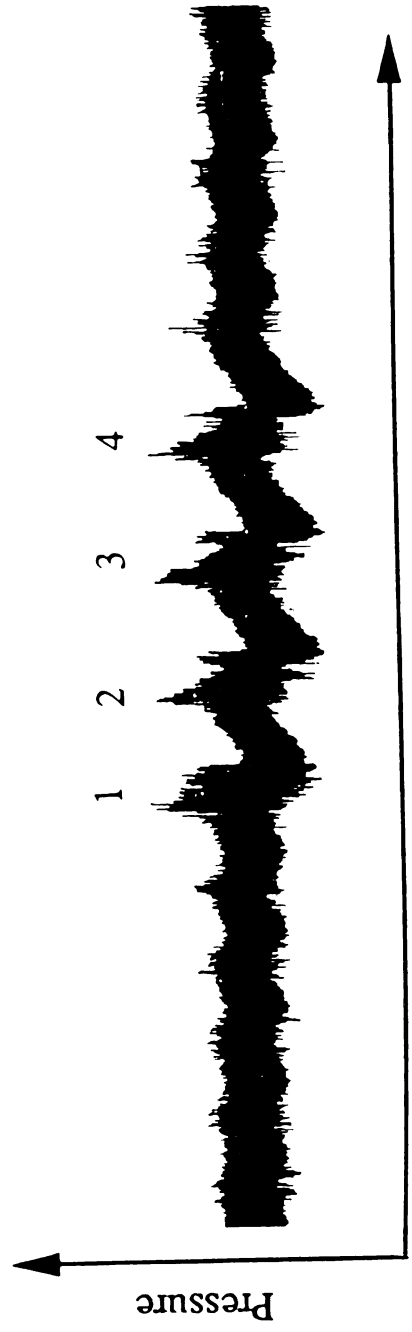

Fig. 4.2. Gould plot of surge train, N_{red}=10,000 rpm

measured at N_{red}=10,000 rpm. The following provides details regarding surge encountered in this investigation.

4.2.1 Surge at N_{red}=10,000 rpm

Figure 4.2, obtained from the Gould recorder, shows the surge events occurring at N_{red}=10,000 rpm. Analysis of the time signal reveals that each event occured for about 0.6 seconds and resembled the others in that they all show a general decline in mean pressure followed by pressure recovery. Pressure/Phase analysis using the bench top analyzer revealed the presence of stall with m=+1 occurring within each instance of surge. For a clearer picture, we digitized pressure and blade vibration signals for the first and third events depicted in Figure 4.2.

Figure 4.3 shows the first of the recorded instabilities in the surge train for machine operation at 10,000 rpm. Here two pressure-time signals taken simultaneously for different circumferential positions at x/s=0.74 are juxtaposed to ease comparison. Both show a general drop in mean pressure with the oscillating rotating stall signals superimposed. Although both signals are similar, they are not identical. This is normal. Signals obtained from different circumferential positions reflect the continually changing unsteady nature of real physical flows as they respond to different boundary conditions. For example, it is well known that the presence of a volute exit produces a circumferential non-uniformity in pressure signals. The remaining surge events more closely resembled that shown in Figure 4.4.

Figure 4.4 shows that for both circumferential probes at x/s=0.74, the mean pressure begins to drop for the first 0.13 seconds. This drop in pressure is followed by a general rise in pressure until clear rotating stall ceases. This pressure pulse indicates the presence of reverse flow in

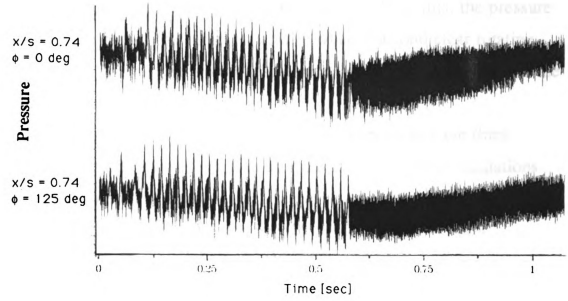

Fig. 4.3. First event in surge train, N_{red}=10,000 rpm

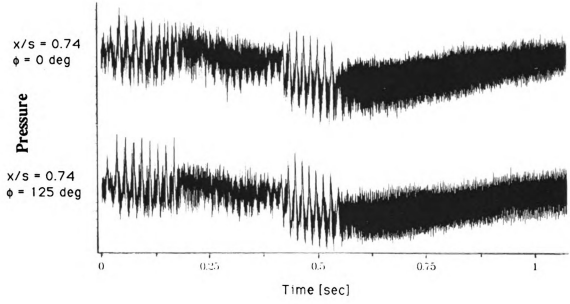

Fig. 4.4. Third event in surge train, N_{red}=10,000 rpm

impeller passages during surge (Pampreen, 1993). After this, the pressure drops over the rest of the surge, especially when a second clear rotating stall emerges. After the surge event, the mean pressure recovers before the compressor enters surge again.

The surge event illustrated in Figure 4.4 appears to have three distinct sections. The first section is characterized by distinct oscillations which die out abruptly at about t=0.2 seconds. After this comes the middle section, which lasts about one-quarter of a second (about 42 rotor revolutions). Parts of this middle section also appear to contain pressure oscillations. The final section resembles the first in that it contains very distinct oscillations which end abruptly at the end of the surge event at about t=0.6 s. After the surge event, no distinct pressure oscillations occur and normal flow resumes with a recovery in the mean pressure.

Analysis using both the bench top analyzer and signal analysis software reveals that the first instance of surge depicted in Figure 4.2 is

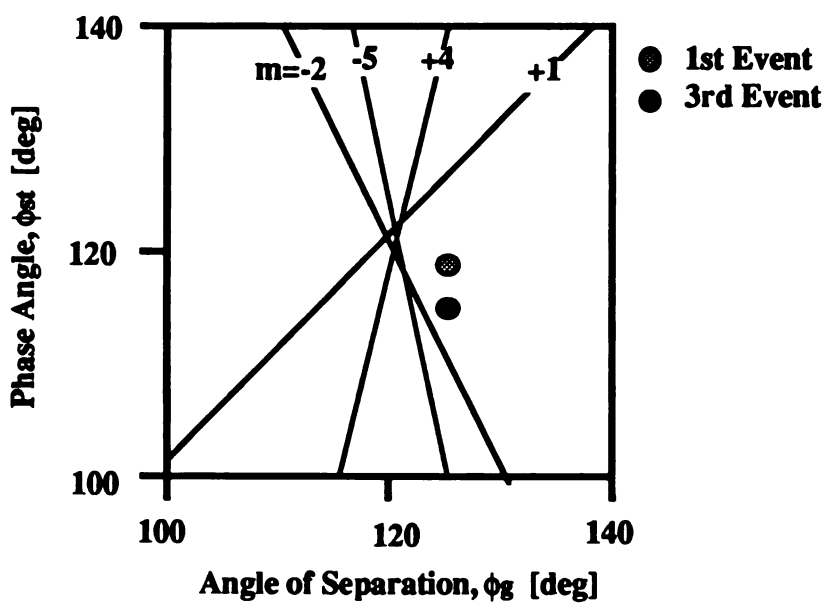

Fig. 4.5 Phase Angle Analysis for Nred=10,000 rpm.

composed entirely of m=+1 rotating stall with speed ω_{st}/Ω=0.33. It also reveals that m=+1 rotating stall causes the clear pressure oscillations at the beginning and ending sections of the surge event depicted in Figure 4.4. Figure 4.5 shows the results of pressure/phase analyses for both events. Note that the phase analysis reveals several possible modes of rotating stall. Blade vibration analysis provided a better indication of the lobe number. Table 4.1 shows the results of the analyses. Full results are given in appendix F.

Table 4.1. Rotating stalls in surge at N_{red}=10,000 rpm

Event Number	Pressure Frequency f_p	Lobe Number m	Propagation Speed ω_{st}/Ω
1	56.3 Hz	+1	0.335
3	54.4 Hz	+1	0.324

Interestingly, both pressure/phase angle analysis and blade vibration analysis showed no clear evidence of rotating stall in the middle section of surge events resembling event 3. Figure 4.6 compares blade vibration signals for the first section of the surge event with the middle section. The blade vibration spectra for the first section reveals distinct blade vibration peaks at 117 Hz and 233 Hz. Both peaks are caused by pressure oscillations. Comparison with pressure spectra data reveals that a rotating stall with m=+1 causes the 117 Hz blade vibration peak. Contrasted to this, the blade vibration spectra for the middle section of the surge signal shows no clear blade vibration peaks except for the blades' I. and II. vibration mode. Other than these, blade vibration remains fairly flat. A more complete description of a surge event will be undertaken for surge at N_{red}=12,000 rpm to illustrate the distinct character of each section of surge.

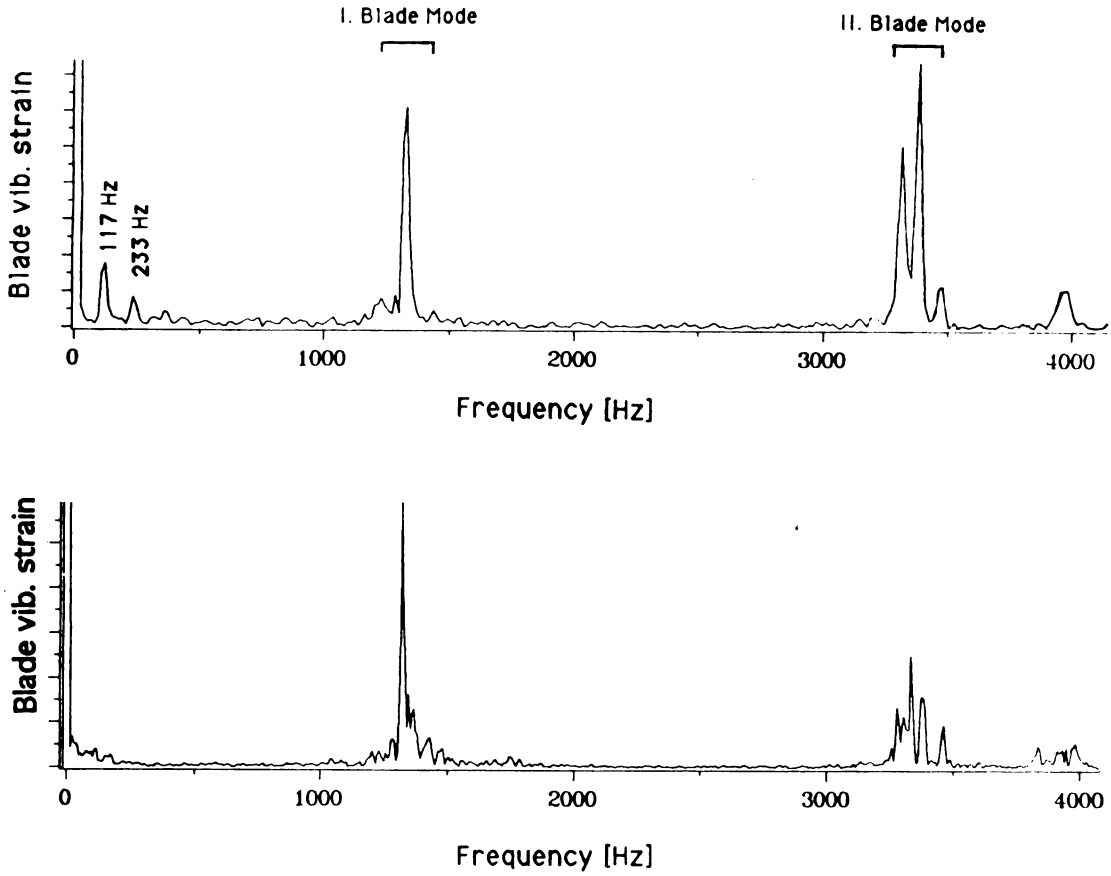

Fig. 4.6. Blade vibration spectra of first section of surge (top) and middle section of surge (bot.)

The pressure/phase angle analysis for the rotating stalls occurring in surge events at N_{red}=10,000 rpm represents a good case where the same event will produce several peaks in the pressure spectra. Figure 4.7 shows the pressure spectra and phase angle readings for the third instability in the surge train. Here, as recorded in Table 4.1(b), we have three well-defined pressure peaks at 54, 109, and 161 Hz with corresponding phase angles ($\Delta\phi_{st}$) of 118, -128, and -5 degrees, respectively. The analytical procedures explained earlier for determining if pressure peaks arise from the same source reveals that the same source produces all three peaks. The bench top analyzer detected multiple peaks also, with frequency and phase angle information similar to those represented in Figure 4.6. However, it was difficult to establish to which surge event these readings pertained. Coherence for each peak was approximately 1.0. Appendix F gives more complete information.

4.2.2 Surge at N_{red}=12,000 rpm

A surge event recorded at the instability limit for N_{red}=12,000 rpm is given in Figure 4.8. Chen, et al. (1994) have analyzed the character of mild, progressive stall before surge at N_{red}=12,000 rpm. Surge at N_{red}=12,000 rpm looks substantially like that occurring at N_{red}=10,000 rpm. Both have what appears to be fairly distinct instances of rotating stall separated by a region of undefined character which appears to contain some periodic pressure fluctuations. Further, both occur for approximately 0.6 seconds. The surge occurring at N_{red}=12,000 rpm shows more prominent mean pressure fluctuations than occur at N_{red}=10,000 rpm, indicating stronger reverse flow.

At 12,000 rpm operation, the mean pressure rises gradually until shortly after the end of the first apparent rotating stall. It then shows a

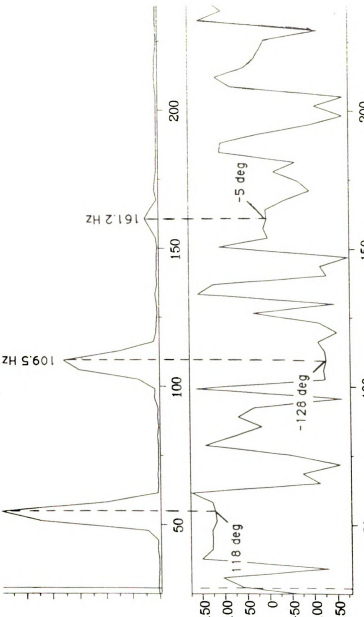

Fig. 4.7. Pressure & phase angle spectra for surge, N_{red}=10,000 rpm

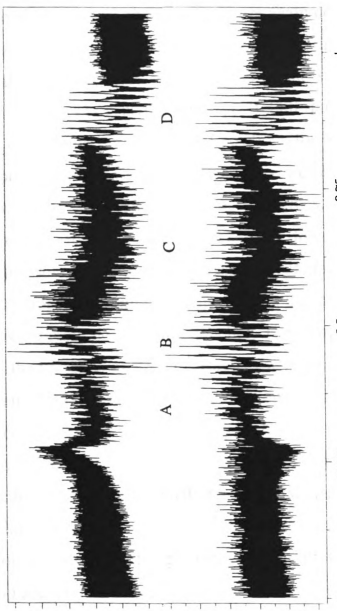

Fig. 4.8. Pressure-time signals for surge, N_{red}=12,000 rpm

marked drop until approximately the midpoint of surge, after which it rises until the beginning of the second rotating stall. With the onset of the second instance of rotating stall, the mean pressure again declines quickly, ending its descent with the termination of the second rotating stall. The mean pressure then recovers until the next surge event is triggered.

As with surge occurring for N_{red}=10,000 rpm, the surge events recorded at different circumferential positions for N_{red}=12,000 rpm look similar, but are not identical. The mean pressure behavior preceding surge at both positions differ radically. At ϕ_g=0 degrees, a short rise in mean pressure occurs, followed by an even sharper drop. Throughout this spike in mean pressure, blade-to-blade pressure oscillation amplitudes at the shroud line appear to diminish some, hinting that over this period, energy transfer is breaking down in the impeller. The sharp rise in mean pressure indicates the presence of strong reverse flow in the impeller channels (Pampreen, 1993). At approximately the same time that the 0 degree transducer is recording a sharp rise and fall in the mean pressure, the 125 degree transducer records a slight decrease in mean pressure, then an abrupt reduction in blade-to-blade pressure rise. Again, it appears energy transfer largely breaks down as the compressor enters surge.

Both pressure/phase angle and blade vibration analyses using the bench top analyzer indicate the presence of m=+1 rotating stall in surge events at N_{red}=12,000 rpm. However, the question remains: "Does the m=+1 rotating stall occur over the entire surge event, or only for discrete sections?" Signal analysis software provides a means for conveniently examining the details of each section of the surge event, whereas the logistics of capturing these details using the bench top analyzer prove cumbersome. To locate the actual occurrence of rotating stall with m=+1 in

the surge event, this investigation examined four sections of the surge signal shown in Figure 4.8. For convenience, these are labeled a, b, c, and d, as shown.

4.2.2.1 Section A

Section A, which lasts from t=0.225 seconds to t=0.4 seconds, is shown in more detail in Figure 4.9. It immediately precedes the first large pressure fluctuations, includes the sites where blade-to-blade pressure rises fall rapidly, and appears to contain some periodic pressure fluctuations. Analysis of section A shows mild pressure fluctuations in the 60 to 70 Hz range, but no identifiable rotating stall.

4.2.2.2 Section B

In contrast with section A, section B, which roughly corresponds to t=0.38 to 0.5 seconds, is composed of apparent rotating stall. Figure 4.10 shows the pressure-time signals, while Figure 4.11 shows the corresponding pressure and phase spectra obtained by performing a two channel FFT analysis on these two signals. Both the pressure-time and the pressure spectra reveal that pressure fluctuations for this section occur at varying frequencies. Due to variable oscillation frequency and short sample period (giving poor resolution), the pressure spectra show pressure peaks extending over wide frequency ranges. For example, the frequency peak which shows a maximum of 62.1 Hz has a base which extends from 36 Hz to 75 Hz. Nevertheless, we can use phase angle data to determine whether or not each of the pressure spectra peaks are caused by the same event. One should note, however, that although the same event causes all of the pressure spectra peaks, this fact is determined by analyzing the phase angle data near the f_p=89 Hz peak using that near the 62 Hz peak and by

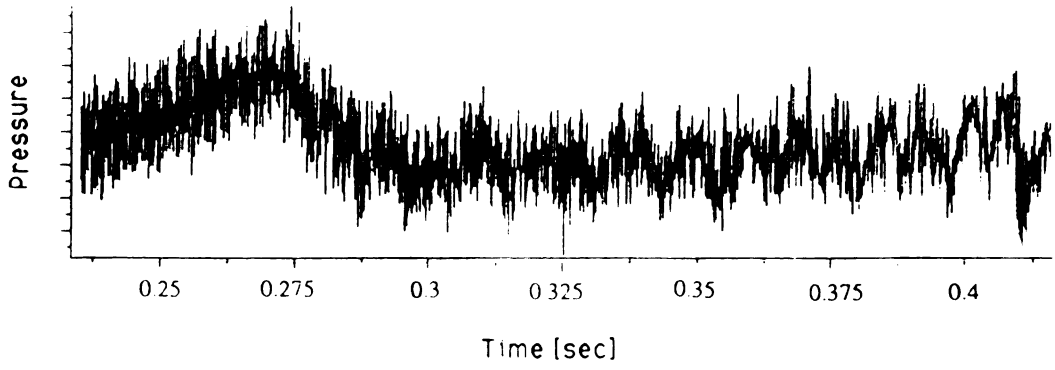

Fig. 4.9. Pressure-time signal for section A, N_{red}=12,000 rpm

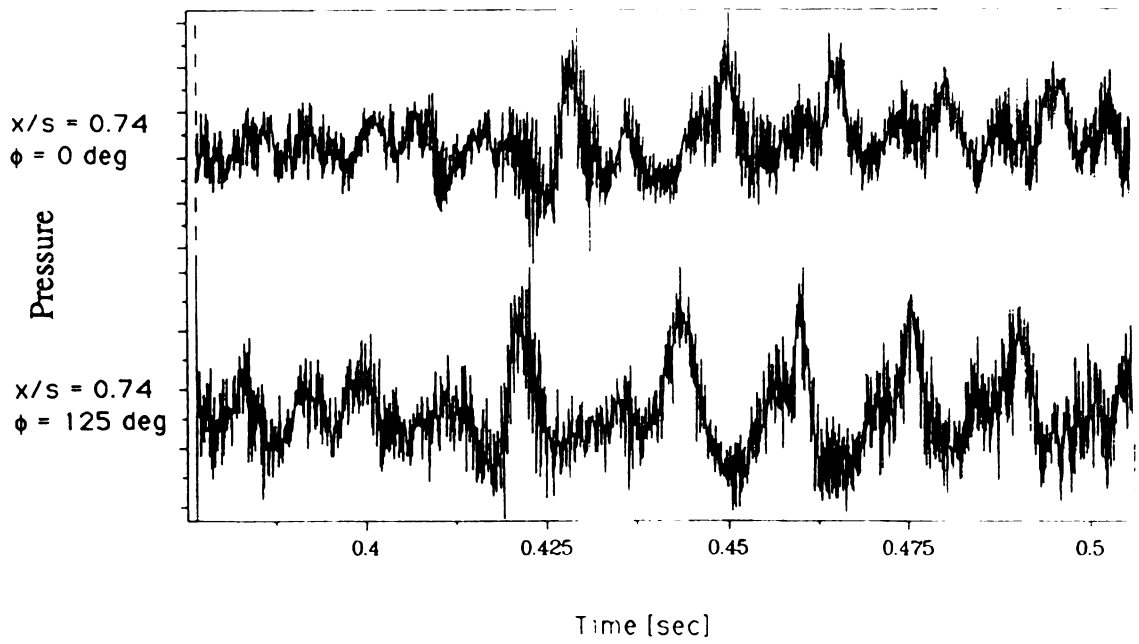

Fig. 4.10. Pressure-time signals for section B, N_{red}=12,000 rpm

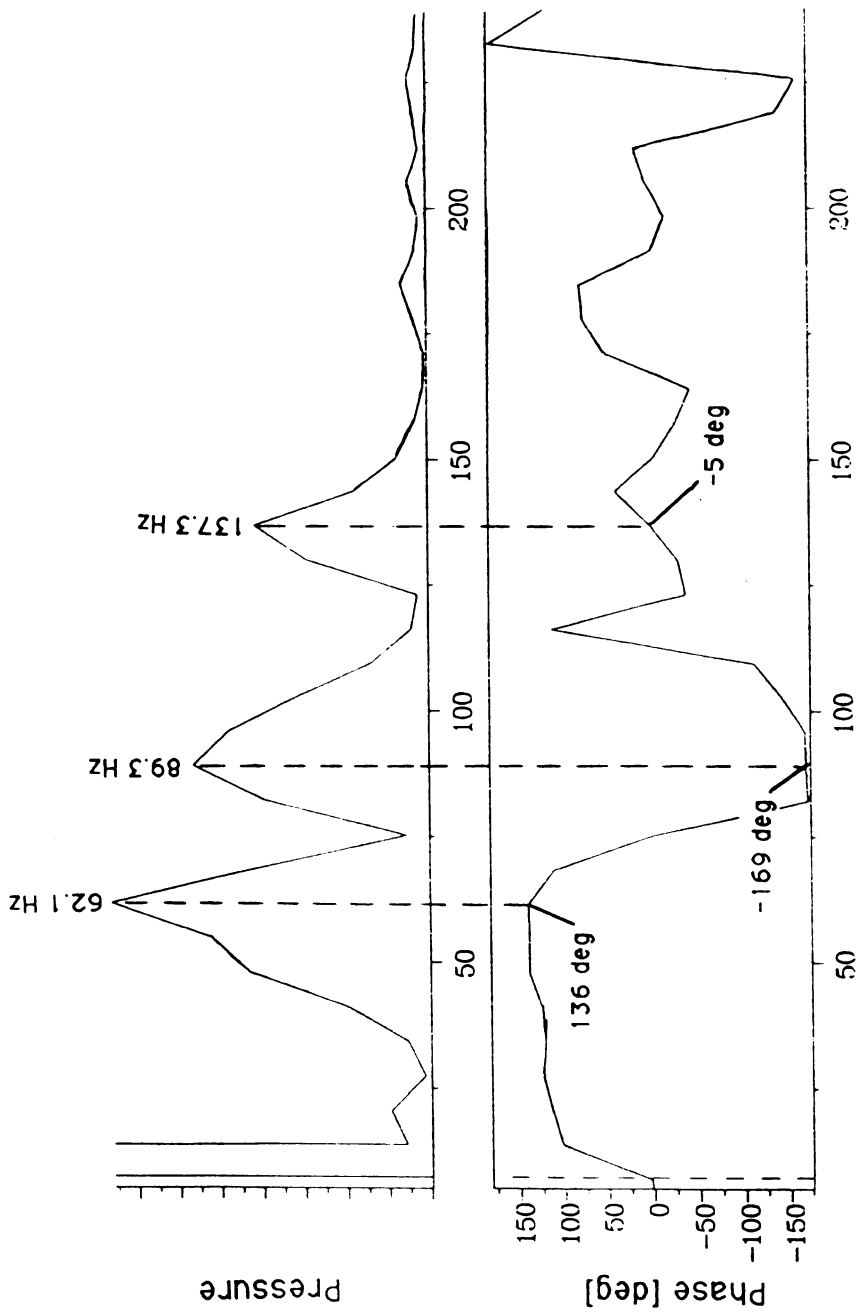

Fig. 4.11. Pressure & phase spectra for section B, N_{red}=12,000 rpm

analyzing the phase angle data near the f_p=137 Hz peak using that near 45 Hz.

Because the pressure peaks in the frequency domain vary so much and phase angles vary widely as well, we turn to blade vibration data for characterizing the stall for section B. Figure 4.12 shows the blade vibration spectra for section B of the surge. Neglecting peaks associated with the first mode, mild yet distinct blade vibration spectra peaks occur at 144 Hz, 766 Hz, 828 Hz, 1094 Hz, 1236 Hz, 1265 Hz, and 1408 Hz. The peaks at 828 and 1236 Hz are dismissed as harmonics of the shaft frequency (f_s=205 Hz). Analyzing the other peaks, and comparing the results with phase analysis results, we find three distinct possibilities regarding lobe number for the rotating stall under scrutiny: m=+1, m=+4 or m=-5. A comparison between these possibilities and those embedded in the pressure/phase analysis shows that of these three possible lobe numbers, results most closely confirm the m=+1 pattern. However, the imprecise nature of the empirical results argue for continued analysis to more conclusively establish the lobe number.

Jin, et al. (1992a) showed that blade vibration peaks not directly associated with rotating stall can occur due to circumferentially asymmetric rotating stall. This gives a means to narrow the possibilities found earlier for rotating stall of section B. According to Jin, et al. (1992a), circumferentially asymmetric rotating stall can induce distinct blade vibration peaks at any frequency given by the following equation:

$$f_b = M \cdot [(m \cdot f_s \pm f_p) + N \cdot f_s], \qquad (3\text{-}12)$$

where M and N are natural numbers. Since it appears that rotating events occurring between 45 and 62 Hz are responsible for all the interesting

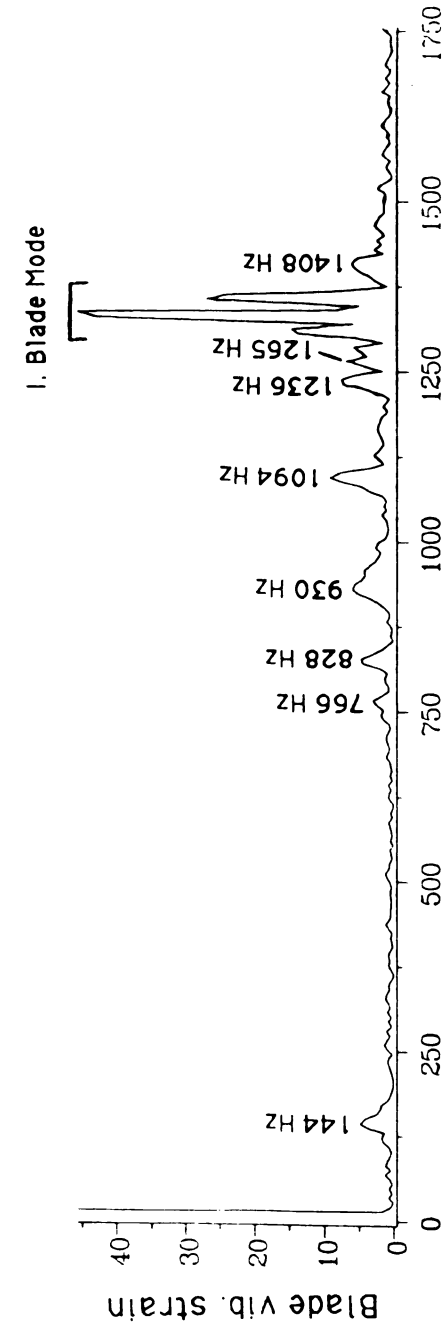

Fig. 4.12. Blade vibration spectra for section B, N_{red}=12,000 rpm

peaks in the pressure spectra, then we explore possible blade vibration spectra peaks from equation (3-12) using 45, 50, 55, and 62 Hz for f_p.

Tables 4.2(a) and 4.2(b) show blade vibration peaks calculated from (3-12) which lie within 10 Hz of measured blade vibration peaks. Both tables reflect results obtained for $-3 \leq M \leq 5$ and $-10 \leq N \leq 10$, which appears to be the important range for these constants (Jin, 1992a). Two tables were created to investigate variations brought about by small changes in shaft speed. Results shown in Tables 4.2(a) and 4.2(b) show that m=+1 best accounts for all of the blade vibration peaks measured. This confirms that the first rotating stall of the surge events for operation at 12,000 rpm is composed of a one-cell rotating stall rotating in the same direction as the rotor rotation. This also agrees with the results reported in Jin, et al. (1992b). Reporting results obtained from the same machine operated under a different configuration, Jin, et al. (1992b) indicated that all rotating stall found to occur during surge have one cell and rotate in the same sense as rotor rotation. In contrast to our findings, however, they also report rotating stall occurring just before surge (in the present investigation, we labeled this region A).

4.2.2.3 Section C

Section C, shown in Figure 4.13, forms the middle part of the surge event and corresponds to the pressure signal between t=0.5 to 0.82 s. (see Figure 4.8). It appears that this section contains distinct pressure fluctuations measured (from the time signal) to occur with a frequency of approximately 79 Hz. FFT analysis shows static pressure fluctuations at 82 Hz. Although a phase analysis reveals several possible modes of rotating stall occurring in this section, the blade vibration analysis indicates that no rotating stall occurs over section C. This result is found by noting from

TABLE 4.2 (a). Comparison of calculated blade vibration peaks with measured blade vibration peaks

fs=205 Hz

For fp=62 Hz:

	m=+1			m=+4			m=-5		
fb,meas.	M	N	fb,calc.	M	N	fb,calc.	M	N	fb,calc.
144	1	0	143	-1	5	143	1	6	143
766	1	3	758	1	0	758	-1	-1	758
930	5	-2	925						
1094	-1	6	1087	1	1	1087	-1	0	1087
1265	4	1	1273						
1286	-1	7	1292	1	2	1292	-1	1	1292
1408									

For fp=55 Hz:

	m=+1			m=+4			m=-5		
fb,meas.	M	N	fb,calc.	M	N	fb,calc.	M	N	fb,calc.
144	1	0	150	1	-3	150	-1	-4	150
766	1	3	765	1	0	765	-1	-1	765
930	2	2	930	2	-4	930	-2	-6	930
1094	5	-1	1095						
1265	3	4	1270				-3	-8	1270
1286	1	5	1285	1	2	1285	-1	1	1285
1408							-3	-9	1395

For fp=50 Hz:

	m=+1			m=+4			m=-5		
fb,meas.	M	N	fb,calc.	M	N	fb,calc.	M	N	fb,calc.
144	-3	3	150						
766	-3	6	765				-1	-1	770
	1	0	770						
930	2	3	925	2	-4	920	-2	-5	926
1094									
1265							-3	-8	1265
1286	1	5	1280	1	2	1280	-1	1	1280
	3	4	1285						
1408									

For fp=45 Hz:

	m=+1			m=+4			m=-5		
fb,meas.	M	N	fb,calc.	M	N	fb,calc.	M	N	fb,calc.
144	-3	3	135						
766	1	3	775	1	0	775	-1	-1	775
930	2	3	935	2	-3	935			
1094	3	3	1095	3	-6	1095	-3	-9	1095
1265	1	5	1275	1	2	1275	-1	1	1275
	4	3	1255	4	-9	1255			
1286									
1408	4	2	1410						

TABLE 4.2 (b). Comparison of calulated blade vibration peaks with measured blade vibration peaks

fs=203 Hz

For fp=62 Hz:

	m=+1			m=+4			m=-5		
fb,meas.	M	N	fb,calc.	M	N	fb,calc.	M	N	fb,calc.
144	1	0	141	1	-3	141	1	6	143
766	4	1	767						
930	2	2	936	2	-4	936			
1094	2	4	1094	2	-2	1094	-1	0	1087
1265	4	1	1263						
1286	1	5	1280	1	2	1280	-1	1	1292
1408	3	3	1404	3	-6	1404			

For fp=55 Hz:

	m=+1			m=+4			m=-5		
fb,meas.	M	N	fb,calc.	M	N	fb,calc.	M	N	fb,calc.
144	1	0	148	1	-3	148	1	6	148
766	1	3	757	1	0	757	1	9	757
	3	0	774						
930	-2	6	922						
1094	5	-1	1087						
1265	1	5	1273	1	2	1273	-1	1	1273
	-3	10	1256	3	-5	1256			
1286	5	0	1290						
1408	4	4	1404	4	-8	1404			

For fp=50 Hz:

	m=+1			m=+4			m=-5		
fb,meas.	M	N	fb,calc.	M	N	fb,calc.	M	N	fb,calc.
144	3	-3	150	1	-3	153	1	6	153
	1	0	153						
766	1	3	762	1	0	762	-1	-1	762
930									
1094									
1265	5	0	1265	1	2	1268	-1	1	1268
	1	5	1268						
1286									
1408	4	2		4	-10	1418			

For fp=45 Hz:

	m=+1			m=+4			m=-5		
fb,meas.	M	N	fb,calc.	M	N	fb,calc.	M	N	fb,calc.
144	3	-3	135						
766	1	3	767	1	0	767	-1	-1	767
930	2	3	925	2	-3	925	-2	-5	925
1094									
1265	1	5	1263	1	2	1263	-1	1	1263
1286	3	4	1286	3	-5	1286	-3	-8	1286
1408	4	2	1398	4	-10	1398			

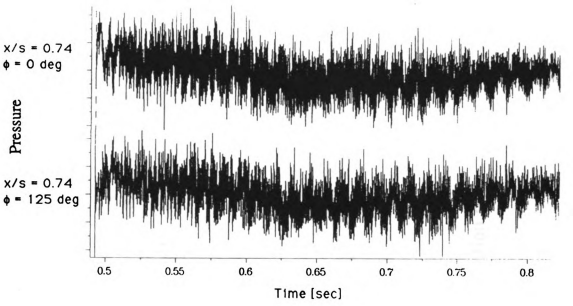

Fig. 4.13. Pressure-time signals for section C, N_{red}=12,000 rpm

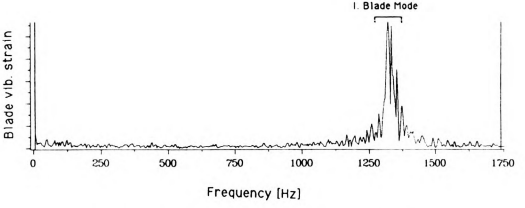

Fig. 4.14. Blade vibration spectra for section C, N_{red}=12,000 rpm

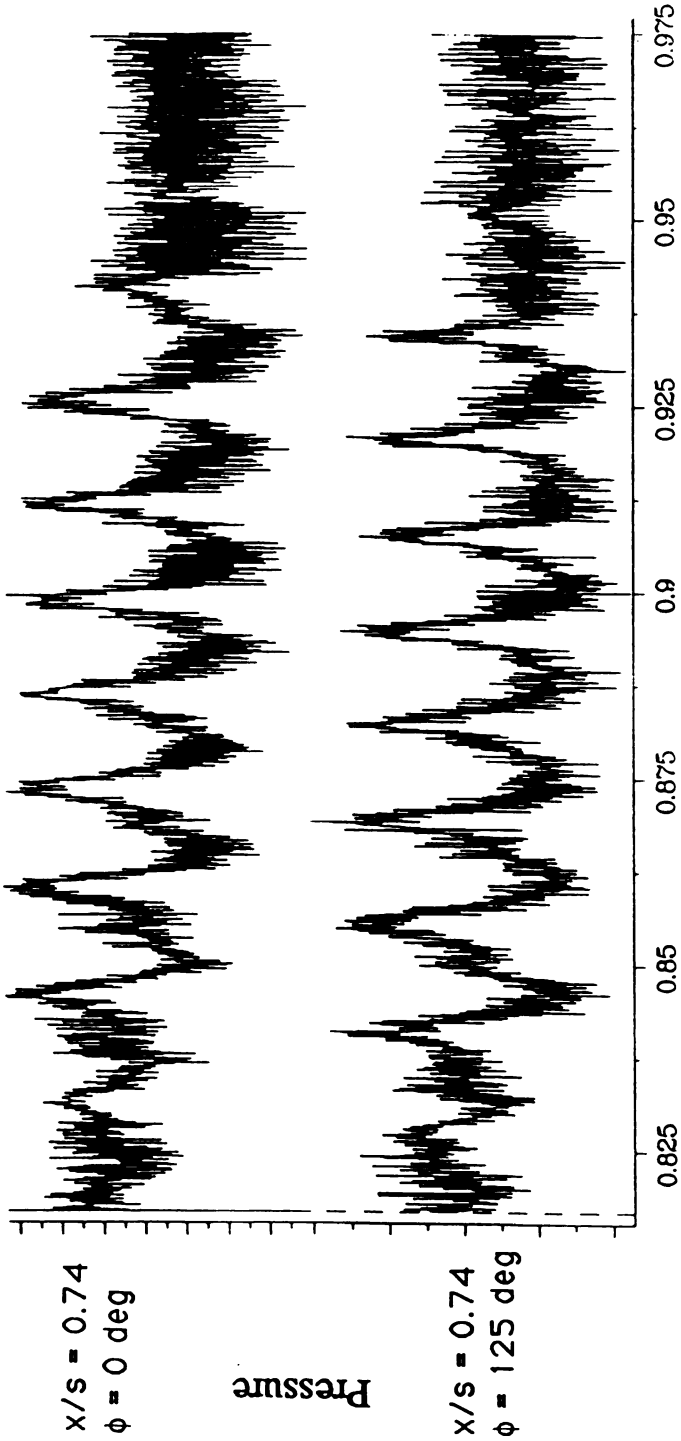

Fig. 4.15. Pressure-time signals for section D, N_{red}=12,000 rpm

Figure 4.14, that for this section no notable blade vibration peaks occur, except at those frequencies associated with the rotor's I. vibration mode.

4.2.2.4 Section D

Figure 4.15 shows the pressure-time signal for section D of the surge signal shown in Figure 4.8. Like section B, section D contains large amplitude pressure oscillations. The pressure and phase angle spectra for this section show that a very notable pressure peak occurs at 75.6 Hz. The peak is fairly wide, with its base extending from 62 to 88 Hz, due to the course resolution resulting from the small time scale of the analyzed section. For this peak, the phase angle lies in the 115 degree range and this can correspond to a number of modes of rotating stall as indicated in Figure 4.16, which presents the results of pressure/phase angle analysis for the entire event, for section B and for section D.

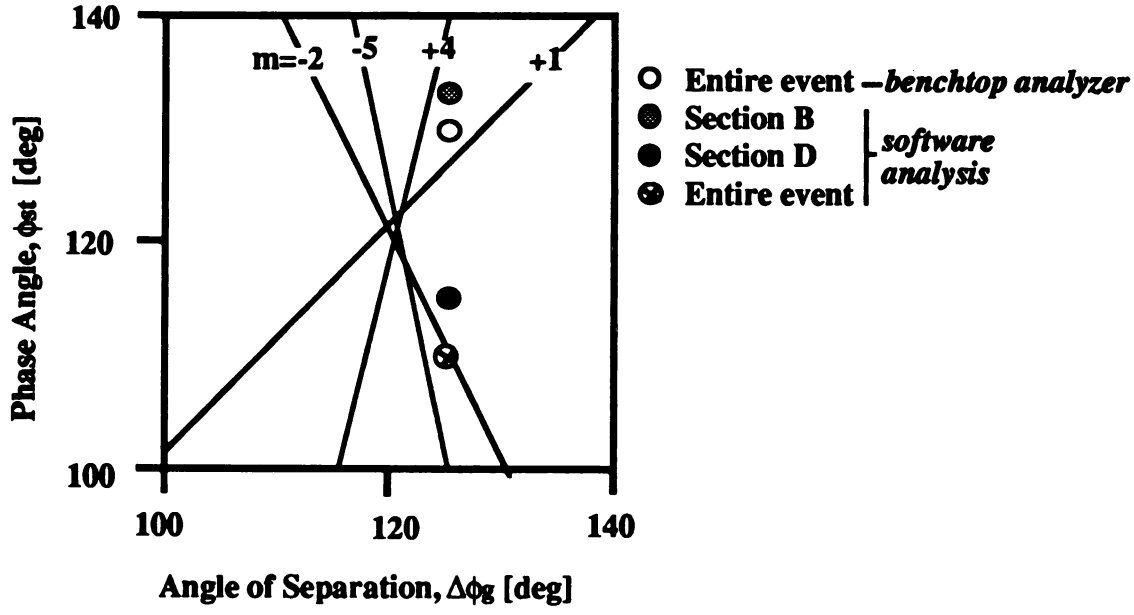

Fig. 4.16. Phase angle analysis for surge, Nred=12,000 rpm.

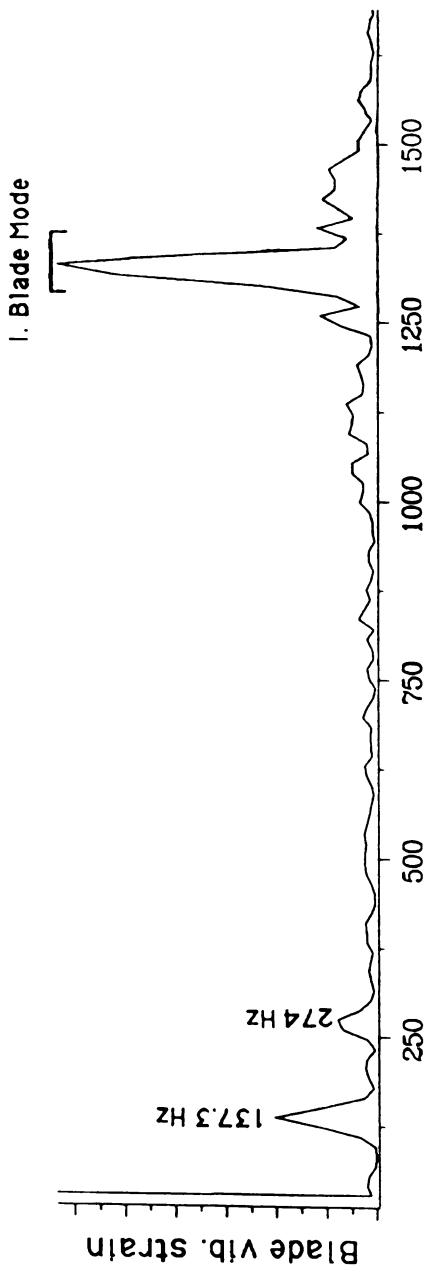

Fig. 4.17. Blade vibration spectra for section D, N_{red}=12,000 rpm

Blade vibration spectra give more information concerning which type of rotating stall was encountered in section D. Figure 4.17 shows that prominent blade vibration peaks occur at 137 Hz and in the frequency range corresponding to the first vibration mode. Analyzing these data gives the result that a rotating stall of m=+1 produces the oscillating pressure patterns of section D. Appendix F contains complete analytical results for the surge event pictured in Figure 4.8.

Knowing that m=+1, a review of Figure 4.16 shows how much more accurately the bench top analyzer captured the appropriate phase angle for an entire event than did the software. This may stem from the fact that probably a different surge event in the surge train was analyzed using the bench top analyzer than was analyzed using the software.

In summary, each surge event at both N_{red}=10,000 rpm and N_{red}= 12,000 rpm is composed of two segments of clear rotating stall separated by pressure unsteadiness of largely indeterminate character within which reasonably clear pressure oscillations reside. Within these intermediate sections, no rotating stall was detected. Comparing the results of analysis for the section as a whole with those obtained for its sub-sections reveals a dramatic variation in pressure, phase angle, and blade vibration spectra which occurs, depending on the portion of the recorded signal analyzed. Table 4.3 summarizes these results for N_{red}=12,000 rpm. Despite the differences, phase analysis did indicate possible modes of rotating stall; blade vibration analysis specifically showed which of these was the actual one. Blade vibration signals provided the most accurate means for determining the character of pressure oscillations recorded.

Table 4.3. Rotating stalls in surge at Nred=12,000 rpm

Event Section	Pressure Frequency fp	Lobe Number m	Propagation Speed ω_{st}/Ω
Entire	62 Hz	+1	0.302
A	60-70 Hz	--	--
B	50-62 Hz	+1	0.244-0.302
C	82 Hz	--	--
D	76 Hz	+1	0.371

4.3 Rotating Stall Characteristics

In contrast with operation at 10,000 rpm and 12,000 rpm, the compressor was not run to surge at N_{red}=14,000 rpm. Instead, intermittent rotating stall formed the limit to low flowrate operation. This investigation recorded four of these events, as shown in Figure 4.18. For convenience, these events are labeled A, B, C, and D. Using the software approach explained earlier, it was found that multiple modes of rotating stall occurred within each event. Rotating stalls with m=-3, m=+4, and m=+5 were definitely detected. In addition, it appears that in two instances,a weak m=-2 rotating stall may have occurred simultaneously with a m=-3 rotating stall. Highly irregular blade vibration spectral patterns were encountered. The following presents the details of the experimental findings regarding rotating stall at N_{red}=14,000 rpm.

4.3.1 Event A

Figure 4.19 shows the pressure-time trace of the first prominent instability recorded for N_{red}=14,000 rpm. The entire event appears to contain at least two, possibly three different rotating stalls and lasts for approximately 0.55 seconds (130 shaft rotations). Analysis of the time signal indicates that the pressure fluctuations forming the initial section of

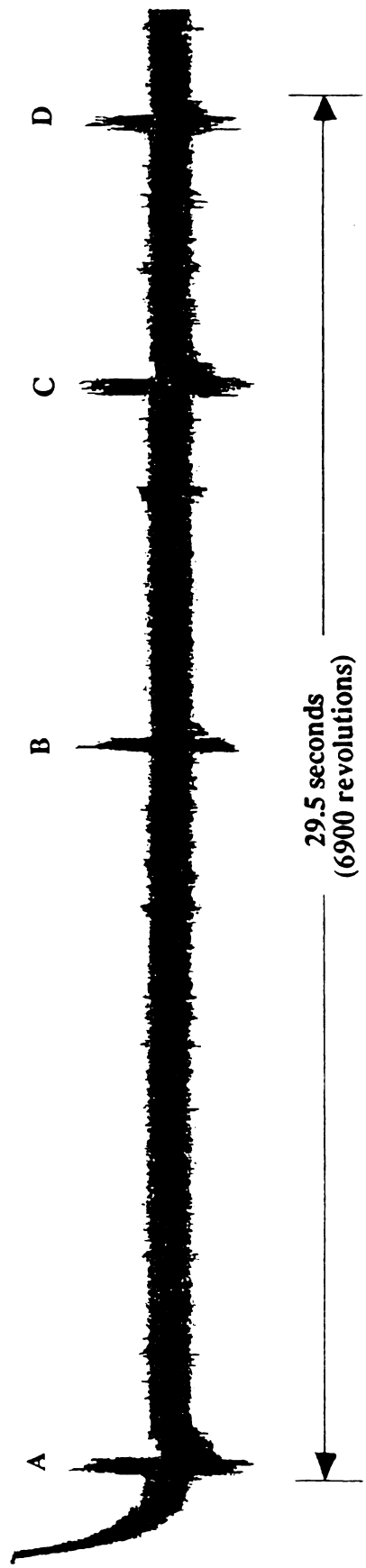

Fig. 4.18. Pressure Signal at Nred=14,000 rpm, x/s=0.74

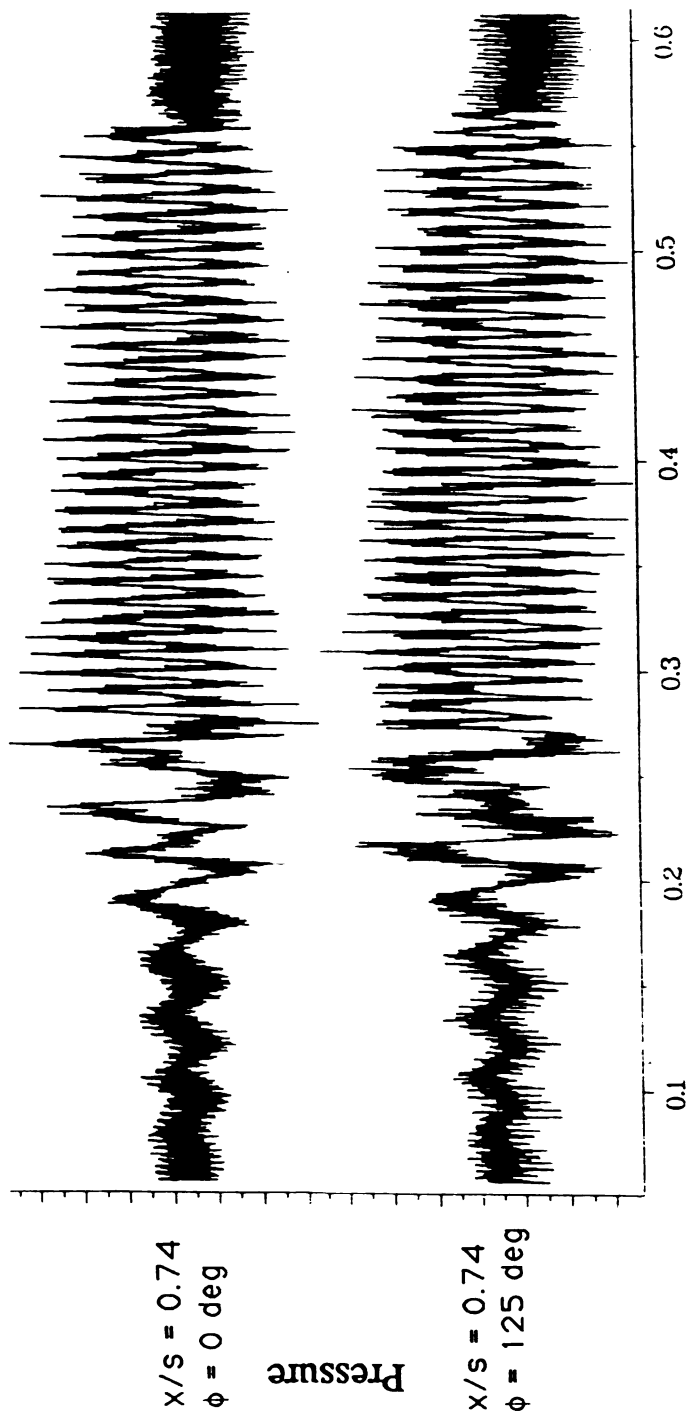

Fig. 4.19. Pressure-time signals for event A, N_{red}=14,000 rpm

the event begins with mild amplitude and variable, but low frequency. They then quickly increase in both amplitude and frequency up to t=0.28 s., at which point a new type of rotating stall appears to emerge. This new mode of rotating stall occurs with large pressure fluctuations and comparatively high frequency.

4.3.1.1 First rotating stall

The initial section of event A was investigated using a phase angle and blade vibration spectral analysis to determine the presence and character of any rotating stalls present. Figure 4.20 shows the pressure and phase angle spectra for this section of event A. A phase angle analysis performed using software revealed two possible modes of rotating stall here: m=+3 and m=-3.

To pinpoint the character of the first rotating stall occurring in event A, we turn to a blade vibration analysis. Figure 4.21 shows the blade vibration response for the 0.1 s.$\leq$t$\leq$0.28 s. section of event A depicted in Figure 4.21. This interval corresponds to approximately 40 rotor rotations. Several prominent peaks appear in the blade vibration spectra; however, most of these (viz., 718, 952, 1191, and 1430 Hz) can be accounted for as multiples of the shaft frequency (f_S=239.6 Hz) and can be dismissed as not resulting from rotating stall. After these peaks are dismissed, only one unexplained prominent peak remains: that at 753 Hz. This peak corresponds to m=-3. Since this agrees with one of the possibilities uncovered by the phase analysis, the investigator can justifiably conclude that the first rotating stall in event A had three lobes (cells) and rotated in a direction opposite to that of the rotor. Applying equation (3-13) reveals that for this mode of rotating stall ω_{St}/Ω=0.048. Interestingly, this mode of

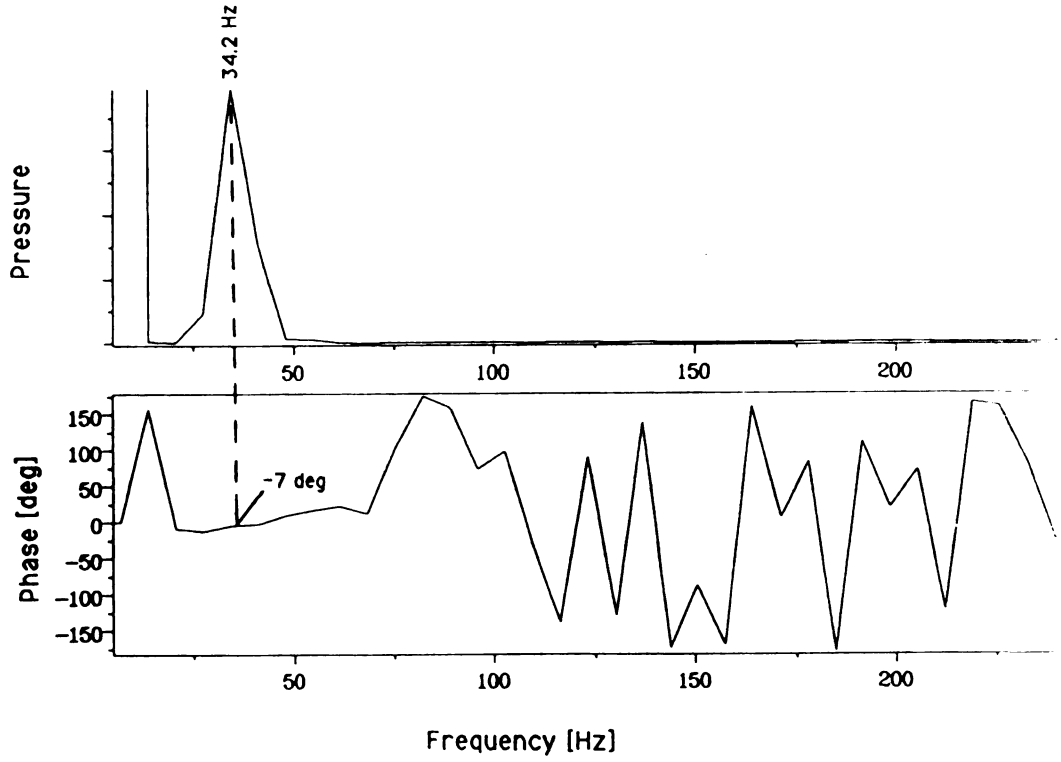

4.20. Pressure & phase spectra for first rotating stall in event A, N_{red}=14,000 rpm

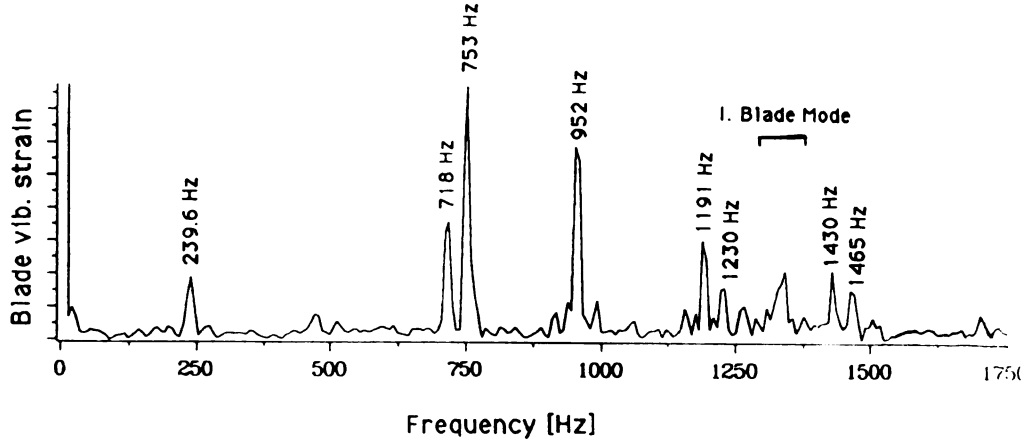

Fig. 4.21. Blade vibration spectra for first rotating stall in event A, N_{red}=14,000 rpm

rotating stall did not greatly excite blade vibrations at the rotor's I. vibration mode.

4.3.1.2 Second rotating stall

The second rotating stall of event A begins at approximately t=0.28 s., as represented in Figure 4.19. Measurements of wavelength from the time signal indicate that pressure oscillated with a frequency of 116 Hz in this section, while the pressure spectra for this section shows a clear peak occurring at f_p=116.5 Hz with a corresponding phase angle of -105 degrees. Again, phase angle analysis reveals several possible modes for this rotating stall: m=+5, m=+2, and m=-1.

Figure 4.22 shows the blade vibration spectra for the second rotating stall of event A. Unlike the first rotating stall of event A, the second rotating stall does not show a number of prominent peaks in blade vibration spectra over a wide range of frequencies. Instead, this rotating stall excites prominent blade vibrations at 1087 Hz, 1238 Hz, and those frequencies associated with the blades' I. Mode. Dismissing the I. Mode frequencies and performing a blade vibration analysis, we find that the 1087 peak can correspond to rotating stalls with either m=+5 or m=-4. Comparing this with results obtained from the phase analysis suggests that the second rotating stall in event A had m=+5. For this mode of rotating stall, we find ω_{st}/Ω=0.098.

The source of the 1238 Hz peak is unknown. This peak does not correspond to a multiple of the shaft frequency, a multiple of the system noise frequency (50 Hz), or a result of a circumferentially asymmetric rotating stall. Sometimes vibration peaks lying near those of the I. Mode are amplified due to their proximity to vibration frequencies of the I. Mode. Possibly, the prominence of the 1238 Hz peak results from its

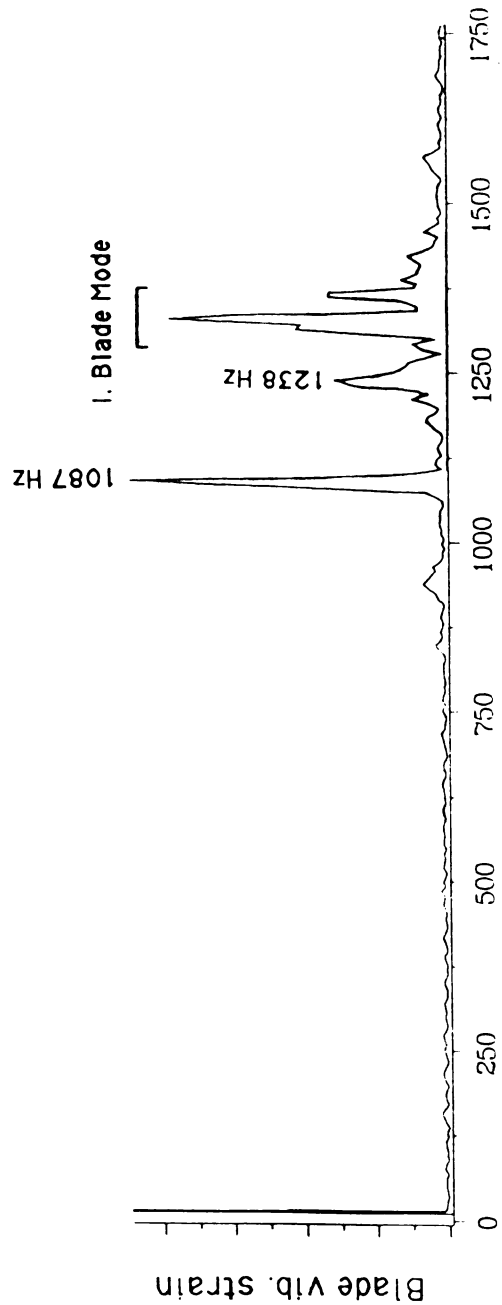

Fig. 4.22. Blade vibration spectra for second rotating stall in event A, N_{red}=14,000 rpm

proximity to the I. Mode. However, with the given data, no conclusive determination of its origin can be established beyond identifying this possibility. Nevertheless, the fact that this peak lies 151 Hz from the principal blade vibration peak is significant. As it turns out, this sort of extraneous peak shows up in blade vibration signals for the other events recorded for N_{red}=14,000 rpm, too.

Signal analysis software proves very useful for rapidly changing occurrences such as event A. Analysis conducted using the bench top FFT analyzer produced results only for the second rotating stall, as can be seen from Appendix F. However, once the existence of the m=-3 rotating stall was established using a software approach, it was possible to find this rotating stall with the bench top analyzer. Nevertheless, this required several trials and the operator had to activate the analyzer at precisely the correct moment to detect this mode of rotating stall. This illustrates the usefulness of the software approach over the bench top approach for investigating these very brief events.

4.3.2 Event B

The pressure-time signal for event B, pictured in Figure 4.23, shows that this event appears to consist of a mode (or modes) of rotating stall giving somewhat varying frequencies in pressure oscillations. It turns out that the character of the rotating stall(s) occurring in event B is very difficult to conclusively establish.

Figure 4.24 shows the pressure and phase angle spectra for event B. Shown are three distinct pressure peaks centered at 48 Hz, 83 Hz and 129 Hz, respectively. Analysis using the bench top analyzer revealed a strong peak at 45 Hz, with weaker peaks at 85 Hz and 131 Hz. Each had a coherence reading of 0.98 to 1.0. The weakness of the 83 Hz and 129 Hz

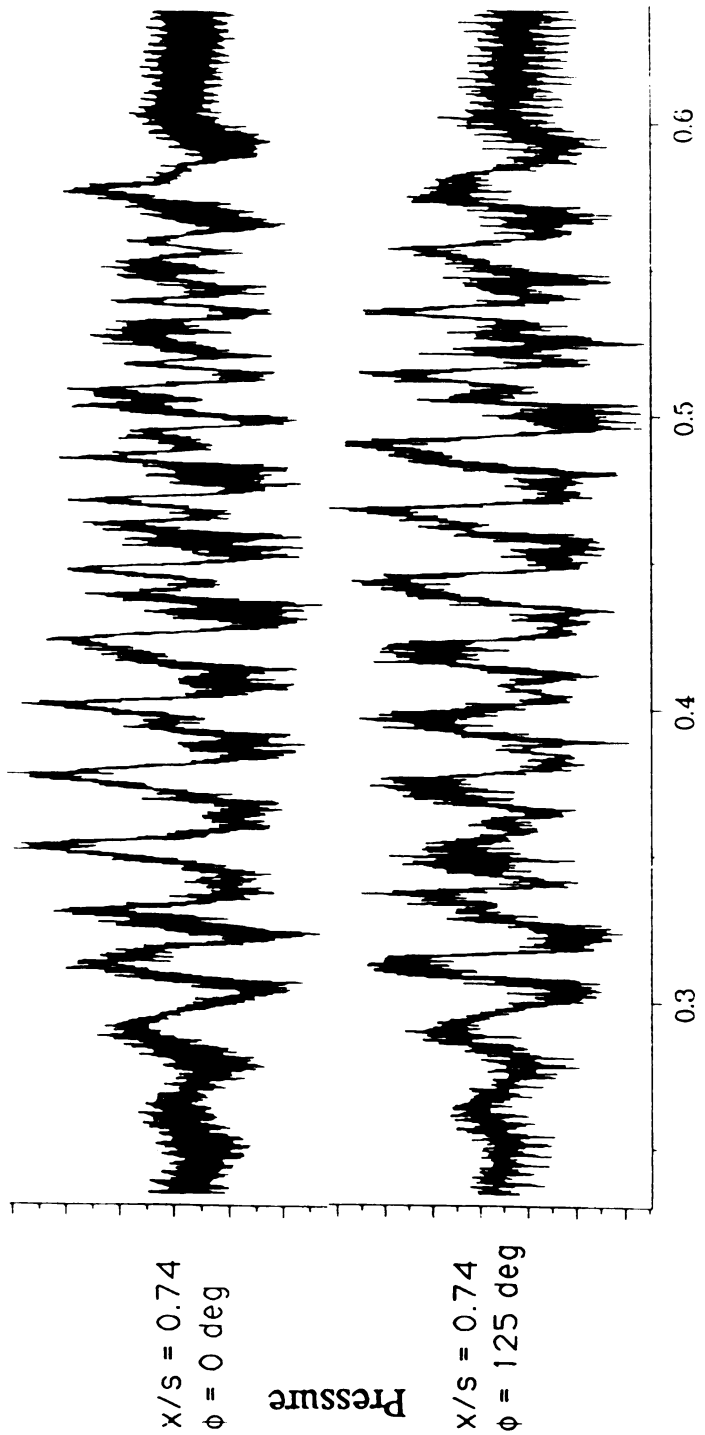

Fig. 4.23. Pressure-time Signals for event B, N_{red}=14,000 rpm

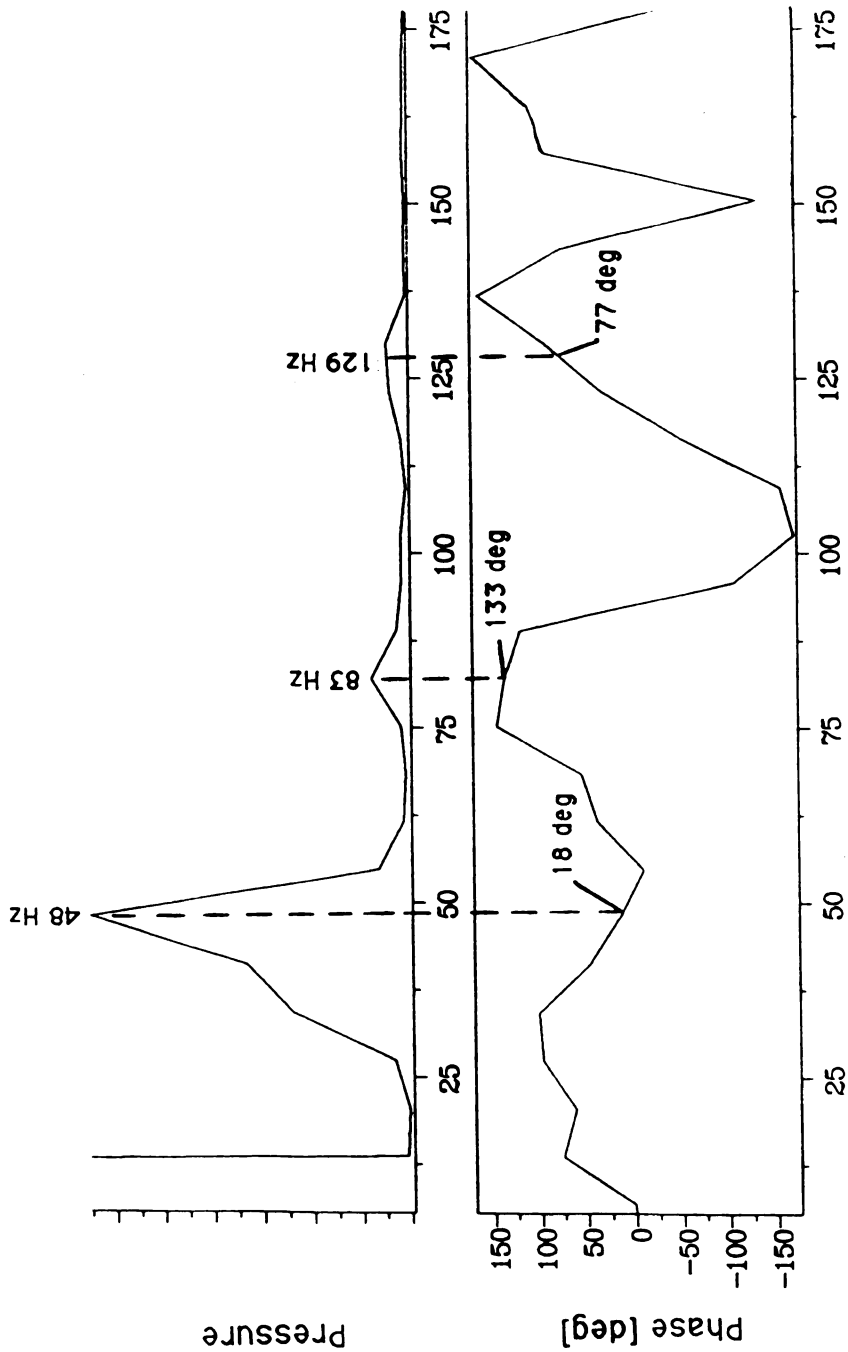

Fig. 4.24. Pressure & phase spectra for first segment of event B, N_{red}=14,000 rpm

peaks motivates us to ignore them for now and to concentrate on the 48 Hz oscillation.

Focusing on the 48 Hz peak, we notice that the phase angles recorded for this peak vary dramatically over its base from 98 degrees to -10 degrees. For transducers spaced 125 degrees apart, it follows from equation (3-10) that rotating stalls can only give phase angles as follows:

$\|m\|$	$\|\Delta f_{st}\|$
7	155
6	30
5	95
4	140
3	15
2	110
1	125

Since no rotating stalls occur for phase angles between 30 and 95 degrees and since the phase angle represented at different frequencies will actually be correct only for those locations corresponding to rotating stall, then we can neglect the portion of the 48 Hz peak with phase angles located in this range. Thus, we can neglect the area between 35 and 45 Hz.

Noticing that below 35 Hz the amplitude of the pressure peak is low, we turn our attention to those portions of the peak between 45 and 50 Hz. It appears that this section of the peak most likely represents the effects of rotating stall. A phase analysis for the sections of the 48 Hz peak where rotating stall may occur reveals that several possible modes of rotating stall can correspond to pressure oscillations with this frequency: m=-3, m=+3, m=-5, and m=-2. In order to narrow the field of possible rotating stall modes, a comparison between the results of the phase analysis and results obtained from a blade vibration analysis is helpful.

Before moving to the blade vibration spectra, we first determine if the 83 Hz and 129 Hz pressure peaks are related to the 45 Hz peak in the pressure spectra. Recall that this can be done by examining the phase angles involved and noting if the phase angles of the higher frequency peaks are the appropriate multiple of the phase angles of the lower frequency. As noted, for this event analysis must focus on the portion of the 48 Hz peak between 45 Hz and 50 Hz. In this range, the 48 Hz peak contains phase angles of between -15 to 30 degrees. Calculating for the 83 Hz peaks we find that in order for the two peaks to be related, the 83 Hz peak must contain a phase angle between -28 and 57 degrees. Since the 83 Hz peak does not contain a phase angle reading in this range, we conclude that the 83 Hz peak and the 48 Hz peak are not directly caused by identical physical events. Similar procedures reveal that the 129 Hz peak is not directly caused by the same event as causes the 48 Hz peak. It appears, then, that three distinct pressure fluctuations were detected which are not directly caused by the same event.

Figure 4.25 shows that the blade vibration strain spectra for event B contains several distinct peaks. Of these, the peak at 157 Hz may be dismissed as a "false" peak arising as an aliased signal of the blades' II Mode. The 1204 Hz and 1682 Hz peaks can be dismissed also. These arise as harmonics of the shaft frequency (239 Hz).

To avoid false peaks in signal analysis, digitizing must conform to the sampling theorem: $f_{sa} \geq 2f_{si}$, where f_{sa} is the sampling frequency and f_{si} is the frequency to be analyzed. In this investigation, f_{sa}=3474 Hz. Under the conditions of this investigation, any peaks residing in blade vibration spectra between 1737 Hz (fsa/2) and 3474 Hz will be reflected back and show up as "false" peaks in the blade spectra. In our case, only one

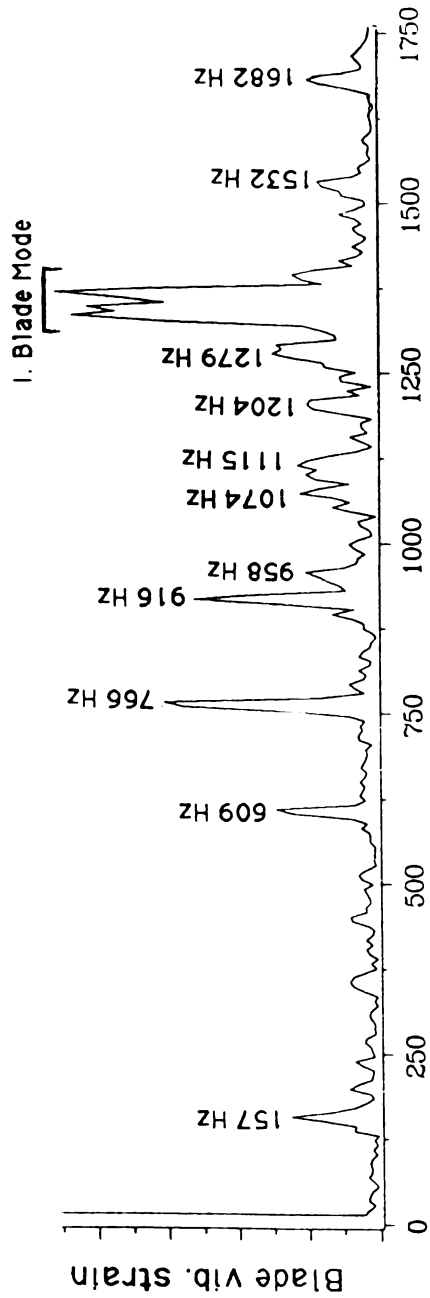

Fig. 4.25. Blade vibration spectra for event B, N_{red}=14,000 rpm

significant peak occurred in this frequency range: the vibrations near 3320 Hz associated with the blades' II mode. The difference between these frequencies shows up as the false peak at 157 Hz (i.e., 3474-3320=154).

An FFT analysis of the digitized signal between t=0.1 s. and t=0.26 s, which corresponds to the section wherein significant pressure oscillations first begin, shows no peaks near 157 Hz. Blade response for this section only shows excitation of frequencies corresponding to multiples of the shaft frequency and excitation of blade vibration near f_b=745 Hz. Given $f_p \approx$ 40 Hz, f_b=745 Hz probably corresponds to an emerging m=-3 rotating stall. This m=-3 rotating stall produced the f_b=766 Hz peak in Figure 4.27. We leave the explanation of the remaining blade vibration strain spectra peaks until later.

Several possibilities emerge for explaining the causes of the three peaks shown in Figure 4.25. Of these, the following are investigated: (1) All three pressure spectra peaks are caused by distinct physical events (e.g., rotating stall) operating in series. (2) Distinct physical events occurring concurrently produce the 48 and 83 Hz pressure spectra peaks and produce the 130 Hz peak as an artifact. (3) Distinct physical events cause the 48 and 130 Hz pressure spectra peaks, while the 83 Hz pressure peaks is produced as an artifact of these two peaks.

4.3.2.1 Possibility #1

The first possibility to explore is that all three peaks in the pressure spectra are caused by distinct modes of rotating stall occurring in series. Table 4.4 presents the results of the pressure/phase angle and blade vibration analyses for this situation. It shows that a m=-3 rotating stall may cause the 48 Hz peak, no rotating stall causes the 83 Hz peak, and a m=+3, m=+6, or m=-2 rotating stall may cause the 129 Hz peak.

TABLE 4.4. ANALYSIS OF EVENT B, N_{red}=14,000 rpm

	PHASE ANALYSIS			BLADE VIB. ANALYSIS	
Analyzer	f_p [Hz]	ϕ_{st} [deg]	Possible m-values	f_b [Hz]	Calculated m-values
DIA/DAGO	48	18	**m=-3**	609	--
			m=+3	766	**m=-3.00**
			m=+6	916	m=+4.03
				1334	I. Mode
				1347	I. Mode
				1368	**m=+5.91** and I. Mode
DIA/DAGO	83	133	m=-2	609	m=+2.09
			m=+1	766	--
			m=+4	916	--
				1334	m=+5.91 and I. Mode
				1347	m=+5.96 and I. Mode
				1368	m=+6.06 and I. Mode
DIA/DAGO	129	50-100	**m=-5**	609	**m=-2.01** or
			m=+1		m=+3.09
			m=+4	766	--
			m=-2	916	--
				1334	**m=-5.03** and I. Mode
				1347	m=-5.08 and I. Mode
				1368	I. Mode
FFT Analyzer	45	4	**m=-3**	762	m=-3.01
			m=+3		
FFT Analyzer	85	154	m=+4		
			m=+7		
FFT Analyzer	131	128	**m=-2**		
			m=+1		
			m=+4		

The readings from the FFT analyzer recorded in Table 4.7 for 45 Hz and 131 Hz appear slightly more accurate than those obtained from the software. However, the phase angle ($\Delta\phi_{st}$) for the 85 Hz peak disagrees strongly with the probable value.

From consideration of the blade vibration spectra, the m=+6 pattern can be dismissed from consideration. It is well known that the I. Mode will often amplify vibrations lying near it in the frequency domain. The fact that the blade vibration peak corresponding to m=+6 lies close to the I. Mode and shows mild amplitudes motivates dismissal of this stall pattern from the list of suspected rotating stalls. The prominence of the 1368 Hz peak likely results as a consequence of its being amplified by the nearby I. vibration mode of the blades. Further, the m=-2 and m=+3 modes of rotating stall correspond to a more distinct, larger peak in the blade spectra and, therefore, constitute more likely candidates.

The above-mentioned modes of rotating stalls, if assumed to be circumferentially asymmetric, can account for all of the peaks encountered in the blade vibration spectra. Separately, no one mode of rotating stall explains all of the blade vibration peaks. Collectively, however, they do. Table 4.5 shows which peaks the different modes of rotating stall account for. The m=-2 hypothesis combined with an identified m=-3 rotating stall accounts for all of the observed blade vibration spectral peaks, whereas the m=-5 hypothesis does not.

Although positing the occurrence of several distinct modes of rotating stall accounts for the pressure and blade spectra data, it appears that this scenario does not in fact occur. Examination of the pressure-time signal given in Figure 4.23 does not reveal three, or even two distinct rotating stalls at different frequencies occurring in series. Instead, what

Table 4.7. EXPLANATION OF BLADE VIBRATION PEAKS DUE TO DIFFERENT STALL MODES

	f_p=48 Hz		f_p=129 Hz	
f_b peak	m=-3	m=+6	m=-5	m=-2
609			x	x
766	x	x		x
916	x	x		
1074				x
1101	x	x		
1115				x
1279				x
1292	x	x	x	
1395	x	x		
1532	x	x		x

appears are two pressure fluctuations with one clearly dominating the other and withthe weaker signal growing in strength as time elapses. This is what we would expect for distinct, simultaneous static pressure oscillations as may occur with the presence of concurrent rotating stalls. But, the complicated nature of pressure oscillations make time-domain analysis relatively infertile ground for producing meaningful results.

4.3.2.2 Possibility #2

The second possibility to consider posits that two pressure oscillations occur simultaneously, corresponding to the 48 and 83 Hz pressure spectra peaks, respectively. In acoustics, which deals with pressure waves, when two tones are produced simultaneously, the human ear will hear tones corresponding to their individual frequencies, a tone corresponding to the sum of their frequencies, and a tone corresponding to the difference of their frequencies. Using this as an analogy, possibility #2 proposes that the 129 Hz peak occurs as a by-product of the superimposed pressure oscillations at 48 and 83 Hz. However, FFT analysis of physical signals does not operate as does human hearing. All three pressure peaks which

show up in the FFT analysis have direct sources in the physical signal. Therefore, possibility #2 must be rejected.

4.3.2.3 Possibility #3

The third possibility to explore supposes that two modes of rotating stall occur simultaneously and that these two rotating stalls show up in the pressure spectra as peaks at 48 Hz and 130 Hz. According to this possibility, the 83 Hz signal occurs as a by-product of these two frequencies (83 Hz =131 Hz-48 Hz). As with possibility #2, possibility #3 derives from an analogy with acoustics and human hearing. Discussion from possibility #2 argues that we must abandon the notion that the 83 Hz peak derives from the others.

The time signal hints that two distinct pressure oscillations occur simultaneously. This agrees with both the pressure and blade vibration spectra data. Close examination of the pressure-time signal shows a 45 Hz oscillation dominating a superimposed 125 Hz oscillation. No oscillations at 83 Hz appear.

The discussion of possibility #1 suggested that pressure oscillations giving rise to the multiple blade spectra peaks occur throughout the entire event. It also showed that only by assuming the m=-3 rotating stall and the m=-2 rotating to be asymmetric could all of the blade peaks be accounted for. Asymmetries most often arise due to the influence of the compressor exit. The exit produces a circumferential distortion of the pressure field felt in the compressor and probably thereby influences the amplitude of pressure oscillations associated with rotating stall cells as these travel circumferentially. For simultaneous rotating stalls, the presence of the other rotating stall would represent a circumferential distortion in static pressure and would likely produce circumferential static pressure

amplitude variations for that rotating stall. Consequently, if two rotating stalls occur simultaneously, they both can be expected to be circumferentially asymmetric.

4.3.2.4 Possibility #4

A fourth alternative simply dismisses the 83 and 129 Hz pressure peaks as insignificantly small. Under this assumption, the unexplained peaks in the blade strain spectra must be accounted for as resulting from either the m=-3 rotating stall with f_p=48 Hz or as "false" signals arising from the non-linear nature of the system under analysis.

Non-linear oscillations sometimes give rise to unusual peaks in frequency spectra which arise from the non-linearity of the system. This occurs when oscillations interact in such as way as to modulate each other. This can be illustrated by observing that $A \sin(x) \cdot B \sin(y) = (A \cdot B/2) \cdot [\cos(x-y) \pm \cos(x+y)]$, where A, B, and C are constants. This trigonometric identity shows how one oscillation (sin(x)) modulates a separate oscillation (sin(y)) and produces two superimposed oscillations which combine the frequencies of the original signals. In the system under investigation here, an oscillation at 157 Hz peak may have modulated one at 766 Hz, producing peaks at 766 Hz+157 Hz (913 Hz) and 766 Hz-157 Hz (609 Hz).

Alternatively, these peaks may arise due to aliasing of vibrations occurring at frequencies higher than those explored here. In this case, the 157 Hz peak also arises as an aliased signal.

In summary, the principal rotating stall found in event B had three cells and rotated counter to the rotor rotation with ω/Ω=0.067. Possibly, a much weaker m=-2 rotating stall rotating with ω_{st}/Ω=0.27 occurs simultaneously with the m=-3 stall. However, such simultaneous rotating

stalls have not been reported in the literature. Consequently, the hypothesis of the simultaneity of stalls must be viewed with considerable skepticism.

4.3.3 Event C

Like event A, it appears that event C is composed of two distinct rotating stall patterns occurring in series. Figure 4.26 shows the pressure time signal obtained for this event from the two transducers at x/s=0.74. It shows that event C occurs for about 0.4 seconds (130 rotor revolutions). Analysis of the time signal shows that the first 0.15 seconds of the event contains pressure fluctuations oscillating near 48 Hz, while the rest of the event contains pressure fluctuations with frequencies near 21 Hz. The analysis of these two segments is straightforward.

4.3.3.1 First rotating stall

Figure 4.27 shows the pressure and phase angle spectra for the first segment of event C and shows a fairly wide, prominent pressure peak with maximum amplitude at 48 Hz. For the majority of this peak, phase angle ($\Delta\phi_{st}$) remains fairly level. A pressure/phase angle analysis reveals that this pressure peak is likely caused by one of three rotating stall patterns: m=+3, m=-3, or m=+6. Analysis of the blade vibration spectra helps determine which of these is correct.

The blade vibration spectra are shown in Figure 4.28. Each of the prominent peaks in this Figure may be shown to correspond to the I. blade mode, a multiple of the shaft frequency, or the result of a circumferentially asymmetric rotating stall pattern with m=-3 or m=+6. Therefore, we narrow our considerations to the m=-3 and m=+6 modes of rotating stall. These correspond to prominent blade vibration peaks at f_b=767 Hz for m=-3 and f_b=1382 Hz for m=+6.

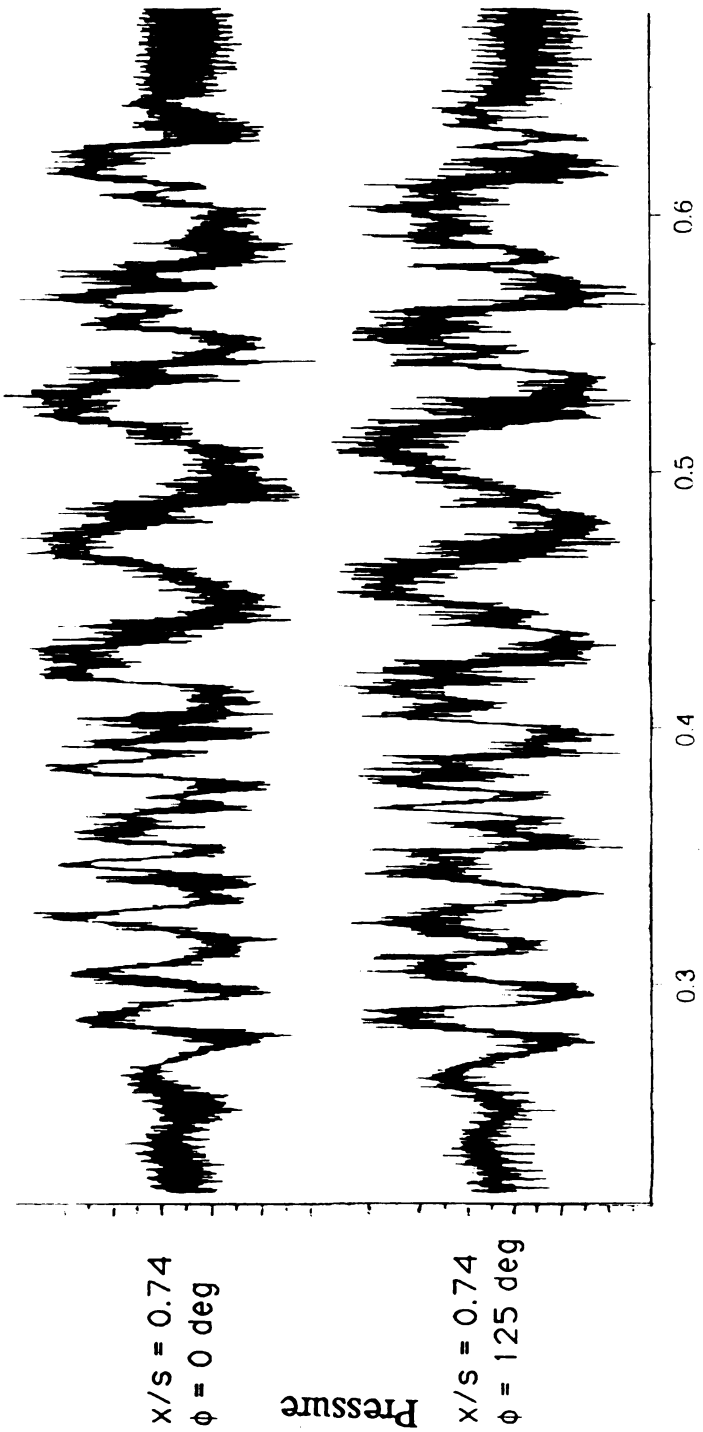

Fig. 4.26. Pressure-time signals for event C, N_{red}=14,000 rpm

As already noted, the I. mode of the rotor often amplifies signals lying near it in the frequency domain. Consequently, we can explain the prominence of the 1382 Hz peak--whose existence can be attributed to the circumferential asymmetry of the m=-3 stall mode--to its proximity to the I. Mode of the blades. This, together with an examination of results obtained with the bench top analyzer (see appendix F) argues for the elimination of the m=+6 pattern from consideration. Therefore, it appears that the first rotating stall pattern has m=-3 and ω_{st}/Ω=0.067.

4.3.3.2 Second rotating stall.

The pressure and phase angle spectra for the second pressure fluctuation occurring in event C shows a very clear peak occurs at f_p=21 Hz. A pressure/phase angle analysis shows that the pressure peak was likely caused by a stall pattern with m=-2, m=+1 or m=+4. Comparison with the results of a blade vibration analysis confirms that the rotating stall has four cells rotating in the same direction as the rotor with ω_{st}/Ω=0.022.

Figure 4.27 shows the pressure and phase angle spectra for the m=-3 rotating stall. Note the difference between the recorded phase angles and the actual phase angle corresponding to the identified mode of rotating stall. According to equation (3-10), a m=-3 rotating stall should give rise to $\Delta\phi_{st}$=-15 deg. However, the phase angle recorded here is $\Delta\phi_{st}$=-1 degree from the software and -7 degrees from the bench top analyzer. Furthermore, from Figure 4.27, it appears that for the pressure peak in question, the phase angle never reaches -15 degrees. Error in measuring $\Delta\phi_g$ could account for discrepancies between measured phase transfer angles and expected phase angles. If this were the case, however, the measured angle values would deviate from the expected values in a consistent way. For example, measured phase angles would always either

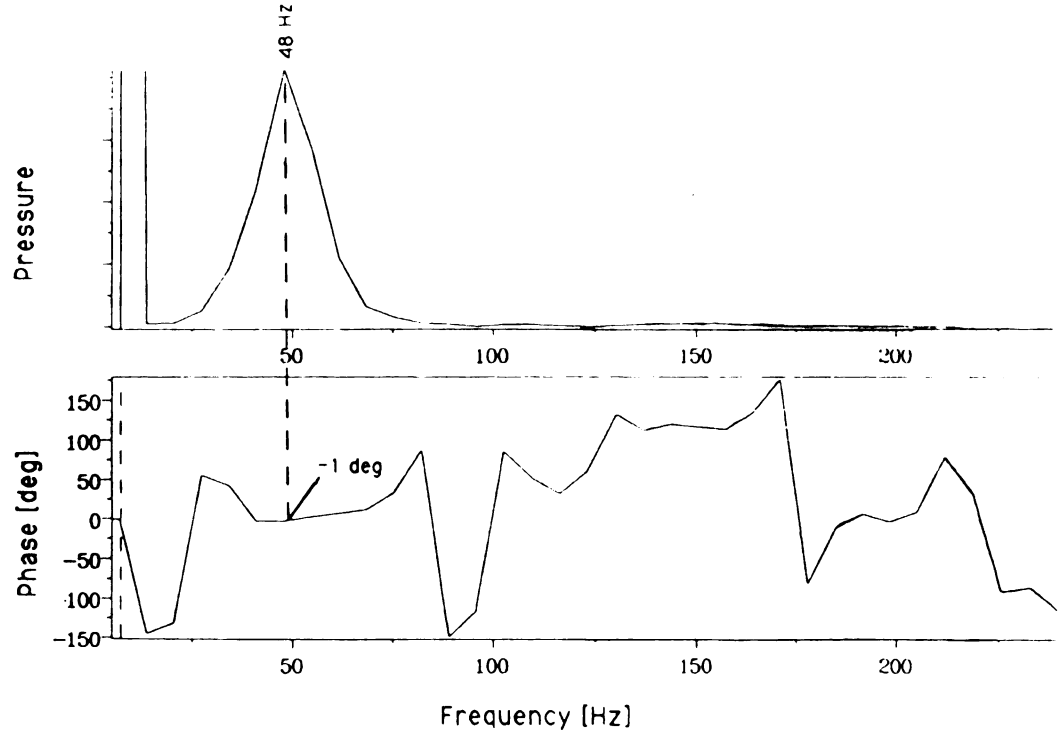

Fig. 4.27. Pressure & phase spectra for first segment of event C, N_{red}=14,000 rpm

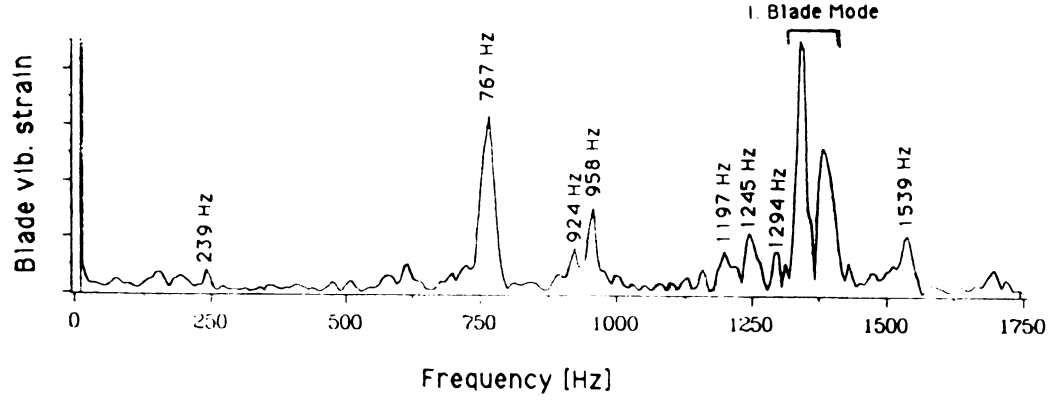

Fig. 4.28. Blade vibration spectra for first segment of event C, N_{red}=14,000 rpm

be lower than expected or higher than expected. However, this investigation reveals that measured phase angles do not follow these consistent patterns. Therefore, it appears that the deviation between recorded and expected values is not the result of error in determining $\Delta\phi_g$. The fact that examination of very slightly different sections of a signal produces significantly different pressure and phase angle spectra hints that the discrepancy between measured and expected values lies in the details of the FFT analysis.

Note also that despite the fact that phase angle at the pressure spectrum peak corresponded most closely with m=+1, the actual mode of rotating stall was m=+4. This illustrates the imprecise nature of phase analysis for determining the character of rotating stalls encountered and the desirability of using several circumferentially-spaced transducers when using this method of stall detection and characterization.

In summary, for event C, agreement between the two analyses shows that the first rotating stall in event C contained three cells and rotated in the opposite sense as the rotor with a speed ω_{st}/Ω=0.067. The second stall had four stall cells, and rotated in the same direction as the rotor rotation with speed ω_{st}/Ω=0.022.

4.3.4 Event D

So far, the pressure-time trace obtained at ϕ_g=0 degrees and ϕ_g=125 degrees have looked substantially the same. However, with event D this changes. Figure 4.29 shows the pressure signals from the two transducers at x/s = 0.74 for event D. Here, the signal from ϕ_g=0 degrees appears to be dominated by low frequency (about 50 Hz) pressure fluctuations of approximately equal amplitude throughout the entire event. In contrast, the signal obtained from ϕ_g=125 degrees shows this low

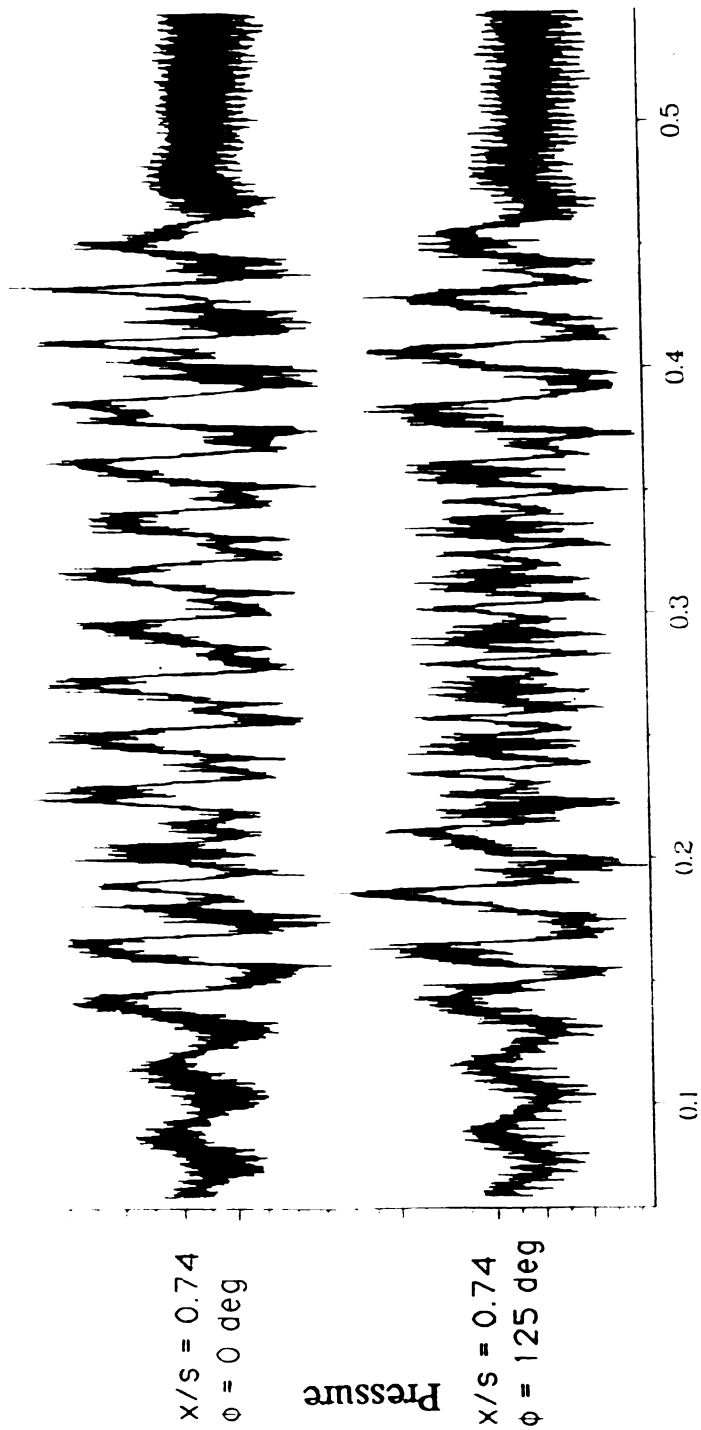

Fig. 4.29. Pressure-time signals for event D, N_{red}=14,000 rpm

frequency oscillation declining in amplitude, leveling off over the center section of the event, then increasing to its previous amplitude over the last of the event. Close inspection of this signal reveals that a clear 50 Hz signal appears to remain (with a lower amplitude), but each crest of this 50 Hz signal is separated by rapid oscillations which produce an unclear trace. This may indicate that we have pressure oscillations superimposed on one another. The ϕ_g=0 degree signal also shows these intermediate fluctuations; but, for this position they have very low amplitudes.

Signal analysis software provides a means for clarifying the dominant frequencies of oscillations embedded in event D. Figure 4.30 shows pressure spectra obtained through FFT analysis of each signal separately. Although the same three frequencies show up at each circumferential position, they differ in amplitude. For ϕ_g=0 degrees, the peak at 45 Hz clearly dominates, followed by a peak at 89 Hz and one at 134 Hz. For ϕ_g=125 degrees, the peak at 134 Hz dominates, followed by the peak at 89 Hz and two peaks in the 40-50 Hz range. This unusual result does not resemble those obtained for the other rotating stall events investigated here. For all other events, the single-signal FFTs showed nearly identical pressure spectra for both signals.

Figure 4.31 shows the pressure and phase angle spectra diagrams for the section of event D between t=0.1 and t=0.5. Figure 4.32 shows the same information, but for a slightly smaller section of event D (0.15 s.$\leq$t$\leq$0.47 s.). Although the sections analyzed differed only slightly in size, their corresponding pressure/phase angle spectra diagrams differ significantly. Figure 4.31 shows greater resolution than Figure 4.32. The blade spectra analyzed comes from the same section represented by Figure 4.32.

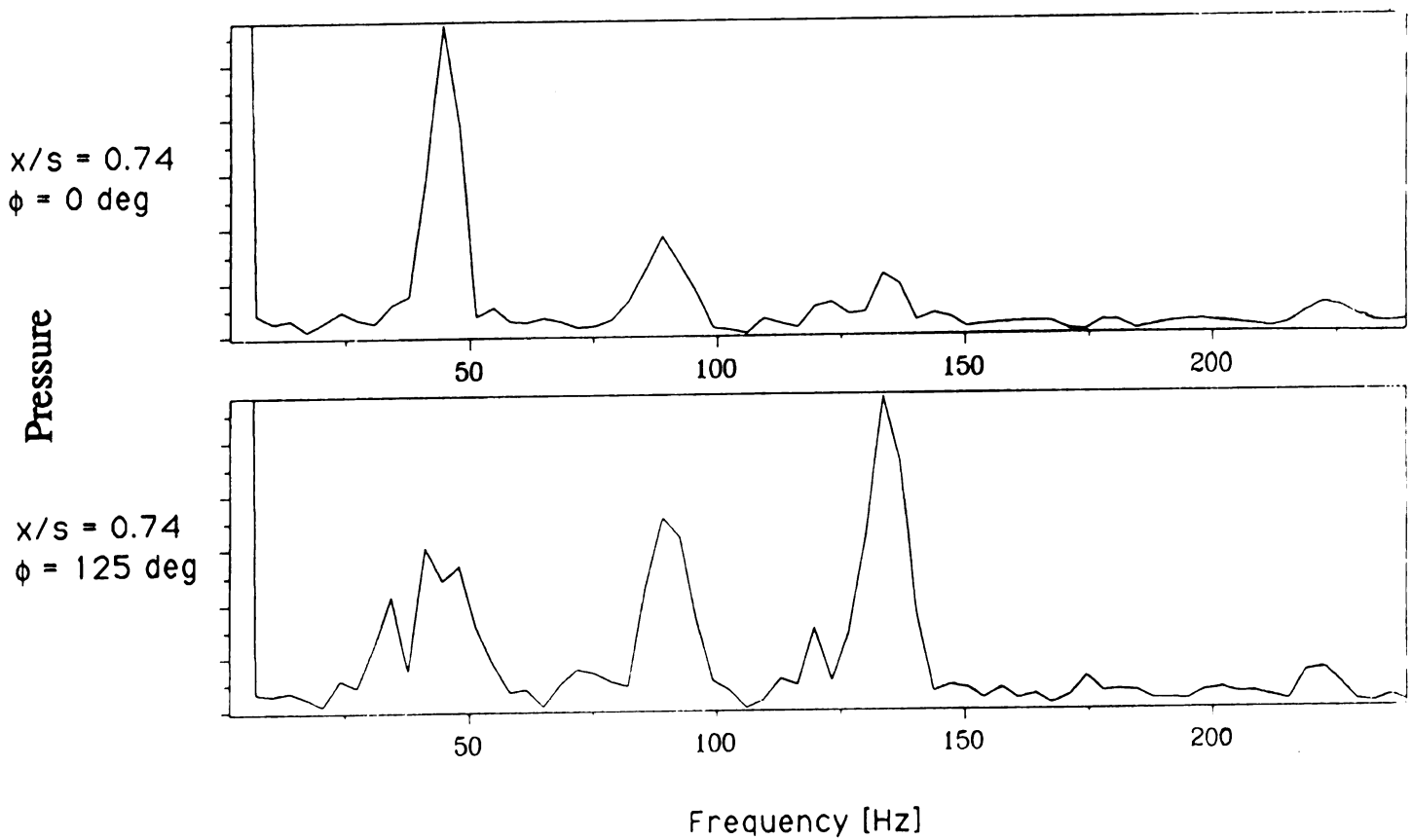

Fig. 4.30. Pressure spectra for individual signals (single-signal FFTs) for event D, N_{red}=14,000 rpm

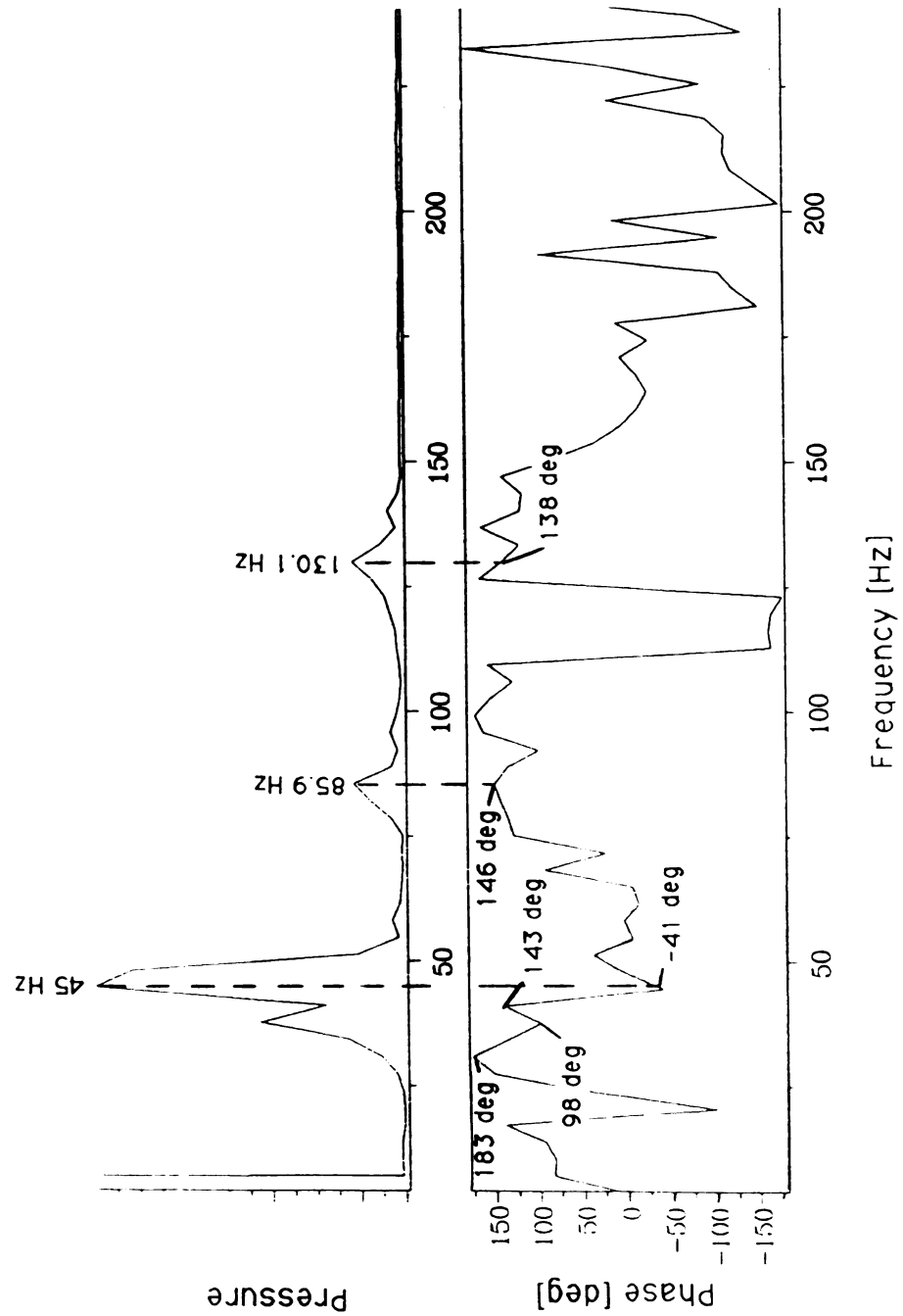

Fig. 4.31. Pressure & phase spectra for event D (Cut #1), N_{red}=14,000 rpm

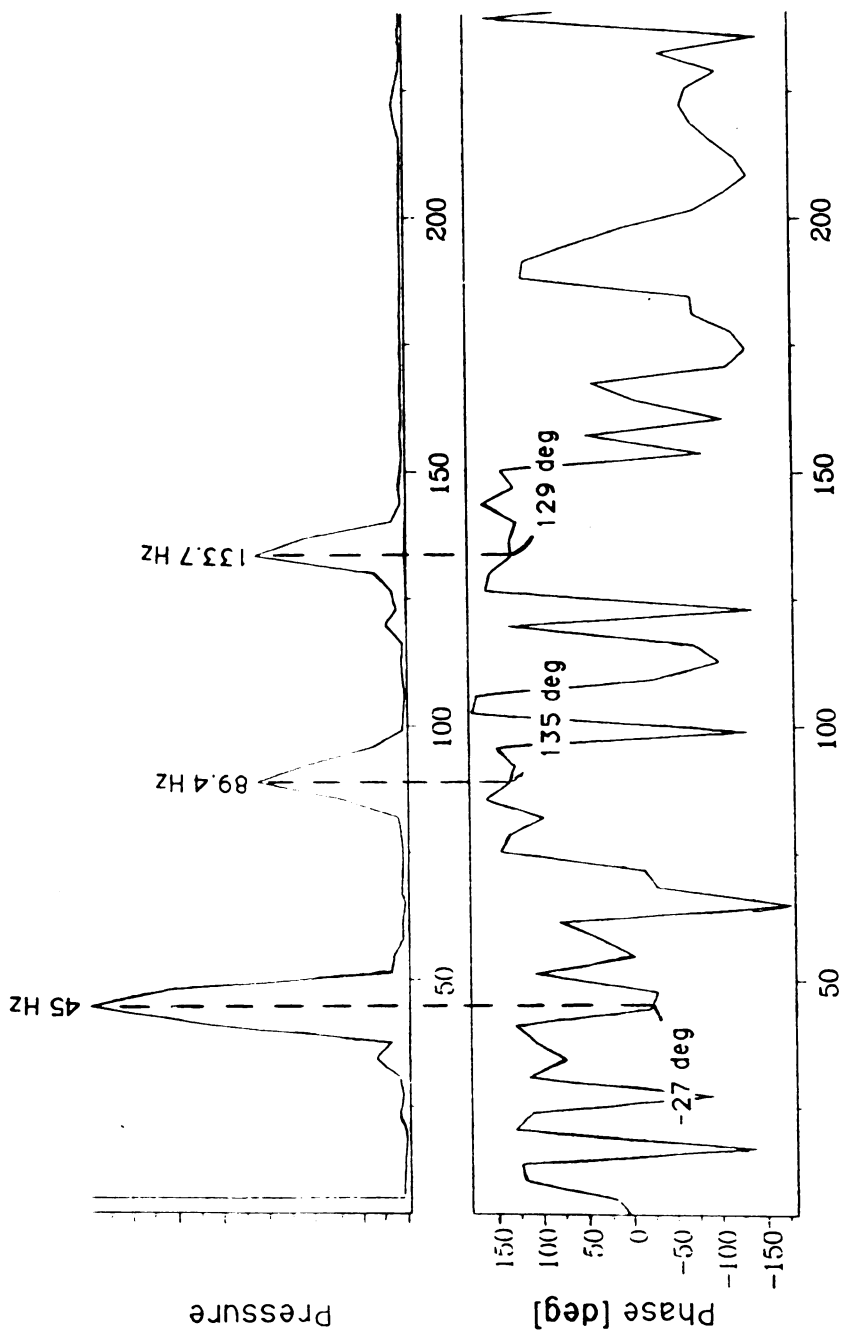

Fig. 4.32. Pressure & phase spectra for event D (Cut #2), N_{red}=14,000 rpm

According to Figure 4.32, the phase angles corresponding to the 45 Hz peak vary dramatically over the entire base of the peak. However, it appears that the core of the peak has phase angles in the 0 to -35 degree range. A phase analysis reveals that this corresponds to rotating stall with m=-3. This agrees with the results found for the previous events at N_{red}=14,000 rpm; however, this result should be checked with that obtained from a blade vibration analysis.

Another possibility exists for the mode of rotating stall responsible for the 45 Hz peak. A phase angle of 95 degrees, which corresponds to m=-5 takes place at approximately 42 Hz. However, this does not have the relatively flat phase angle distribution typically found for events formerly analyzed. For this reason, we suspect that the m=-3 hypothesis seems stronger than the m=-5 hypothesis.

Figure 4.32 also shows prominent peaks at 89 Hz and 134 Hz. Analyzing the phase angles of the 89 Hz and 134 Hz peaks shows that these peaks are caused by a different event than causes the 45 Hz peak. The pressure spectra for event D looks very similar to that found for event B, where simultaneous stalls may have occurred. This observation also proves useful for explaining the data obtained for event D.

Figure 4.33 shows the peak amplitude blade vibration spectra for event D. It appears that similar stall patterns produce the unusual blade vibration spectra for both event B and event D. The blade vibration spectra for both events resemble one another. This suggests that for event D, as in event B, simultaneously operating modes of rotating stall occurred.

Equation (3-12) provides a means for explaining the peaks for both events. Supposing two simultaneous rotating stalls with f_p=45 Hz and 134 Hz, almost every prominent peak can be explained as resulting from shaft

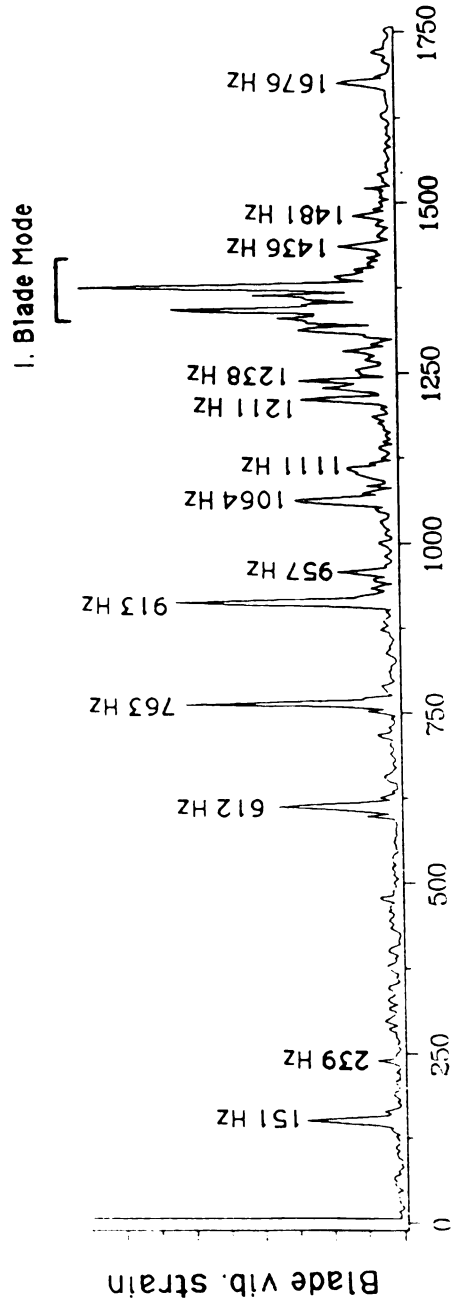

Fig. 4.33. Blade vibration spectra for event D, N_{red}=14,000 rpm

frequency (e.g., 957=4·f_s, 1436=6·f_s,1676=7·f_s,), aliasing (viz., 151 Hz), or from asymmetric rotating stalls. In this case, the m=-3 stall produces the 763, 913, 1111, and 1238 Hz peaks and the m=-2 stall produces the 612 and 1064 Hz peaks. No explanation can be given for the 1211 Hz peak. So, it appears that the blade vibration analysis bears out our suspicion that event D contains a m=-3 rotating stall propagating with ω_{st}/Ω=0.063 and a weaker m=-2 rotating stall with ω_{st}/Ω=0.280.

A further glance at the blade vibration spectra, however, reveals remarkable regularity between the 612, 763, 913, 1064, and 1211 Hz peaks. Each of these lies approximately 151 Hz from its neighbor in the series (viz., 151≈763-612≈913-763≈1064-913). This remarkable pattern hints that at least some of the peaks are related to the 151 Hz peak. If the 151 Hz peak originates from the physical system, then the peaks listed above could result from the non-linear nature of the physical system, as described earlier. However, the 151 Hz peak is thought to arise from aliasing. Therefore, precise determination of the source of the multiple peaks cannot be made at this time.

Hypothesizing concurrent stalls also helps explain the different character of the pressure signals obtained (see Figure 4.35) for two circumferential positions. At ϕ_g = 125 degrees, the circumferential pressure asymmetry, perhaps produced by the presence of the collector exit appears to have dampened the low frequency oscillations which dominate the pressure signal at ϕ_g = 0 degrees. It also serves to amplify pressure oscillations which occurred at other frequencies. The net effect is to reveal more clearly higher frequency pressure fluctuations which appear to be somewhat masked in the presence of the clearly dominant 45 Hz oscillations at ϕ_g=0 degrees.

4.3.5 Other events

Brief, mild pressure oscillations occurred between each of the events at N_{red}=14,000 rpm described above. In each case, a pressure/phase angle analysis revealed these mild events to result from rotating stalls with m=-3. Also, as noted earlier, one brief instance of m=+1 rotating stall lasting for 0.6 seconds constituted the first event in a surge train recorded at N_{red}=10,000 rpm. This surge event is included in Table 4.6, which displays the results for rotating stalls encountered in this investigation.

Table 4.6 compares the results of this investigation with those presented in Seidel, et al. (1991b) for the same machine with the same diffuser vane geometry (cambered vane), but operated at different diffuser vane angle and with a different impeller. Generally, the rotating stalls found in this investigation occurred with higher speeds than those found with other configurations, and in greater variety. It appears that the rotor exit angle plays a more prominent role in determining the character of the rotating stalls encountered than does either the rotor blade number or the diffuser vane angle settings. The most prominent mode of rotating stall found in this investigation had m=-3. This also occurred in the 90 degree impeller investigated by Seidel, et al., even though the rotor they used had 28 vanes and the diffuser vanes were set at a different angle to that used here. Changing to a backswept impeller produced entirely different results than that obtained for the 90 degree impellers, even for a blade number and diffuser vane angle setting identical to those used in this investigation.

TABLE 4.6. Rotating Stalls found for different impeller and diffuser configurations, λ =1.15 for all

(a)=event A, (b)=event B, (c)=event C, (d)=event D

	β_3= 17 deg β_2= 90 deg Z = 28 (Seidel, et. al., 1991b)			β_3= 27 deg β_2= 60 deg Z = 20 (Seidel, et. al., 1991b)			β_3= 27 deg β_2= 90 deg Z = 20		
Nred [rpm]	m [-]	fp [Hz]	$\frac{\omega_{st}}{\Omega}$ [-]	m [-]	fp [Hz]	$\frac{\omega_{st}}{\Omega}$ [-]	m [-]	fp [Hz]	$\frac{\omega_{st}}{\Omega}$ [-]
10,000	Not recorded			Not recorded			+1	56	0.33
12,000	-3	40	0.067	+6	56	0.050	No rot. stall		
14,000	-3	18	0.026	+5	16	0.014	-3	34 (a)	0.047
				+6	85	0.068		45 (d)	0.063
								48 (b)	0.067
								48 (c)	0.067
							+4	22 (c)	0.022
							+5	117 (a)	0.098

4.4 Blade-to-Blade Pressure Difference Characteristics for Stable Operation

Figures 4.34 through 4.37 show blade-to-blade static pressure difference variation with meridional position and flowrate. Here, blade-to-blade pressure coefficient (ψ_b) is plotted against meridional position (x/s) and flow coefficient (ϕ). Each figure shows two views of one contour corresponding to a single operating speed. These graphs provide a convenient way of displaying blade-to-blade pressure oscillations so as to (1) understand how these vary along the meridional extent of the shroud line over the entire operating range and (2) provide a convenient way to

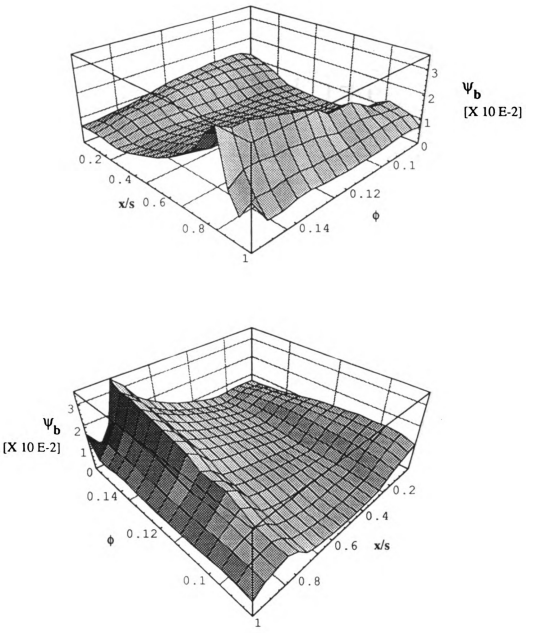

Fig. 4.34. Blade-to-blade pressure variation with flowrate and meridional position (Nred=10,000 rpm, 90 deg. impeller).

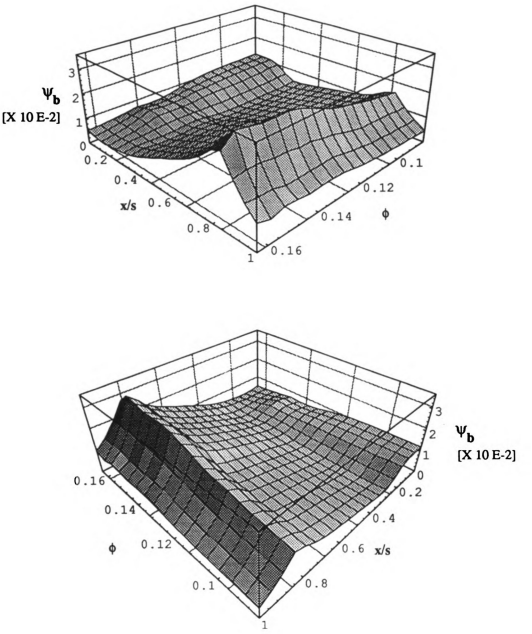

Fig. 4.35. Blade-to-blade pressure variation with flowrate and meridional position (Nred=12,000 rpm, 90 deg. impeller).

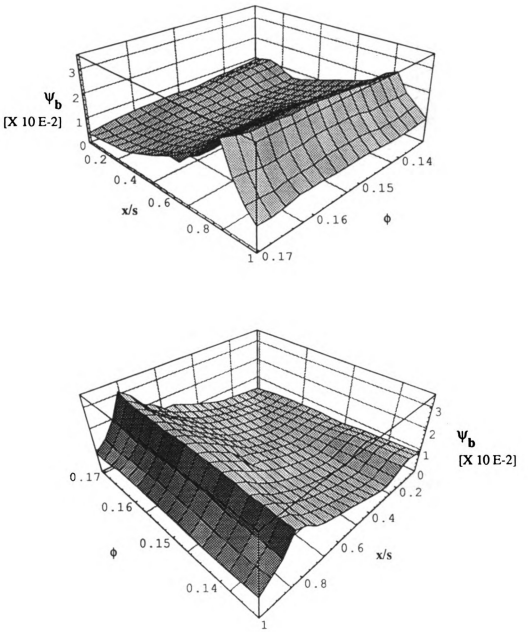

Fig. 4.36. Blade-to-blade pressure variation with flowrate and meridional position (Nred=14,000 rpm, 90 deg. impeller).

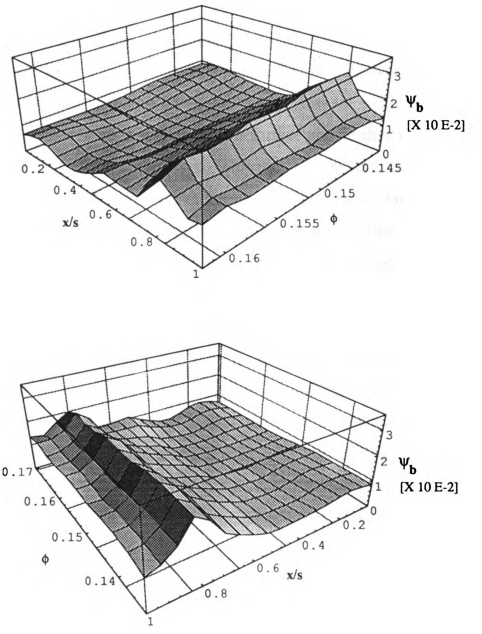

Fig. 4.37. Blade-to-blade pressure variation with flowrate and meridional position (Nred=16,500 rpm, 90 deg. impeller).

check whether or not reductions in blade-to-blade pressure difference provide a good way of following the extent of reverse flow from the impeller exit toward the inlet.

4.4.1 Pressure variation with mass flowrate

If reverse flow occurs, its effects would first be felt over the last portion of the impeller passage. Then, as reverse flow intensifies as flowrate drops, its influence should be felt further and further into the impeller channels. For operation at 10,000 rpm, 12,000 rpm, and 14,000 rpm, data presented in Figures 4.34 through 4.37 show that blade-to-blade pressure rise changes little at the impeller exit. For this section of the impeller, only data for N_{red}=12,000 show a significant decline in blade pressure coefficient as flow is reduced. For the site of maximum energy transfer (near x/s=0.8), however, blade-to-blade pressure rise does drop as flowrate is reduced. Comparison of data for different operating speeds shows that this decline in blade-to-blade pressure differences decrease as speed increases until, at N_{red}=16,500 rpm, the blade-to-blade pressure difference amplitudes actually increase with reduction in flowrate. Figure 4.38 shows these trends by means of simple straight-line curve fits of the data for x/s=0.84. Thus, it appears that blade-to-blade pressure difference data follow the trend cited by Chen, et al. (1988) for low speed operation, but not when operating speed exceeds a critical value.

Trends for the initial section of the impeller differ from those of the trailing section. Here, for N_{red}=10,000, 12,000, and 14,000 rpm, blade-to-blade pressure difference generally increases as flow drops. For these speeds, contours for low speed operation show more pronounced increases in the blade pressure coefficient with decreases in flowrate than do contours for higher speeds. The contour for N_{red}=16,500 rpm differs

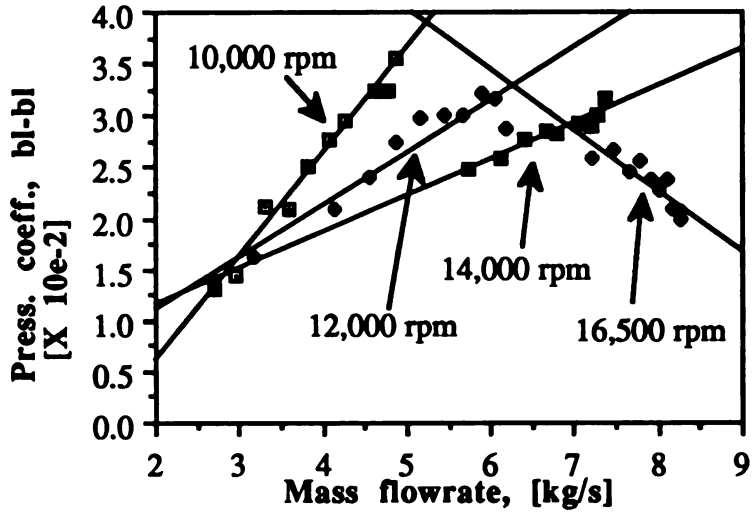

Fig. 4.38. General variation in blade-to-blade pressure difference with mass flowrate over last section of impeller

from the others. Moving from maximum flowrate toward minimum flowrate, blade pressure coefficient drops, reaching a minimum value near the midpoint of the flow range. As flowrate drops further, the blade pressure coefficient climbs to values slightly higher than those encountered at maximum flowrate.

Generally, it appears that at the shroud line for N_{red}=10,000, 12,000, and 14,000 rpm, as flowrate drops, an increasingly larger portion of energy transfer occurs in the initial impeller section relative to that occurring in downstream sections. This is indicated (though inconclusively) by the fact that further downstream, the blade pressure coefficient declines with decreases in mass flowrate at the same time that blade pressure coefficients in the inducer section increases. This does not appear to be the case for operation at 16,500 rpm. Here, blade pressure coefficient values increase in both the inducer section and further downstream as flowrate drops. Even so, examination of trends for all speeds investigated reveals that for decreasing flowrates, the larger the blade pressure coefficient drop

at x/s=0.84, the larger the blade pressure coefficient rise in the inducer section.

4.4.2 Pressure variation with meridional location

Figures 4.34 through 4.37 show that the greatest blade-to-blade pressure differences occur in the impeller section containing splitter blades.

4.4.2.1 Before splitter blades (x/s<0.25)

Values of blade-to-blade pressure differences before the onset of splitter blades are generally much lower than those downstream. In the impeller section preceding the splitter blades, blade pressure coefficient usually achieves a maximum at x/s=0.06, then drops with increasing meridional position. The exception appears to be at N_{red}=14,000 rpm. Here, maximum values for blade pressure coefficient in the initial channel section occur at x/s=0.16 over a section of the flow range. For high flowrates, it appears that values of blade pressure coefficient upstream of splitter blades tend to remain flat or gently rise with increases in meridional position.

4.4.2.2 After splitter blades (0.25<x/s<1.0)

For every speed investigated, the pressure transducer located at x/s=0.84 sensed the highest blade-to-blade pressure differences. Between this point and the point at which splitter blades start (x/s=0.25), blade-to-blade pressure differences dropped smoothly and relatively gradually. Minimum blade-to-blade pressure oscillation amplitudes were measured by the probe at x/s=0.31 for all operating speeds over most of the flow range. This minimum probably results from fluid adapting to the presence of splitter blades where there were none before.

From the site of maximum ψ_b (x/s=0.84) to the impeller outlet, blade-to-blade pressure differences dropped rapidly. Over this range, the

fluid has to adjust to the boundary conditions just past the impeller exit, where no impeller blades reside and energy transfer ceases.

4.4.3 Pressure variation with impeller type

Analysis was also performed on data from earlier tests using an impeller with a 30 degree backsweep (β_2=60 degrees). Figure 4.39 shows how blade pressure coefficient varies with both flowrate and meridional position. As with earlier plots, Figure 4.39 presents two views of one contour. Comparison with Figure 4.35, which shows a plot for the same speed, but different impeller, shows that blade-to-blade pressure variation for the initial impeller section resembles that of the 90-degree impeller. In both cases, blade pressure coefficient increases as flowrate drops. Variation with increasing meridional position constitutes the principal difference for the inducer sections of the different impellers. The 90-degree impeller shows maxima occurring at x/s=0.06 for all flowrates. In contrast, the 60-degree impeller shows maxima occurring at x/s=0.15 over most of its flow range. However, this difference may be artificial due to the fact that for the 60-degree impeller, pressure measurements were taken just downstream of the impeller (x/s=-0.02), in contrast to the 90-degree impeller where measurements were taken just upstream (x/s=0.06) of the impeller entrance. This likely resulted in artificially depressed values of blade pressure coefficient for the 60-degree impeller's entrance region.

A further contrast between blade pressure coefficient for the two different impellers lies in the trend toward a minimum value. With the 90-degree impeller, minimum blade-to-blade pressure differences were recorded by the transducer at x/s=0.31, just past the beginning of the splitter blades (x/s=0.25). With the 60-degree impeller, however, minimum blade-to-blade pressure differences were recorded at x/s=0.40, just before

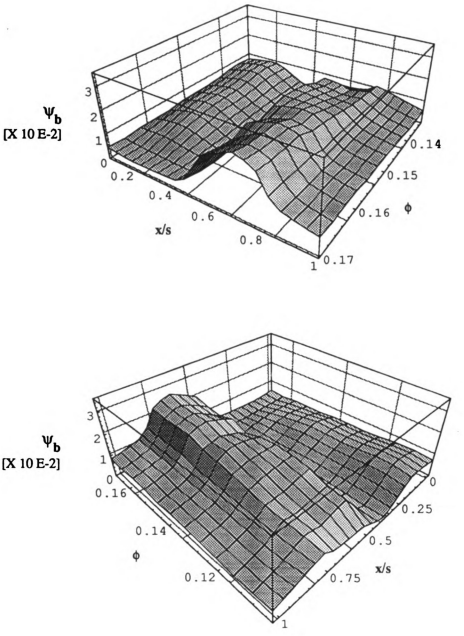

Fig. 4.39. Blade-to-blade pressure variation with flowrate and meridional position (Nred=12,000 rpm, 60 deg. impeller).

the beginning of the splitter blades (x/s=0.43). Again, this difference likely comes about as a result of the discrete placement of the pressure transducers along the shroud wall.

The largest difference between the maps of blade pressure coefficient for the two impellers investigated lies in how blade pressure coefficient grows downstream of the splitter blades' leading edges. For the 60-degree impeller, blade-to-blade pressure difference rises very quickly soon after the splitter blades are reached. In contrast, blade-to-blade pressure oscillation amplitudes rise much more gently in the 90- degree impeller. Furthermore, the 90-degree impeller showed maximum blade pressure coefficients at only one x/s position. For all flowrates and operating speeds, maximum blade-to-blade pressure rises were recorded at x/s=0.84. Maximum values for the 60-degree impeller, however, occur at varying meridional positions, depending on the flowrate. At high flowrates, a maximum occurs at x/s=0.7 and this maximum constitutes the only peak in blade pressure coefficient for these flowrates. However, as flowrate drops, blade pressure coefficient values tend to flatten out. Between x/s=0.55 and x/s=0.8, blade-to-blade pressure oscillation amplitudes drop significantly for the lowest flowrate. This could indicate the presence of reverse flow; but, this cannot be established without further testing.

CHAPTER 5--CONCLUSIONS & RECOMMENDATIONS

5.1 Conclusions

The preceding analysis suggest the following conclusions:

This investigation succeeded in extending results found in Seidel, et al. (1991b). A single flowrate at N_{red}=14,000 rpm contained several instances of intermittent unsteadiness, each enduring for approximately 100 rotor rotations before dying out. Two of these events contained identifiable modes of rotating stall. Two others contained one identifiable mode of rotating stall together with a possible mode of distinct, but weak rotating stall. All intermittent unsteadiness at 14,000 rpm contained m=-3 rotating stall events with frequency and propagational speeds corresponding to m=-3 stall modes found by Seidel (1991b) for the same machine operated with a different diffuser blade configuration and a 28-bladed radial outlet rotor.

Surge events investigated showed the same trends reported in Jin, et. al. (1992a). Surge was detected at N_{red}=10,000 rpm and N_{red}=12,000 rpm. Those events most resembling surge in other investigations contained two sections of gross unsteadiness, separated by a section of apparent, low amplitude unsteadiness. The two gross events were identified as products of m=+1 rotating stalls. The section separating these did not appear to contain identifiable modes of rotating stall.

Insights into the accuracy and utility of various analytical devices and procedures were obtained. It appears that bench top FFT analysis gives slightly more accurate readings than the software package used in this

investigation. However, software allowed for greater flexibility for analyzing the details of very brief events difficult to capture using the FFT analyzer. Generally, blade vibration analysis yields more accurate results than pressure/phase angle analysis. However, investigators must be careful to filter out frequency bands which may show up as aliased signals.

This investigation shows that blade-to-blade pressure difference readings did not provide a reliable means for tracking reverse flow intensity in impeller channels. No clear pattern of diminishing blade-to-blade pressure difference amplitudes were found near the rotor exit, where they would first be expected to occur. Near the site of maximum energy transfer (x/s=0.84), declines in blade-to-blade pressure difference are most severe at N_{red}=10,000 rpm. As rotor speed is increased, these declines diminish. Data showed that for N_{red}=16,500 rpm, these amplitudes actually increase with decreases in flowrate.

5.2 Directions for Future Work

This investigation uncovered highly unusual peaks in the blade spectra. Attempts to explain the origin of many of these peaks have provided inconclusive results. Future work could concentrate on finding the source of these peaks. The fact that many of these peaks are separated from other major peaks by 151 to 157 Hz should provide one clue for solving this mystery.

Further work could also establish expected pressure patterns produced by simultaneous pressure unsteadiness and how this unsteadiness would excite blade vibration.

Blade-to-blade pressure difference amplitudes are known to vary during rotating stall (Chen, et. al., 1993). Further analysis of pressure signals

produced under conditions of rotating stall could quantify these amplitudes over different sections of stall periods.

APPENDICES

APPENDIX A--EQUIPMENT

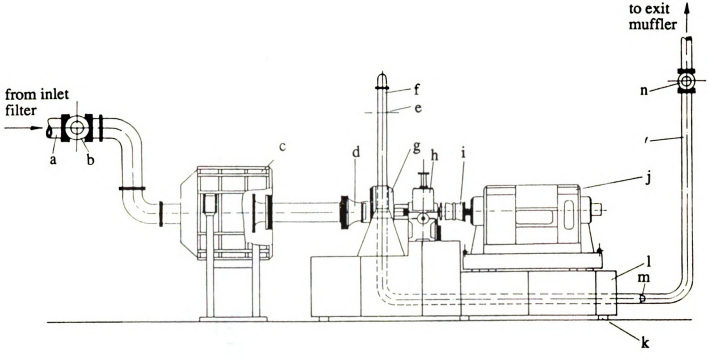

a. Suction pipe
b. Gate valve
c. Plenum
d. Inlet nozzle
e. Measurement plane, stage exit
f. Pressure pipe
g. Centrifugal compressor
h. Gearbox
i. Coupling
j. DC motor
k. Vibration pads
l. Steel foundation
m. flowmeter
n. Throttle valve

Fig. A.1. Schematic representation of compressor test stand

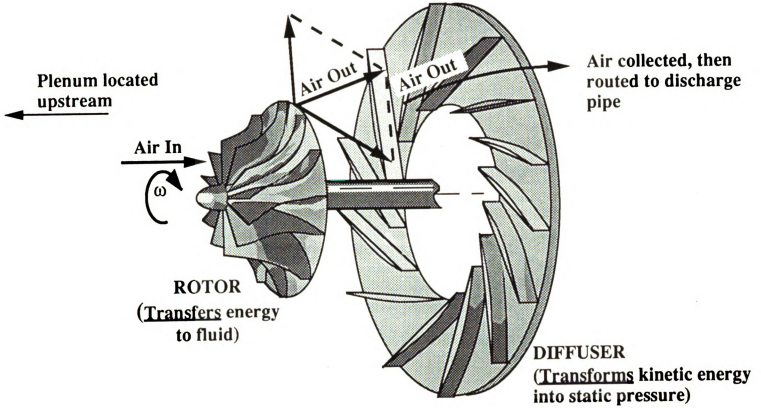

Fig. A.2. Key Components of centrifugal compressors

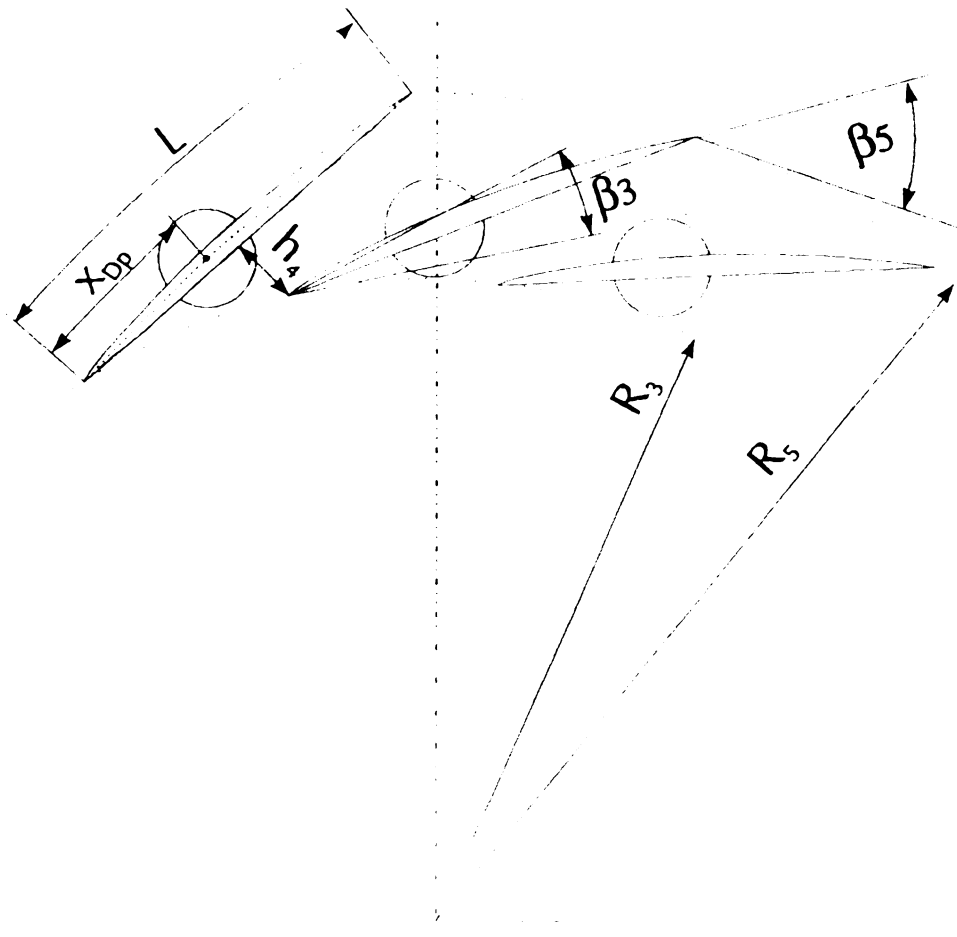

Fig. A.3. Basic diffuser configuration parameters

MINIATUR-DRUCKAUFNEHMER
(Miniature Pressure Transducer)

XCQ-080

- Durchmesser 2,0 mm; Länge 6,35 mm
- sehr hohe Eigenfrequenzen
- für statische und dynamische Messungen
- sehr gutes Temperaturverhalten

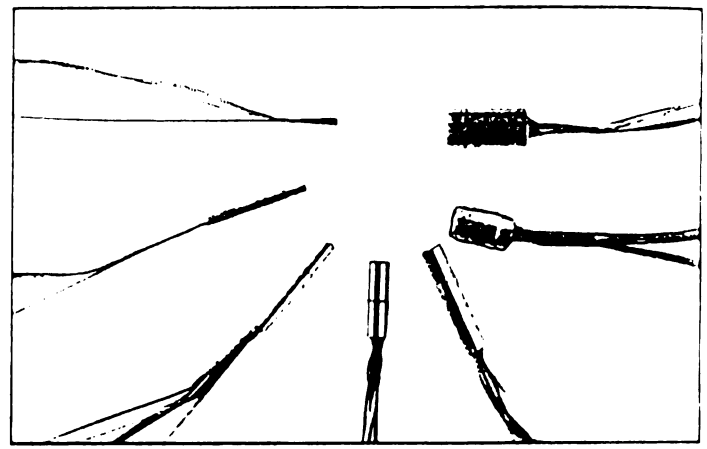

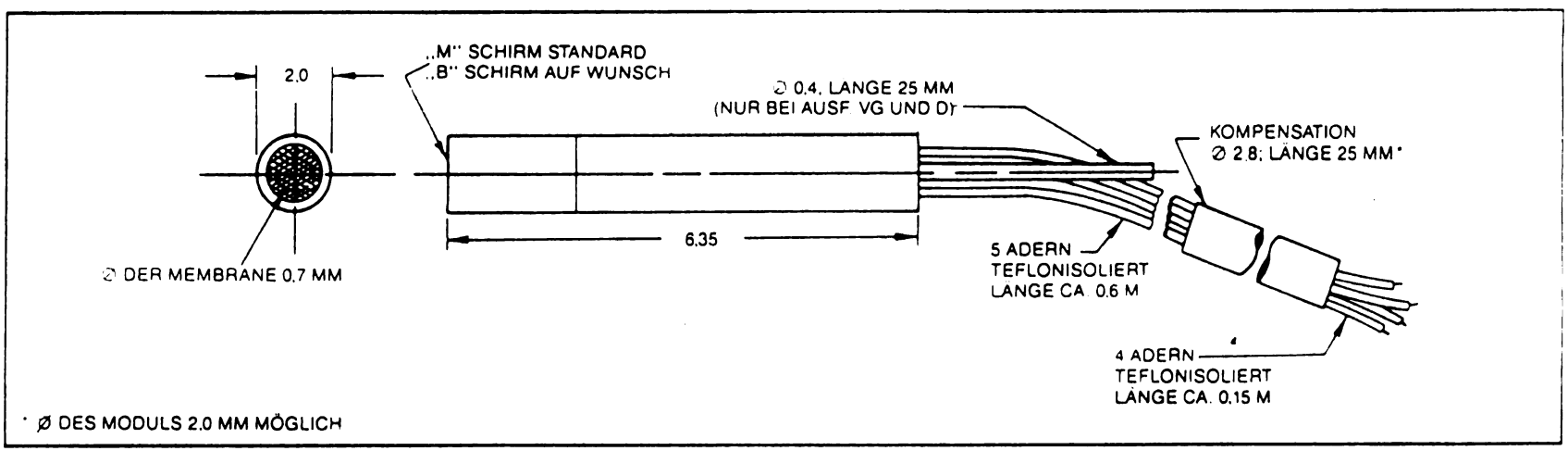

Fig. A.4. Schematic of Kulite XCQ-080 dynamic pressure transducer

APPENDIX B--DERIVATION OF EQUATIONS FOR ANALYSIS

APPENDIX B1--ANALYSIS OF ROTATING STALL USING BLADE VIBRATION CHARACTERISTICS

Rotating stalls are characterized in part by the number of cells of which they are composed. The following derives a relation between measured pressure signals, blade vibration spectra peaks, and the number of cells in rotating stall.

B.1 Rotational Speeds.

For centrifugal compressors, we must relate motions in two frames of reference: (1) the absolute frame, which corresponds to coordinate axes fixed to the earth, and (2) the relative frame, which corresponds to coordinate axes fixed to a rotor rotating with respect to the absolute frame. Figure B.1 shows these two reference frames. From general kinematics, we can write

$$\omega_{abs} = \omega_{rel}+\omega_{abs/rel}, \text{ or}$$

$$\omega_{rel} = \omega_{abs}+\omega_{rel/abs}, \text{ where} \qquad \text{(B-1)}$$

ω_{abs} is rotational velocity in the absolute frame,
ω_{rel} is rotational velocity in the relative frame,
$\omega_{abs/rel}$ is rotational velocity of the absolute frame with respect to the relative frame, and
$\omega_{rel/abs}$ is rotational velocity of the relative frame with respect to the absolute frame.

Now consider the rotation of the rotating stall cells. Following (B-1), we can write

$$\omega'_{rel} = \omega'_{abs}+\omega_{rel/abs}, \qquad \text{(B-2)}$$

where the prime designation is used to signify that we are talking of rotating speed of stall cells.

Next, we note that in practice an impeller resides on and rotates around a fixed axis of rotation (fixed in both reference frames). In this case, $\omega_{rel/abs} = \omega_{rot} = \omega_{shaft}$. (B-3)

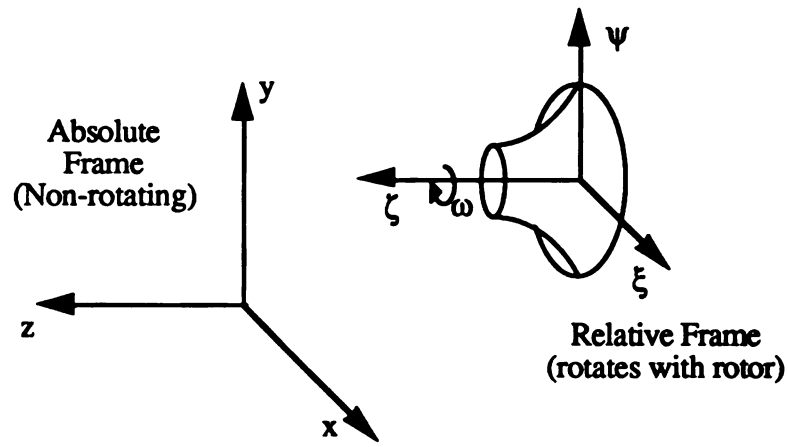

Fig. B.1. Absolute and relative reference frames.

Noting from figure B.1 that the z and ζ axes are always parallel and employing equation (B-3) allows us to rewrite equation (B-2) in scalar form

$$\omega'_{rel} = \varepsilon \cdot \omega'_{abs} + \omega_{shaft} \text{ , where} \qquad \text{(B-4)}$$

$\varepsilon = +1$, when ω'_{abs} is in the same direction as ω_{shaft} and
$\varepsilon = -1$, when ω'_{abs} is in the opposite direction as ω_{shaft}.

B.2 Frequencies.

Frequencies are related to rotational speeds by the relation $f = 2\pi\omega$. Substituting into equation(B-4) allows us to write:

$$f_{r.s./rel} = \varepsilon \cdot f_{r.s./abs} - f_{shaft}. \qquad \text{(B-5)}$$

Note that since $f_{r.s./rel}$ is a frequency, its value will always be positive; so, equation (B-5) should be rewritten

$$f_{\text{r.s./rel}} = | \varepsilon \cdot f_{\text{r.s./abs}} - f_{\text{shaft}} |. \qquad \text{(B-6)}$$

Next, we need to relate measured pressure and blade vibration frequencies with those of rotating stall. Note that the blade vibration arises from the frequency of rotation of the rotating stall in the relative frame. We must also account for the number of stall cells. We write,

$$f_{\text{blade}} = m \cdot f_{\text{r.s./rel}} \text{ , where m = number of stall cells.} \qquad \text{(B-7)}$$

Also, we should note that $f_{\text{press/abs}} = m \cdot f_{\text{r.s./abs}}$. (B-8)

Substituting into (B-6) and manipulating, we find that

$$f_{\text{blade}} = | \varepsilon \cdot f_{\text{press/abs}} - m f_{\text{shaft}} |. \qquad \text{(B-9)}$$

Here, we are confronted with three cases:

Case 1: $(\varepsilon \cdot f_{\text{press/abs}} - m f_{\text{shaft}}) < 0$;
Case 2: $(\varepsilon \cdot f_{\text{press/abs}} - m f_{\text{shaft}}) = 0$; and
Case 3: $(\varepsilon \cdot f_{\text{press/abs}} - m f_{\text{shaft}}) > 0$.

Since $m \geq 1$ and since $f_{\text{shaft}} > f_{\text{press/abs}}$, then only case 1 is of interest. Case 1 implies that

$$f_{\text{blade}} = -(\varepsilon \cdot f_{\text{press/abs}} - m f_{\text{shaft}}), \qquad \text{(B-10)}$$

and this constitutes our final expression relating measured frequencies and rotating stall characteristics.

APPENDIX B2--ANALYSIS OF ROTATING STALL USING PRESSURE AND PHASE SPECTRA DATA

Instances of rotating stall are characterized in part by their lobe number. In addition to the method derived in appendix B1 for determining lobe number, we can also find this value by utilizing the pressure signal phase shifts in circumferentially spaced pressure transducers. The following, drawn from Kämmer (1984), derives the relation expressing lobe number in terms of pressure signal phase shift.

The lobe number of rotating pressure patterns such as rotating stall can be measured using two circumferentially spaced pressure transducers. Pressure signals for rotating pressure patterns are functions of both space and time and act essentially as pressure waves propagating in the circumferential position. The pressure signal will assume a sinusoidal character. For a signal of maximum amplitude, P, the pressure can be written

$$p(t,\Delta\phi_g) = P \cdot \sin(\omega_{st} t - m\Delta\phi_g) \qquad \text{(B-11)}$$

Here, ω_{st} is the rotational speed of the pressure pattern,
$\Delta\phi_g$ is the geometric angle separating the two transducers, and
m is the number of cells of the pressure pattern.

When the pressure pattern rotates in the same direction as the rotor, then m assumes a positive value. For pattern rotation opposite that of the rotor, m is negative.

Pressure signals from two pressure transducers located at circumferential position ϕ_{g1} and ϕ_{g2} sampling the same rotating pressure pattern can be related as follows:

$$P \cdot \sin(\omega_{st} t - m\Delta\phi_{g1}) = P \cdot \sin[\omega_{st}(t + \Delta t) - m\Delta\phi_{g2}] \quad \text{(B-12)}$$

where at location ϕ_{g2}, the maximum pressure P arrives slightly later than at location ϕ_{g1}. This is time lag is accounted for by replacing t with t+Δt. This allows us to write m in terms of time, rotational velocity of the pressure pattern, and circumferential positions of the transducers, as follows:

$$m = \frac{(\omega_{st}\Delta t \pm k \cdot 2\pi)}{(\phi_{g2} - \phi_{g1})}, \quad \text{(B-13)}$$

where k is any integer desired. Figure B.1 shows two signals produced by two circumferentially spaced transducers.

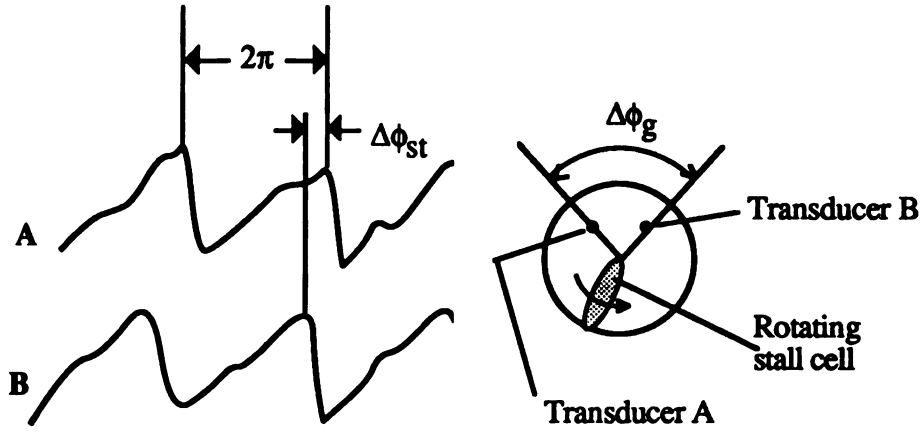

Fig. B.2. Signals produced by two circumferentially-spaced transducers

Next, we relate phase angle between pressure signals with the rotational speed of the rotating pressure pattern

$$\omega_{st}\Delta t = \frac{2\pi \cdot \Delta t}{T_{st}} = \Delta\phi_{st} \qquad \text{(B-14)}$$

Here T_{st} is the average period of the measured pressure signals and $\Delta\phi_{st}$ is the phase angle difference between the pressure signals.

Substituting (B-4) into (B-3), we find a useful relation for the lobe number:

$$m = \frac{(\Delta\phi_{st} \pm k \cdot 2\pi)}{\Delta\phi_g} \qquad \text{(B-15)}$$

Here, $\Delta\phi_g=(\phi_{g2}-\phi_{g1})$ and is the geometric angle separating the two transducers. Note that the value of $\Delta\phi_{st}$ can be negative. For example, for $\Delta\phi_{st}$=15 degrees and $\Delta\phi_g$=125 degrees, we get: m = (-0.26-2π)/(2.18) = -3.

A graphical method provides an easy way to determine lobe number. Using equation (B-5) and plotting lines for m=-1, +1, -2, +2, -3, ..., -5, +5, we produce the diagram shown as figure B.2. To determine the lobe number, a user simply plots the point corresponding to a given transducer separation angle and a measured phase angle. The user can then read lobe numbers from the chart by noting by which m-lines cross ϕ_g line in the area of the point. As an example, figure B.2 shows a reading for $\Delta\phi_{st}$ = -100 degrees and $\Delta\phi_g$ = 125 degrees, giving m=+5. To avoid ambiguous readings, at least three circumferentially-spaced transducers should be used when characterizing rotating stalls using this method.

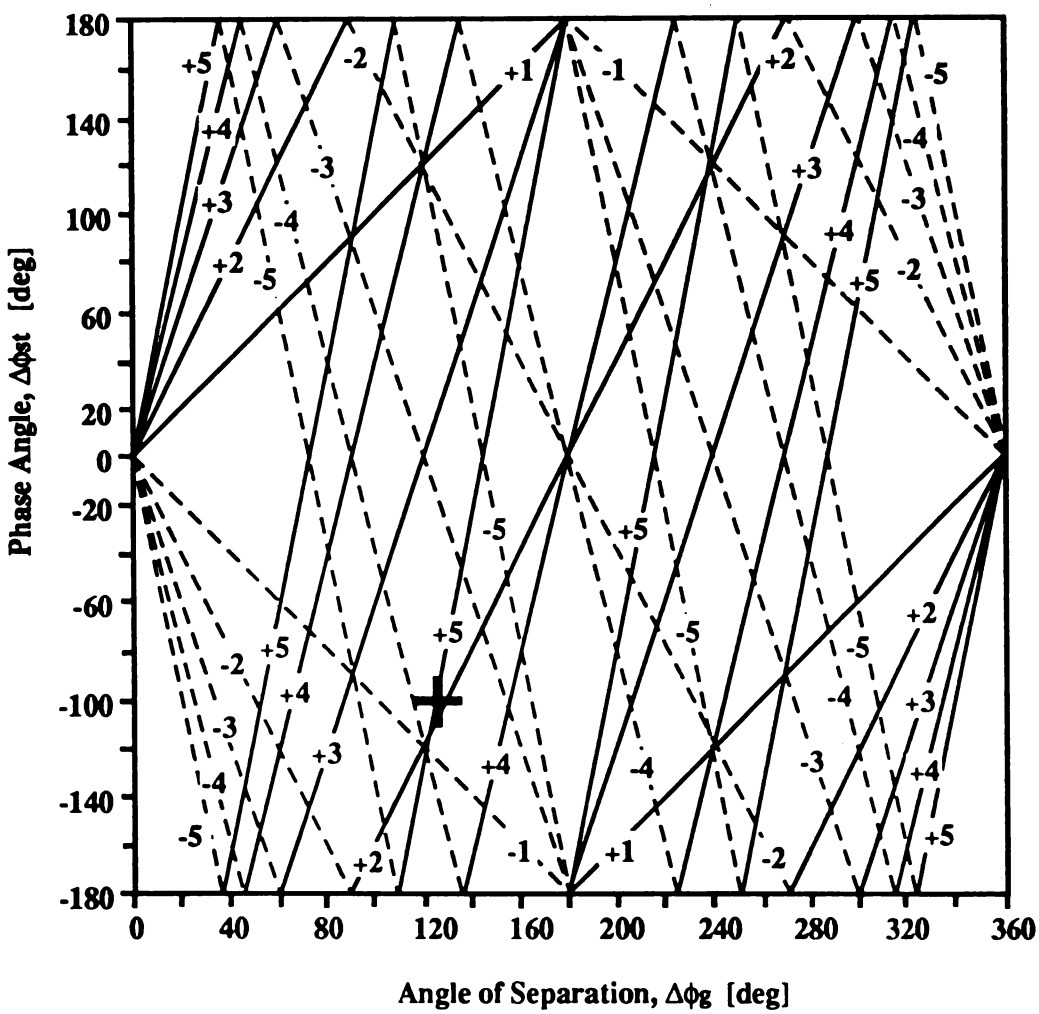

Figure B.3. Graphical method for determining lobe number.
e.g. ($\Delta\phi_{st}$=-100 deg. & $\Delta\phi_g$=125 deg) => m=+5

APPENDIX C--EXPERIMENTAL DATA

TABLE C.1. AMPLITUDE OF PRESSURE SIGNAL AT BLADE PASSING FREQUENCY--RAW DATA									Tape No.	102	
									Test Date	11.05.93	
									Analysis Date	27.07.93	
		Red.	Pressure Readings [mV]								
Meas. Point	Red. Speed	Mass Flowrate	Probe Position								
	[rpm]	[kg/s]	x/s=0.06	x/s=0.16	x/s=0.31	x/s=0.58	x/s=0.74*	x/s=0.74**	x/s=0.84	x/s=0.94	x/s=1.0
1	10,000	4.89	29.00	15.50	14.60	57.10	47.90	49.00	37.60	10.70	18.20
2	10,000	4.78	29.80	17.00	13.60	53.00	43.70	45.20	34.20	16.70	9.73
3	10,000	4.61	32.70	21.10	14.80	55.70	44.30	46.00	34.20	15.60	8.78
4	10,000	4.28	19.50	23.80	14.90	52.10	40.30	40.70	31.10	16.00	9.61
5	10,000	4.07	23.00	51.20	27.90	50.00	37.40	37.70	29.20	15.30	8.39
6	10,000	3.82	26.70	55.20	25.00	46.90	33.50	34.70	26.40	14.10	7.79
7	10,000	3.59	28.50	55.20	21.40	38.20	26.60	29.10	22.00	13.20	7.81
8	10,000	3.32	30.60	53.70	22.30	32.90	23.50	32.00	22.10	13.80	7.90
9	10,000	2.96	31.50	50.10	19.00	17.10	15.30	31.20	15.10	13.30	8.83
10	10,000	2.705	25.80	19.90	14.70	12.40	5.74	27.30	6.87	11.70	7.38
11	10,000	Surge									
12	12,000	6.18	16.10	12.70	8.10	39.40	62.30	33.10	43.20	24.20	15.70
13	12,000	6.05	16.70	14.70	9.09	39.40	62.10	65.50	47.50	23.50	12.80
14	12,000	5.89	17.80	17.30	8.84	39.10	63.40	62.80	48.40	23.30	14.90
15	12,000	5.69	19.30	21.00	16.50	37.20	59.80	59.30	45.20	22.90	15.30
16	12,000	5.45	22.40	27.70	16.00	38.00	59.10	55.50	22.50	22.50	13.40
17	12,000	5.18	21.30	26.60	18.10	37.20	57.60	25.60	22.30	10.30	6.97
18	12,000	4.88	23.30	54.20	16.10	70.80	54.20	24.20	20.60	21.30	6.86
19	12,000	4.57	29.20	30.60	13.20	59.10	21.80	21.00	17.90	9.21	5.68
20	12,000	4.14	34.00	31.80	12.50	27.80	20.00	19.30	15.60	7.71	4.87
21	12,000	3.17	18.10	17.60	7.73	12.40	8.54	5.00	6.03	6.40	3.56
22	12,000	Not Recorded									

TABLE C.1. (Cont'd)

Meas. Point	Red. Speed [rpm]	Red. Mass Flowrate [kg/s]	Pressure Readings [mV] Probe Position x/s=0.06	x/s=0.16	x/s=0.31	x/s=0.58	x/s=0.74*	x/s=0.74**	x/s=0.84	x/s=0.94	x/s=1.0
23	14,000	7.36	8.31	10.50	12.70	28.70	43.00	36.60	63.90	15.80	9.72
24	14,000	7.28	9.54	9.26	12.10	25.80	42.60	36.10	60.80	15.10	9.19
25	14,000	7.20	10.80	9.54	12.60	25.00	43.30	35.50	58.40	28.10	9.82
26	14,000	7.05	11.90	9.68	13.50	24.70	45.50	35.40	29.50	14.90	11.00
27	14,000	6.81	13.50	12.90	13.00	23.80	45.60	34.40	28.40	15.40	10.70
28	14,000	6.68	13.80	27.60	13.00	48.20	46.20	33.00	28.80	16.10	10.60
29	14,000	6.41	27.70	32.90	13.70	51.30	44.30	35.10	27.90	16.00	10.30
30	14,000	6.13	32.80	42.20	13.30	46.10	38.00	32.10	26.20	14.10	9.47
31	14,000	5.75	37.70	46.70	13.40	52.20	36.80	30.00	25.00	15.00	10.00
32	14,000	5.04	Rot. Stall								
33	16,500	8.26	18.90	25.50	6.12	31.90	28.90	34.10	27.80	17.70	19.10
34	16,500	8.25	19.10	25.20	6.55	32.00	28.30	34.50	28.80	18.20	19.70
35	16,500	8.18	19.20	24.60	7.38	30.60	29.90	35.10	29.30	19.00	20.10
36	16,500	8.11	19.90	23.90	8.29	30.50	34.80	37.80	33.30	21.80	21.70
38	16,500	8.02	19.10	21.10	7.51	25.20	36.70	34.60	31.70	20.70	19.80
38	16,500	7.92	18.80	18.70	7.67	24.40	41.20	35.20	33.30	20.80	20.30
39	16,500	7.80	18.80	17.30	8.30	25.00	42.90	36.30	35.70	21.80	10.70
40	16,500	7.67	22.40	21.00	8.73	25.30	40.20	35.30	34.30	20.00	10.40
41	16,500	7.46	24.80	26.80	9.46	47.90	45.70	41.30	37.40	11.50	10.90
42	16,500	7.22	24.80	28.90	12.20	43.80	41.30	40.20	18.10	10.40	9.91

* taken at phi=0 degrees

** taken at phi=125 degrees

TABLE C.2. AMPLIFICATION COEFFICIENTS USED IN RECORDING									Tape No.	102	
EXPERIMENTAL MEASUREMENTS									Test Date	11.05.93	
		Red.				Ampl. Coeffs.					
Meas. Point	Red. Speed	Mass Flowrate				Probe Position					
	[rpm]	[kg/s]	x/s=0.06	x/s=0.16	x/s=0.31	x/s=0.58	x/s=0.74*	x/s=0.74**	x/s=0.84	x/s=0.94	x/s=1.0
1	10,000	4.89	16	8	8	16	8	8	4	4	4
2	10,000	4.78	16	8	8	16	8	8	4	4	4
3	10,000	4.61	16	8	8	16	8	8	4	4	4
4	10,000	4.28	8	8	8	16	8	8	4	4	4
5	10,000	4.07	8	16	16	16	8	8	4	4	4
6	10,000	3.82	8	16	16	16	8	8	4	4	4
7	10,000	3.59	8	16	16	16	8	8	4	4	4
8	10,000	3.32	8	16	16	16	8	8	4	4	4
9	10,000	2.96	8	16	16	16	8	8	4	4	4
10	10,000	2.705	8	8	16	16	4	8	2	4	4
11	10,000	Surge	8	4	8	8	4	4	2	2	4
12	12,000	6.18	8	8	4	8	8	4	4	4	4
13	12,000	6.05	8	8	4	8	8	8	4	4	4
14	12,000	5.89	8	8	4	8	8	8	4	4	4
15	12,000	5.69	8	8	8	8	8	8	4	4	4
16	12,000	5.45	8	8	8	8	8	8	2	4	4
17	12,000	5.18	8	8	8	8	8	4	2	2	2
18	12,000	4.88	8	16	8	16	8	4	2	4	2
19	12,000	4.57	8	8	8	16	4	4	2	2	2
20	12,000	4.14	8	8	8	8	4	4	2	2	2
21	12,000	3.17	4	4	4	4	2	1	1	2	2
22	12,000	Not Rcdd.	4	4	4	4	2	4	1	2	2
* at phi=0 degrees			** at phi=125 degrees								

TABLE C.2 (Cont'd)											
		Red.				Ampl. Coeffs.					
Meas.	Red.	Mass									
Point	Speed	Flowrate				Probe Position					
	[rpm]	[kg/s]	x/s=0.06	x/s=0.16	x/s=0.31	x/s=0.58	x/s=0.74*	x/s=0.74**	x/s=0.84	x/s=0.94	x/s=1.0
23	14,000	7.36	4	4	4	4	4	4	4	2	2
24	14,000	7.28	4	4	4	4	4	4	4	2	2
25	14,000	7.20	4	4	4	4	4	4	4	4	2
26	14,000	7.05	4	4	4	4	4	4	2	2	2
27	14,000	6.81	4	4	4	4	4	4	2	2	2
28	14,000	6.68	4	8	4	8	4	4	2	2	2
29	14,000	6.41	8	8	4	8	4	4	2	2	2
30	14,000	6.13	8	8	4	8	4	4	2	2	2
31	14,000	5.75	8	8	4	8	4	4	2	2	2
32	14,000	5.04	2	2	4	4	2	2	1	1	1
33	16,500	8.26	4	4	2	4	4	4	2	2	2
34	16,500	8.25	4	4	2	4	4	4	2	2	2
35	16,500	8.18	4	4	2	4	4	4	2	2	2
36	16,500	8.11	4	4	2	4	4	4	2	2	2
38	16,500	8.02	4	4	2	4	4	4	2	2	2
38	16,500	7.92	4	4	2	4	4	4	2	2	2
39	16,500	7.80	4	4	2	4	4	4	2	2	1
40	16,500	7.67	4	4	2	4	4	4	2	2	1
41	16,500	7.46	4	4	2	8	4	4	2	1	1
42	16,500	7.22	4	4	2	8	4	4	1	1	1
* taken at phi=0 degrees			** taken at phi=125 degrees								

TABLE C.3. AMPLITUDE OF PRESSURE SIGNAL AT BLADE PASSING FREQUENCY--AMPLIFICATION ACCOUNTED FOR									Tape No.	102	
									Test Date	11.05.93	
									Analysis Date	27.07.93	
		Red.				Pressure Readings [mV]					
Meas. Point	Red. Speed	Mass Flowrate				Probe Position					
	[rpm]	[kg/s]	x/s=0.06	x/s=0.16	x/s=0.31	x/s=0.58	x/s=0.74*	x/s=0.74**	x/s=0.84	x/s=0.94	x/s=1.0
1	10,000	4.89	1.81	1.94	1.83	3.57	5.99	6.13	9.40	2.68	4.55
2	10,000	4.78	1.86	2.13	1.70	3.31	5.46	5.65	8.55	4.18	2.43
3	10,000	4.61	2.04	2.64	1.85	3.48	5.54	5.75	8.55	3.90	2.20
4	10,000	4.28	2.44	2.98	1.86	3.26	5.04	5.09	7.78	4.00	2.40
5	10,000	4.07	2.88	3.20	1.74	3.13	4.68	4.71	7.30	3.83	2.10
6	10,000	3.82	3.34	3.45	1.56	2.93	4.19	4.34	6.60	3.53	1.95
7	10,000	3.59	3.56	3.45	1.34	2.39	3.33	3.64	5.50	3.30	1.95
8	10,000	3.32	3.83	3.36	1.39	2.06	2.94	4.00	5.53	3.45	1.98
9	10,000	2.96	3.94	3.13	1.19	1.07	1.91	3.90	3.78	3.33	2.21
10	10,000	2.705	3.23	2.49	0.92	0.78	1.44	3.41	3.44	2.93	1.85
11	10,000	Surge									
12	12,000	6.18	2.01	1.59	2.03	4.93	7.79	8.28	10.80	6.05	3.93
13	12,000	6.05	2.09	1.84	2.27	4.93	7.76	8.19	11.88	5.88	3.20
14	12,000	5.89	2.23	2.16	2.21	4.89	7.93	7.85	12.10	5.83	3.73
15	12,000	5.69	2.41	2.63	2.06	4.65	7.48	7.41	11.30	5.73	3.83
16	12,000	5.45	2.80	3.46	2.00	4.75	7.39	6.94	11.25	5.63	3.35
17	12,000	5.18	2.66	3.33	2.26	4.65	7.20	6.40	11.15	5.15	3.49
18	12,000	4.88	2.91	3.39	2.01	4.43	6.78	6.05	10.30	5.33	3.43
19	12,000	4.57	3.65	3.83	1.65	3.69	5.45	5.25	8.95	4.61	2.84
20	12,000	4.14	4.25	3.98	1.56	3.48	5.00	4.83	7.80	3.86	2.44
21	12,000	3.17	4.53	4.40	1.93	3.10	4.27	5.00	6.03	3.20	1.78
22	12,000	Not Recorded									

TABLE C.3. (Cont'd)											
		Red.				Pressure Readings [mV]					
Meas.	Red.	Mass									
Point	Speed	Flowrate				Probe Position					
	[rpm]	[kg/s]	x/s=0.06	x/s=0.16	x/s=0.31	x/s=0.58	x/s=0.74*	x/s=0.74**	x/s=0.84	x/s=0.94	x/s=1.0
23	14,000	7.36	2.08	2.63	3.18	7.18	10.75	9.15	15.98	7.90	4.86
24	14,000	7.28	2.39	2.32	3.03	6.45	10.65	9.03	15.20	7.55	4.60
25	14,000	7.20	2.70	2.39	3.15	6.25	10.83	8.88	14.60	7.03	4.91
26	14,000	7.05	2.98	2.42	3.38	6.18	11.38	8.85	14.75	7.45	5.50
27	14,000	6.81	3.38	3.23	3.25	5.95	11.40	8.60	14.20	7.70	5.35
28	14,000	6.68	3.45	3.45	3.25	6.03	11.55	8.25	14.40	8.05	5.30
29	14,000	6.41	3.46	4.11	3.43	6.41	11.08	8.78	13.95	8.00	5.15
30	14,000	6.13	4.10	5.28	3.33	5.76	9.50	8.03	13.10	7.05	4.74
31	14,000	5.75	4.71	5.84	3.35	6.53	9.20	7.50	12.50	7.50	5.00
32	14,000	5.04									
33	16,500	8.26	4.73	6.38	3.06	7.98	7.23	8.53	13.90	8.85	9.55
34	16,500	8.25	4.78	6.30	3.28	8.00	7.08	8.63	14.40	9.10	9.85
35	16,500	8.18	4.80	6.15	3.69	7.65	7.48	8.78	14.65	9.50	10.05
36	16,500	8.11	4.98	5.98	4.15	7.63	8.70	9.45	16.65	10.90	10.85
38	16,500	8.02	4.78	5.28	3.76	6.30	9.18	8.65	15.85	10.35	9.90
38	16,500	7.92	4.70	4.68	3.84	6.10	10.30	8.80	16.65	10.40	10.15
39	16,500	7.80	4.70	4.33	4.15	6.25	10.73	9.08	17.85	10.90	10.70
40	16,500	7.67	5.60	5.25	4.37	6.33	10.05	8.83	17.15	10.00	10.40
41	16,500	7.46	6.20	6.70	4.73	5.99	11.43	10.33	18.70	11.50	10.90
42	16,500	7.22	6.20	7.23	6.10	5.48	10.33	10.05	18.10	10.40	9.91
* taken at phi=0 degrees			** taken at phi=125 degrees								

TABLE C.4. AMPLITUDE OF NON-DIMENSIONALIZED PRESSURE (=Pb/P2) AT BLADE PASSING FREQUENCY									Tape No.	102	
									Test Date	11.05.93	
									Analysis Date	27.07.93	
		Red.			Non-dimens. Press. [x 10 E-4]						
Meas. Point	Red. Speed	Mass Flowrate			Probe Position						
	[rpm]	[kg/s]	x/s=0.06	x/s=0.16	x/s=0.31	x/s=0.58	x/s=0.74*	x/s=0.74**	x/s=0.84	x/s=0.94	x/s=1.0
1	10,000	4.89	13.9	14.9	14.0	27.4	46.0	47.1	72.2	20.6	35.0
2	10,000	4.78	14.1	16.1	12.9	25.2	41.5	42.9	65.0	31.7	18.5
3	10,000	4.61	15.4	19.9	13.9	26.2	41.7	43.3	64.4	29.4	16.5
4	10,000	4.28	18.1	22.0	13.8	24.1	37.3	37.7	57.6	29.6	17.8
5	10,000	4.07	21.1	23.4	12.8	22.9	34.2	34.5	53.5	28.0	15.4
6	10,000	3.82	24.3	25.1	11.4	21.3	30.5	31.6	48.0	25.6	14.2
7	10,000	3.59	25.7	24.9	9.7	17.2	24.0	26.3	39.7	23.8	14.1
8	10,000	3.32	27.4	24.1	10.0	14.7	21.1	28.7	39.6	24.7	14.2
9	10,000	2.96	28.3	22.5	8.5	7.7	13.7	28.0	27.1	23.9	15.9
10	10,000	2.705	23.2	17.9	6.6	5.6	10.3	24.6	24.8	21.1	13.3
11	10,000	Surge									
12	12,000	6.18	16.5	13.0	16.6	40.4	63.9	68.0	88.7	49.7	32.2
13	12,000	6.05	17.1	15.0	18.6	40.3	63.5	67.0	97.1	48.0	26.2
14	12,000	5.89	18.0	17.5	17.9	39.6	64.2	63.6	98.0	47.2	30.2
15	12,000	5.69	19.3	21.0	16.5	37.3	59.9	59.4	90.6	45.9	30.7
16	12,000	5.45	22.2	27.4	15.9	37.6	58.5	55.0	89.2	44.6	26.5
17	12,000	5.18	20.9	26.2	17.8	36.6	56.6	50.3	87.7	40.5	27.4
18	12,000	4.88	22.8	26.5	15.7	34.6	53.0	47.3	80.5	41.6	26.8
19	12,000	4.57	28.4	29.7	12.8	28.7	42.4	40.8	69.6	35.8	22.1
20	12,000	4.14	32.6	30.5	12.0	26.7	38.4	37.0	59.9	29.6	18.7
21	12,000	3.17	34.1	33.2	14.6	23.4	32.2	37.7	45.5	24.1	13.4
22	12,000	Not Recorded									

TABLE C.4. (Cont'd)

Meas. Point	Red. Speed [rpm]	Red. Mass Flowrate [kg/s]	Non-dimens. Press. [x 10 E-4] Probe Position x/s=0.06	x/s=0.16	x/s=0.31	x/s=0.58	x/s=0.74*	x/s=0.74**	x/s=0.84	x/s=0.94	x/s=1.0
23	14,000	7.36	16.6	20.9	25.3	57.2	85.7	72.9	127.3	62.9	38.7
24	14,000	7.28	18.8	18.3	23.9	50.9	84.1	71.3	120.1	59.6	36.3
25	14,000	7.20	21.1	18.6	24.6	48.9	84.6	69.4	114.1	54.9	38.4
26	14,000	7.05	23.0	18.7	26.1	47.7	87.9	68.4	114.0	57.6	42.5
27	14,000	6.81	25.8	24.7	24.9	45.5	87.3	65.8	108.7	58.9	41.0
28	14,000	6.68	26.1	26.1	24.6	45.5	87.3	62.3	108.8	60.8	40.0
29	14,000	6.41	25.9	30.8	25.6	48.0	82.9	65.7	104.4	59.9	38.6
30	14,000	6.13	30.4	39.2	24.7	42.8	70.5	59.6	97.2	52.3	35.1
31	14,000	5.75	34.8	43.1	24.8	48.2	68.0	55.4	92.4	55.4	37.0
32	14,000	5.04									
33	16,500	8.26	37.5	50.7	24.3	63.4	57.4	67.7	110.5	70.3	75.9
34	16,500	8.25	37.9	49.9	26.0	63.4	56.1	68.4	114.1	72.1	78.1
35	16,500	8.18	37.1	47.5	28.5	59.1	57.7	67.8	113.1	73.4	77.6
36	16,500	8.11	37.9	45.5	31.5	58.0	66.2	71.9	126.7	82.9	82.6
38	16,500	8.02	35.6	39.3	28.0	46.9	68.3	64.4	118.0	77.1	73.7
38	16,500	7.92	34.3	34.2	28.0	44.6	75.3	64.3	121.7	76.0	74.2
39	16,500	7.80	33.8	31.1	29.9	45.0	77.2	65.3	128.4	78.4	77.0
40	16,500	7.67	39.6	37.1	30.8	44.7	71.0	62.3	121.2	70.6	73.5
41	16,500	7.46	42.7	46.2	32.6	41.3	78.7	71.2	128.9	79.3	75.1
42	16,500	7.22	42.3	49.3	41.7	37.4	70.5	68.6	123.6	71.0	67.7

* taken at phi=0 degrees ** taken at phi=125 degrees

TABLE C.5. AMPLITUDE OF PRESSURE COEFFICIENT AT BLADE PASSING FREQUENCY

Tape No. 102
Test Date 11.05.93
Analysis Date 27.07.93

Meas. Point	Red. Speed [rpm]	Flow Coeff. [-]	Pressure Coefficient [x 10 E-2] Probe Position x/s=0.06	x/s=0.16	x/s=0.31	x/s=0.58	x/s=0.74*	x/s=0.84	x/s=0.94	x/s=1.0
1	10,000	0.155	0.69	0.74	0.70	1.36	2.27	3.57	1.02	1.73
2	10,000	0.151	0.71	0.81	0.65	1.26	2.07	3.25	1.59	0.92
3	10,000	0.146	0.78	1.00	0.70	1.32	2.11	3.25	1.48	0.84
4	10,000	0.136	0.93	1.13	0.71	1.24	1.92	2.96	1.52	0.91
5	10,000	0.129	1.10	1.22	0.66	1.19	1.78	2.78	1.46	0.80
6	10,000	0.121	1.27	1.31	0.59	1.12	1.60	2.51	1.34	0.74
7	10,000	0.114	1.36	1.31	0.51	0.91	1.27	2.10	1.26	0.74
8	10,000	0.105	1.46	1.28	0.53	0.79	1.12	2.11	1.32	0.76
9	10,000	0.094	1.50	1.19	0.45	0.41	0.73	1.44	1.27	0.84
10	10,000	0.086	1.23	0.95	0.35	0.30	0.55	1.31	1.12	0.71
11	10,000	Surge								
12	12,000	0.164	0.53	0.42	0.54	1.31	2.07	2.87	1.61	1.04
13	12,000	0.161	0.56	0.49	0.60	1.31	2.06	3.16	1.56	0.85
14	12,000	0.157	0.59	0.58	0.59	1.30	2.11	3.22	1.55	0.99
15	12,000	0.151	0.64	0.70	0.55	1.24	1.99	3.01	1.53	1.02
16	12,000	0.145	0.75	0.92	0.53	1.27	1.97	3.00	1.50	0.89
17	12,000	0.138	0.71	0.89	0.60	1.24	1.92	2.97	1.37	0.93
18	12,000	0.13	0.78	0.91	0.54	1.18	1.81	2.75	1.42	0.92
19	12,000	0.122	0.98	1.03	0.44	0.99	1.46	2.39	1.23	0.76
20	12,000	0.111	1.14	1.06	0.42	0.93	1.34	2.09	1.03	0.65
21	12,000	0.085	1.21	1.18	0.52	0.83	1.14	1.61	0.86	0.48
22	12,000	Not Recorded								

TABLE C.5. (Cont'd)

Meas. Point	Red. Speed [rpm]	Flow Coeff. [-]	Pressure Coefficient [x 10 E-2] Probe Position x/s=0.06	x/s=0.16	x/s=0.31	x/s=0.58	x/s=0.74*	x/s=0.84	x/s=0.94	x/s=1.0
23	14,000	0.17	0.41	0.52	0.63	1.42	2.13	3.16	1.56	0.96
24	14,000	0.168	0.47	0.46	0.60	1.28	2.11	3.01	1.50	0.91
25	14,000	0.166	0.53	0.47	0.62	1.24	2.14	2.89	1.39	0.97
26	14,000	0.163	0.59	0.48	0.67	1.22	2.25	2.92	1.48	1.09
27	14,000	0.158	0.67	0.64	0.64	1.18	2.26	2.82	1.53	1.06
28	14,000	0.154	0.68	0.68	0.64	1.20	2.29	2.85	1.60	1.05
29	14,000	0.148	0.69	0.81	0.68	1.27	2.20	2.76	1.59	1.02
30	14,000	0.142	0.81	1.05	0.66	1.14	1.89	2.60	1.40	0.95
31	14,000	0.133	0.93	1.16	0.66	1.30	1.82	2.48	1.49	0.99
32	14,000									
33	16,500	0.162	0.68	0.91	0.44	1.14	1.30	1.99	1.27	1.37
34	16,500	0.162	0.68	0.90	0.47	1.14	1.01	2.06	1.30	1.41
35	16,500	0.161	0.69	0.88	0.53	1.09	1.07	2.09	1.36	1.44
36	16,500	0.159	0.71	0.85	0.59	1.09	1.24	2.38	1.56	1.55
37	16,500	0.158	0.68	0.75	0.54	0.90	1.31	2.27	1.48	1.42
38	16,500	0.155	0.67	0.67	0.55	0.87	1.47	2.38	1.49	1.45
39	16,500	0.153	0.67	0.62	0.59	0.89	1.53	2.55	1.56	1.53
40	16,500	0.151	0.80	0.75	0.62	0.90	1.44	2.45	1.43	1.49
41	16,500	0.147	0.89	0.96	0.68	0.86	1.63	2.67	1.64	1.56
42	16,500	0.142	0.89	1.03	0.87	0.78	1.48	2.59	1.49	1.42

* taken at phi=0 degrees

APPENDIX D--PLOTS OF NORMALIZED BLADE-TO-BLADE PRESSURE DIFFERENCE

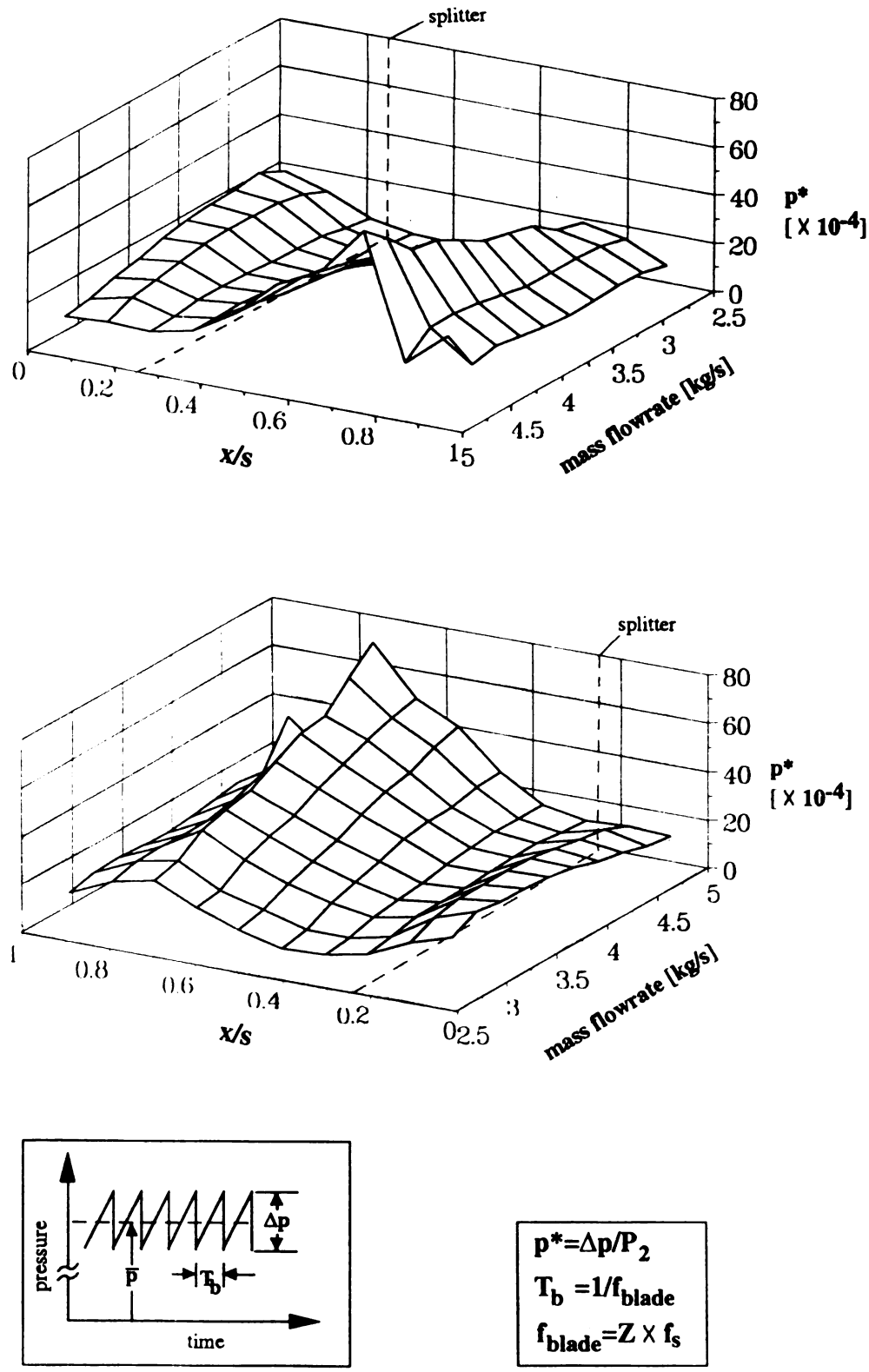

Fig. D.1. Non-dimension. blade-to-blade pressure rise, N_{red}=10,000 rpm

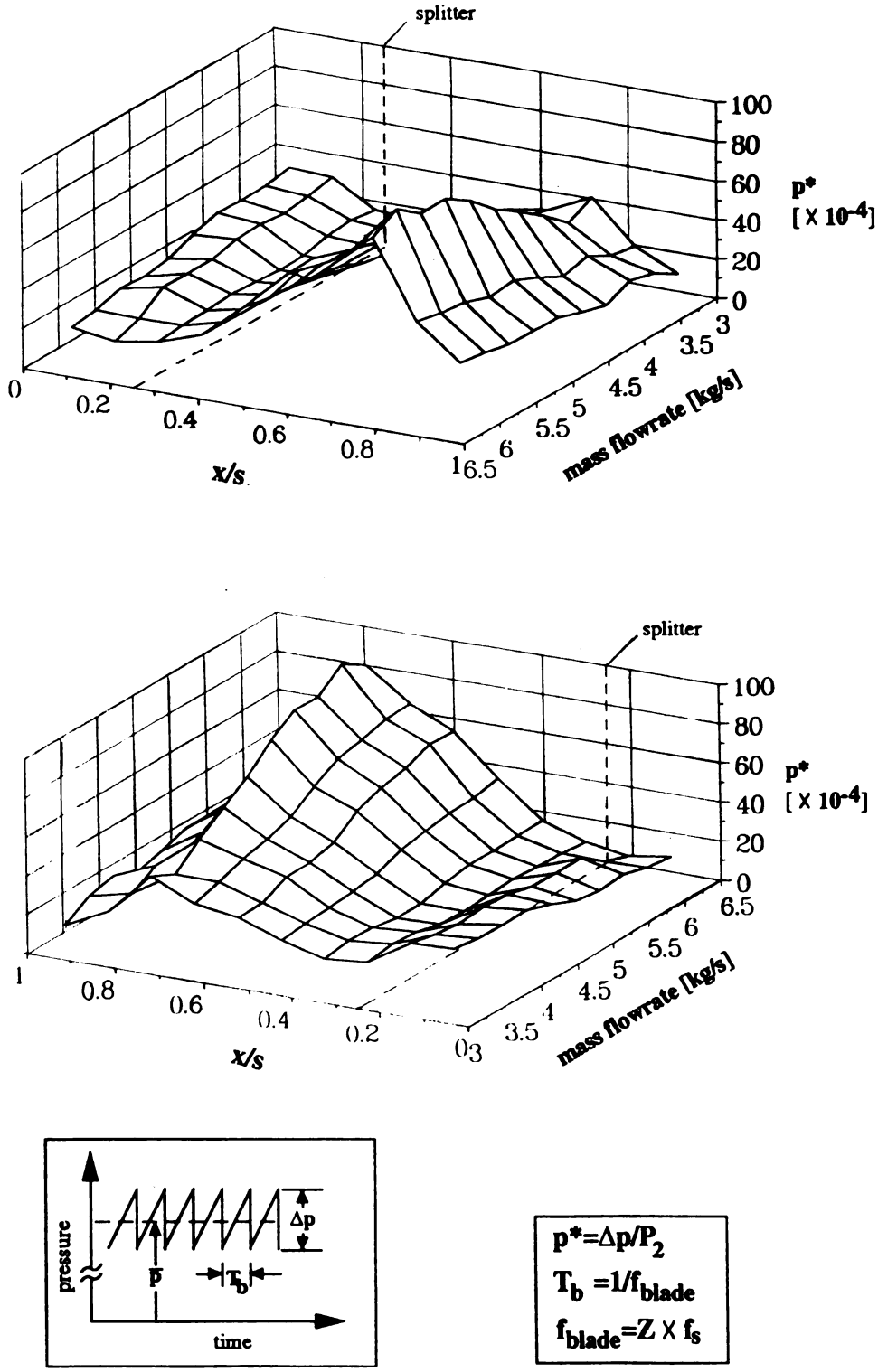

Fig. D.2. Non-dimension. blade-to-blade pressure rise, N_{red}=12,000 rpm

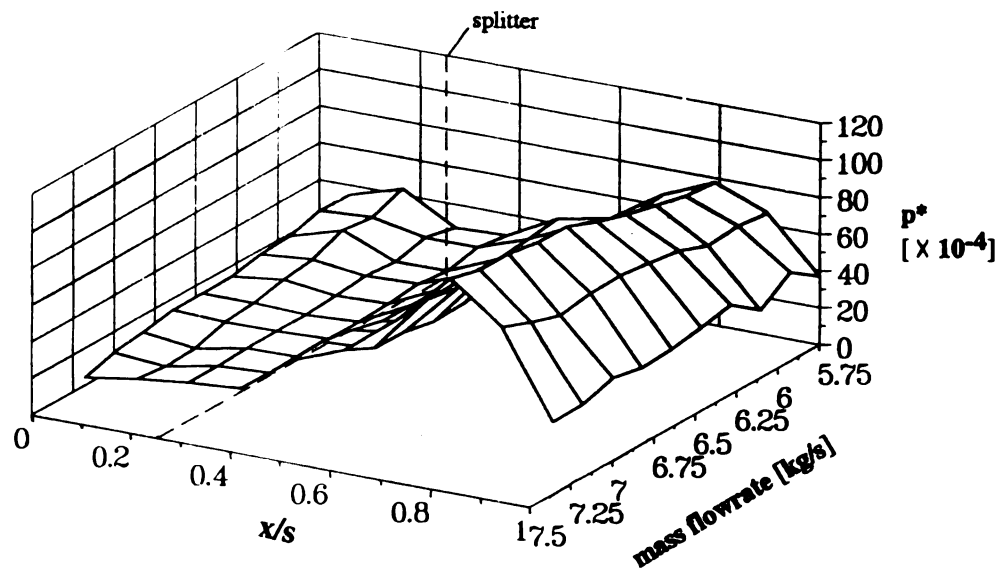

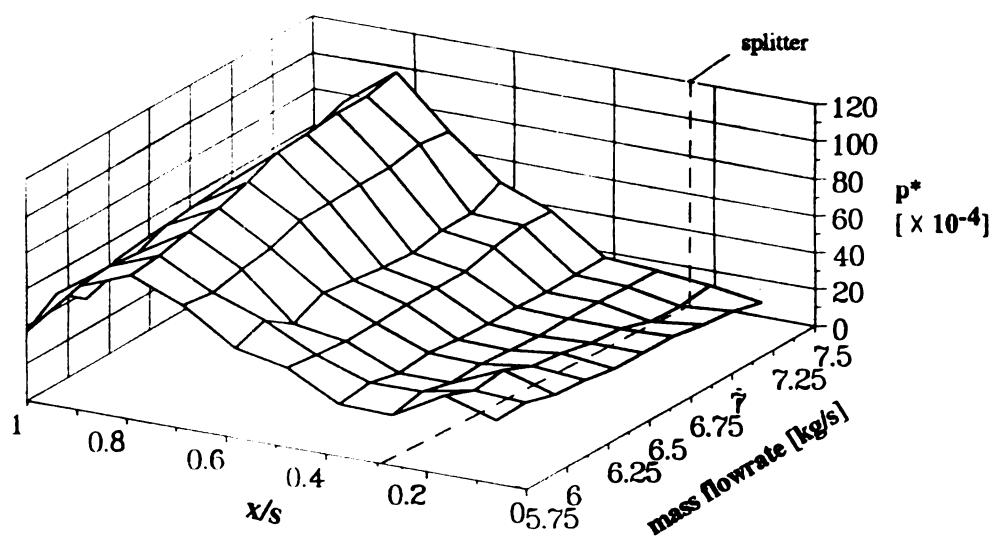

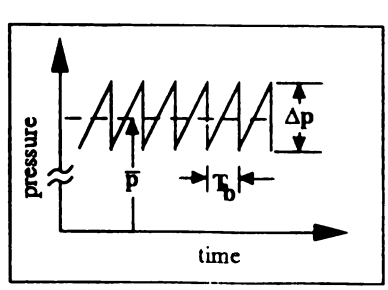

$p^* = \Delta p / P_2$

$T_b = 1/f_{blade}$

$f_{blade} = Z \times f_s$

Fig. D.3. Non-dimension. blade-to-blade pressure rise, N_{red}=14,000 rpm

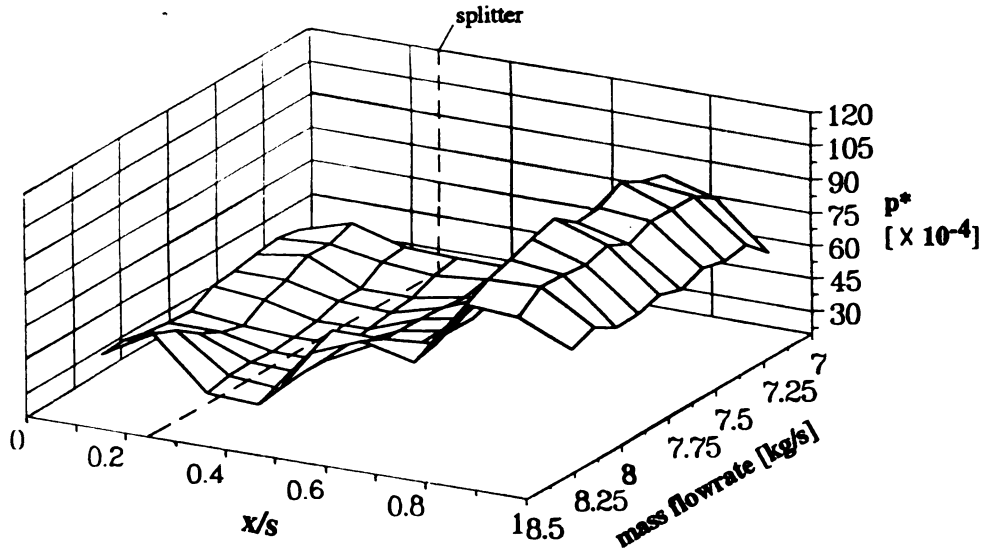

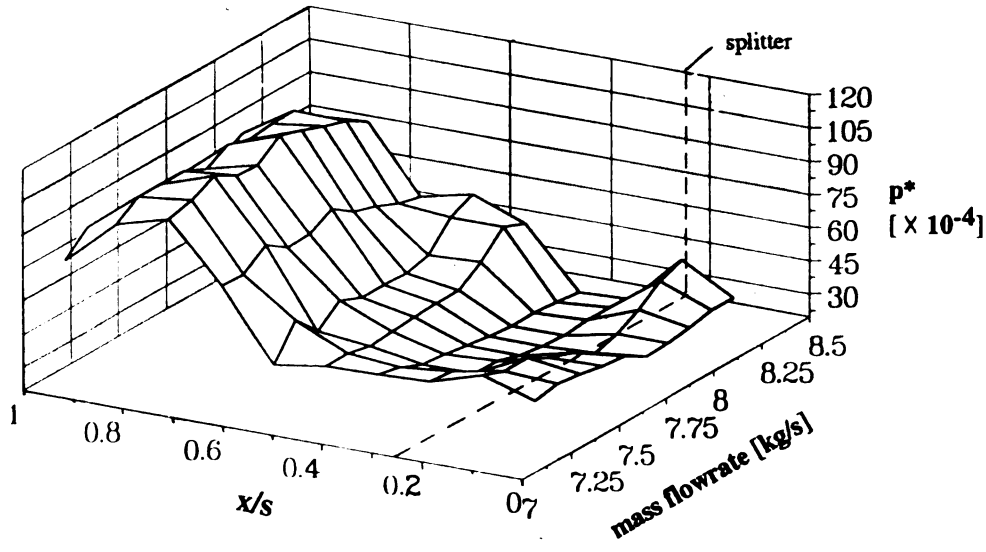

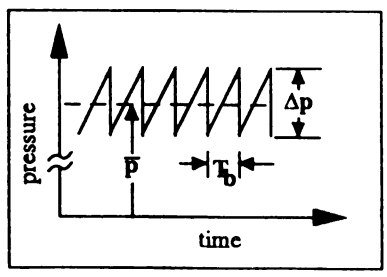

$p^* = \Delta p / P_2$

$T_b = 1/f_{blade}$

$f_{blade} = Z \times f_s$

Fig. D.4. Non-dimension. blade-to-blade pressure rise, N_{red}=16,500 rpm

APPENDIX E--MISCELLANEOUS GRAPHS

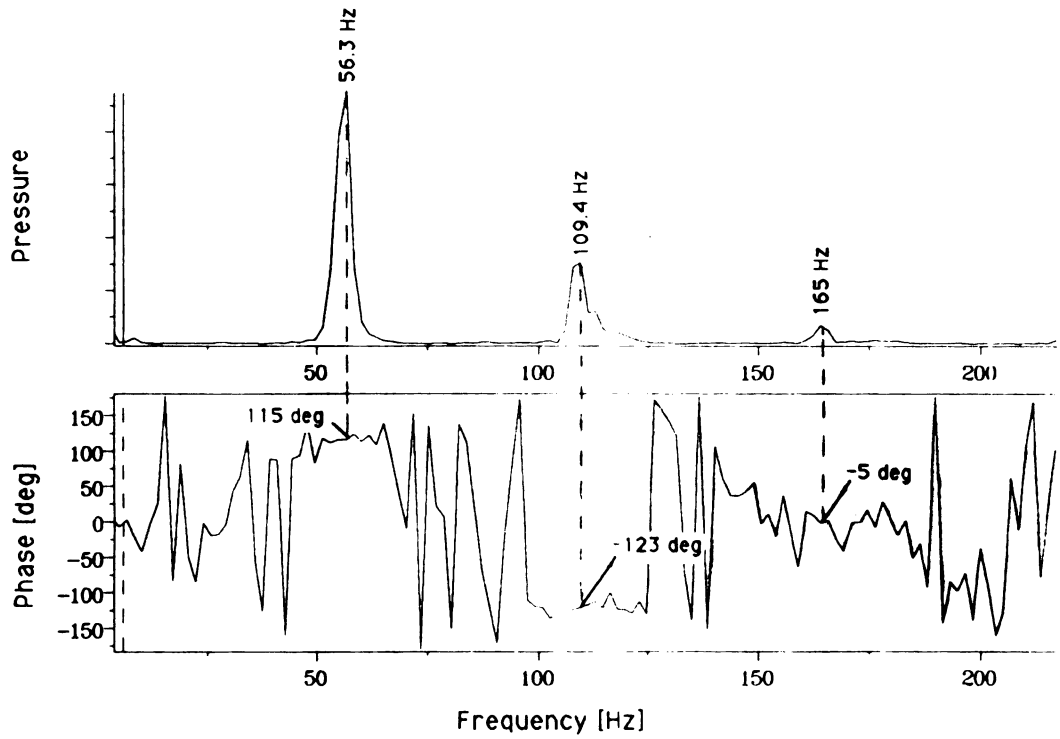

Fig. E.1. Pressure & phase spectra for rotating stall, N_{red}=10,000 rpm

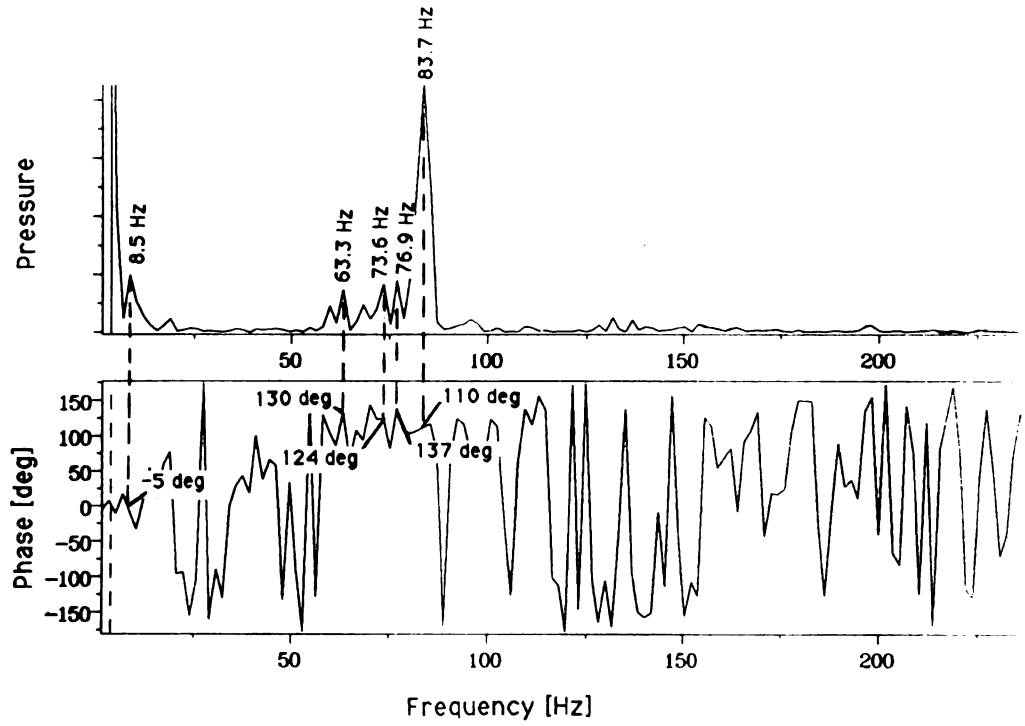

Fig. E.2. Pressure & phase spectra for surge, N_{red}=12,000 rpm

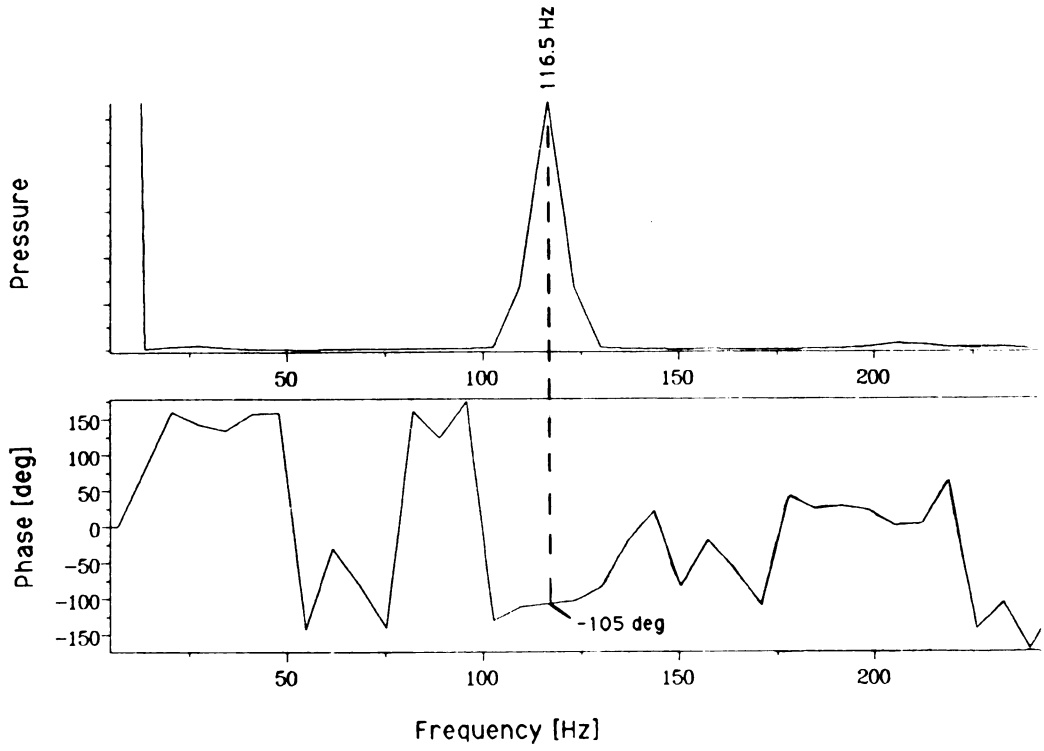

Fig. E.3. Pressure & phase spectra for second rotating stall in event A, N_{red}=14,000 rpm

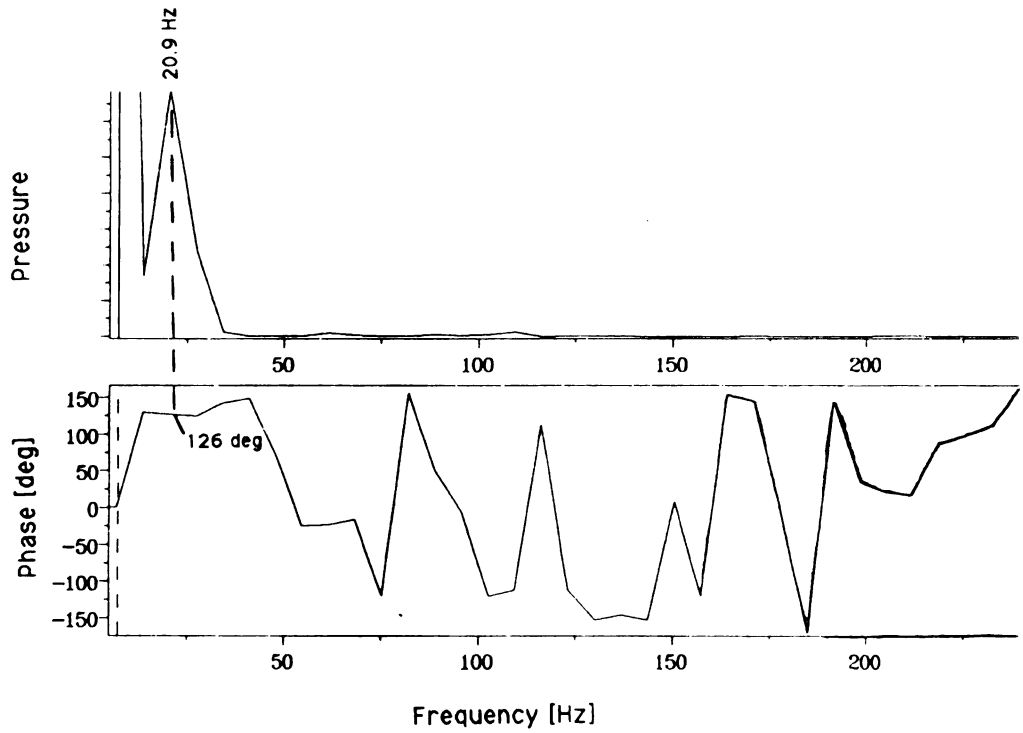

Fig. E.4. Pressure and phase spectra for second segment of event C, N_{red}=14,000 rpm

APPENDIX F--RESULTS OF ANALYSES OF UNSTEADY EVENTS

APPENDIX F--ANALYSES OF UNSTEADY EVENTS

Section	Analyzer	Phase Analysis				Blade Vib. Analysis		comments
		f_p [Hz]	$\Delta\phi_{st}$ [deg]	$\Delta\phi_{st}$ range [deg]	Possible m-values	f_b [Hz]	Possible m-values	
10,000 rpm Rotating Stall	DIA/ DAGO	56	115	115 to 119	m=-5 ($\Delta\phi_{st}$=95) m=-2 ($\Delta\phi_{st}$=110) **m=+1 ($\Delta\phi_{st}$=125)** m=+4 ($\Delta\phi_{st}$=140)	117 236	**m=+1.02** m=-1.07	•Pressure peaks listed from most to least prominent.
	DIA/ DAGO	108 165	-120 -5	-115 to -126 -20 to 5	Analysis reveals that both of these are caused by the same event which causes the 56 Hz reading.			

APPENDIX F--ANALYSIS OF UNSTEADY EVENTS

Section	Analyzer	Phase Analysis				Blade Vib. Analysis		comments
		f_p [Hz]	$\Delta\phi_{st}$ [deg]	$\Delta\phi_{st}$ range [deg]	Possible m-values	f_b [Hz]	Possible m-values	
10,000 rpm Surge	DIA/ DAGO	54	118	112 to 124	m=-5 ($\Delta\phi_{st}$=95) m=-2 ($\Delta\phi_{st}$=110) m=+1 ($\Delta\phi_{st}$=125) m=+4 ($\Delta\phi_{st}$=140)	117 233 1204 1289 1440	**m=+1.01** m=-1.06 -- -- --	•Pressure peaks listed from least to most prominent.
	DIA/ DAGO	109 161	-128 -5	-122 to -128 -5 to 0	Analysis reveals that both of these are caused by the same event which causes the 54 Hz reading.			
10,000 rpm Surge	FFT Analyzer	54 112	118 -113	112 to 122 -109 to -120	Same as above			•Coherence = 0.96 for 56 Hz and 0.93 for 108 Hz. •Pressure peaks listed from lowest to highest frequency.

APPENDIX F--ANALYSES OF UNSTEADY EVENTS

Section	Analyzer	Phase Analysis				Blade Vib. Analysis		comments
		f_p [Hz]	$\Delta\phi_{st}$ [deg]	$\Delta\phi_{st}$ range [deg]	Possible m-values	f_b [Hz]	Possible m-values	
12,000 rpm Surge (1st Section)	DIA/ DAGO	62	136	-8 to 136 (mostly 124 to136)	m=-5 ($\Delta\phi_{st}$=95) m=-2 ($\Delta\phi_{st}$=110) m=+1 ($\Delta\phi_{st}$=125) m=+4 ($\Delta\phi_{st}$=140) m=+7 ($\Delta\phi_{st}$=155)	144 766 828 1094 1236 1265	m=+0.98 m=+4.08 -- m=-5.08 -- m=-5.93	•Used shaft freq.=203 •Pressure peaks listed from most to least prominent.
	DIA/ DAGO	89	-169	-100 to -176	Analysis reveals that this peak is caused by the same event which causes the 62 Hz reading.			
	DIA/ DAGO	137	-5	-29 to 32	m=-3 ($\Delta\phi_{st}$=-15) m=+3 ($\Delta\phi_{st}$=15)	144 766 828 1094 1236 1265	-- m=-3.10 -- m=+6.06 -- m=+6.91	

APPENDIX F--ANALYSES OF UNSTEADY EVENTS

Section	Analyzer	Phase Analysis				Blade Vib. Analysis		comments
		f_p [Hz]	$\Delta\phi_{st}$ [deg]	$\Delta\phi_{st}$ range [deg]	Possible m-values	f_b [Hz]	Possible m-values	
12,000 rpm Surge (2nd section, i.e. mid-section)	DIA/ DAGO	82	114	92 to 127	m=-5 ($\Delta\phi_{st}$=95) m=-2 ($\Delta\phi_{st}$=110) m=+1 ($\Delta\phi_{st}$=125) m=+4 ($\Delta\phi_{st}$=140)	--		•Used shaft freq.=203. •Pressure peaks listed from most to least prominent.
12,000 rpm Surge (3rd Section)	DIA/ DAGO	76	115	98 to 117	same as above	137 1265	**m=+1.05** --	•Used shaft freq.=203.
12,000 rpm Surge (Entire Section)	DIA/ DAGO	84	110	83 to 111	same as above	136 1257 1275 1288	**m=+1.08** -- -- m=-5.93	•Used shaft freq.=203. •Peak at 84 Hz clearly dominates.
	DIA/ DAGO	60 to 77	118	96 to 137	same as above	same	nearly same as above	•Distinct peaks at 77,74,63,60 and 68 Hz (largest to smallest).

ANALYSIS OF ROTATING STALL

Section	Analyzer	Phase Analysis				Blade Vib. Analysis		comments
		f_p [Hz]	$\Delta\phi_{st}$ [deg]	$\Delta\phi_{st}$ range [deg]	Possible m-values	f_b [Hz]	Possible m-values	
12,000 rpm Surge	FFT Analyzer	62	130	122 to 135	m=-2 ($\Delta\phi_{st}$=110) m=+1 ($\Delta\phi_{st}$=125) m=+4 ($\Delta\phi_{st}$=140)			•Coherence = 0.96. •Phase and coherence info. are for three samples. •Pressure peaks listed from lowest to highest frequency.
		74 to 76	121	119 to 123	m=-2 ($\Delta\phi_{st}$=110) m=+1 ($\Delta\phi_{st}$=125) m=+4 ($\Delta\phi_{st}$=140)			•Coherence = 0.91. •Phase and coherence info. are for four samples.
14,000 rpm Rot. Stall, (Occur-rence A,1st Rot. Stall)	DIA/ DAGO	34	-7	-13 to 21	**m=-3** (**$\Delta\phi_{st}$=-15**) m=+3 ($\Delta\phi_{st}$=15)	753 465	**m=-3.01** m=-5.99	•Used shaft freq.=239. •472, 718, 953, 1191, & 1430 Hz peaks are all associated with shaft freq. Therefore, not associated with rot. stall.

APPENDIX F--ANALYSES OF UNSTEADY EVENTS

Section	Analyzer	Phase Analysis				Blade Vib. Analysis		comments
		f_p [Hz]	$\Delta\phi_{st}$ [deg]	$\Delta\phi_{st}$ range [deg]	Possible m-values	f_b [Hz]	Possible m-values	
14,000 rpm Rot. Stall, (Occur-rence A, 2nd Rot. Stall)	DIA/ DAGO	117	-105	-102 to -112	m=+5 ($\Delta\phi_{st}$=-95) m=+2 ($\Delta\phi_{st}$=-110) m=-1 ($\Delta\phi_{st}$=-125)	1087 1238	m=-4.06 or m=+5.04 --	•Used shaft freq.=239 Hz
14,000 rpm Rot. Stall, (Occur. A)	FFT Analyzer	115	-107	-107 to -108	m=+5 ($\Delta\phi_{st}$=-95) m=+2 ($\Delta\phi_{st}$=-110) m=-1 ($\Delta\phi_{st}$=-125)			•Coherence = 1.0
14,000 rpm Unstead. between occur. A & occur. B	FFT Analyzer	30	-15	-14 to -16	m=-3 ($\Delta\phi_{st}$=-15)			•Coherence = 0.99

APPENDIX F--ANALYSES OF UNSTEADY EVENTS

Section	Analyzer	Phase Analysis				Blade Vib. Analysis		comments
		f_p [Hz]	$\Delta\phi_{st}$ [deg]	$\Delta\phi_{st}$ range [deg]	Possible m-values	f_b [Hz]	Possible m-values	
14,000 rpm Rot. Stall, (Occur. B)	DIA/ DAGO	48	18	-10 to 98	**m=-3** (**$\Delta\phi_{st}$=-15**) m=+3 ($\Delta\phi_{st}$=15) m=-5 ($\Delta\phi_{st}$=95) m=-2 ($\Delta\phi_{st}$=110)	157 609 766 916 1292	-- -- **m=-3.00** m=+4.03 --	•Used: shaft freq.=239 Hz. •Pressure spectra peak is very broad for lower frequencies. Appears that f_p=30 to 50 Hz can be considered main part of peak. •Pressure peaks listed from most to least prominent. •Coherence = 1.0
	DIA/ DAGO	83	133	120 to 146	**m=-2** (**$\Delta\phi_{st}$=110**) **m=+1** (**$\Delta\phi_{st}$=125**) m=+4 ($\Delta\phi_{st}$=140) m=+7 ($\Delta\phi_{st}$=155)	157 609 766 916 1292	**m=+1.00** m=+2.90 or **m=-1.99** -- -- m=-5.06	•Unable to conclusively determine if 83 Hz peak is related to 48 Hz peak. • f_b=157 is probably alias of II. Mode.

APPENDIX F--ANALYSES OF UNSTEADY EVENTS

Section	Analyzer	Phase Analysis				Blade Vib. Analysis		comments
		f_p [Hz]	$\Delta\phi_{st}$ [deg]	$\Delta\phi_{st}$ range [deg]	Possible m-values	f_b [Hz]	Possible m-values	
14,000 rpm Rot. Stall, (Occur-rence B)	DIA/ DAGO	129	77	-45 to 167	m=-3 ($\Delta\phi_{st}$=-15) **m=+3 ($\Delta\phi_{st}$=15)** m=-5 ($\Delta\phi_{st}$=95) **m=-2 ($\Delta\phi_{st}$=110)** m=+1 ($\Delta\phi_{st}$=125) m=+4 ($\Delta\phi_{st}$=140) m=+7 ($\Delta\phi_{st}$=155)	157 609 766 916 1292	-- **m=-2.01 or m=+3.09** -- -- m=+5.95	•Pressure peaks listed from most to least prominent.
	DIA/ DAGO	34	100	95 to 100	m=-5 ($\Delta\phi_{st}$=95) m=-2 ($\Delta\phi_{st}$=110)	157 609 766 916 1292	-- -- m=-3.06 m=+3.9 7	

ANALYSIS OF ROTATING STALL

Section	Analyzer	Phase Analysis				Blade Vib. Analysis		comments
		f_p [Hz]	$\Delta\phi_{st}$ [deg]	$\Delta\phi_{st}$ range [deg]	Possible m-values	f_b [Hz]	Possible m-values	
14,000 rpm Rot. Stall, (Occur-rence B)	FFT Analyzer	45	4		m=-3 ($\Delta\phi_{st}$=-15) m=+3 ($\Delta\phi_{st}$=15)	762	m=-3.01	•Coherence = 1.0. •Shaft frequency = 238 Hz. •762 Hz peak was most prominent. •Pressure peaks listed from lowest to highest frequencies.
	FFT Analyzer	85	154	150 to 155	m=+4 ($\Delta\phi_{st}$=140) m=+7 ($\Delta\phi_{st}$=155)			•Coherence = 1.0
	FFT Analyzer	131	128	121 to 133	m=-2 ($\Delta\phi_{st}$=110) m=+1 ($\Delta\phi_{st}$=125) m=+4 ($\Delta\phi_{st}$=140)			•Coherence = 1.0

APPENDIX F--ANALYSES OF UNSTEADY EVENTS

Section	Analyzer	Phase Analysis				Blade Vib. Analysis		comments
		f_p [Hz]	$\Delta\phi_{st}$ [deg]	$\Delta\phi_{st}$ range [deg]	Possible m-values	f_b [Hz]	Possible m-values	
14,000 rpm Unstead. between occur. B & occur. C	FFT Analyzer	30	-15		m=-3 ($\Delta\phi_{st}$=-15) m=+3 ($\Delta\phi_{st}$=15)			•Coherence = 1.0 •Shaft frequency = 238 Hz.
14,000 rpm Rot. Stall, (Occur. C, 1st Rot. Stall)	DIA/ DAGO	48	-1	-9 to 57	**m=-3 ($\Delta\phi_{st}$=-15)** m=+3 ($\Delta\phi_{st}$=15)	767 1245 1539	**m=-3.01** m=-5.01 --	•$\Delta\phi_{st}$ is mostly between -9 and 14 degrees. •Shaft frequency = 239 Hz.
14,000 rpm Rot. Stall, (Occur-rence C, 2nd Rot. Stall)	DIA/ DAGO	21	126	125 to 142	m=-2 ($\Delta\phi_{st}$=110) m=+1 ($\Delta\phi_{st}$=125) **m=+4 ($\Delta\phi_{st}$=140)** m=+7 ($\Delta\phi_{st}$=155)		**m=+4.01** -- m=+5.04 -- -- m=+6.04	

APPENDIX F--ANALYSES OF UNSTEADY EVENTS

Section	Analyzer	Phase Analysis				Blade Vib. Analysis		comments
		f_p [Hz]	$\Delta\phi_{st}$ [deg]	$\Delta\phi_{st}$ range [deg]	Possible m-values	f_b [Hz]	Possible m-values	
14,000 rpm Rot. Stall, (Occur-rence C)	FFT Analyzer	51	-7	-5 to -9	m=-3 ($\Delta\phi_{st}$=-15) m=+3 ($\Delta\phi_{st}$=15)			•Coherence = 1.0 •Shaft frequency = 238 Hz.
	FFT Analyzer	22	133		m=-2 ($\Delta\phi_{st}$=110) m=+1 ($\Delta\phi_{st}$=125) m=+4 ($\Delta\phi_{st}$=140)			•Coherence = 0.99
14,000 rpm Unstead. between occurrence C & occur. D	FFT Analyzer	34	-10		m=-3 ($\Delta\phi_{st}$=-15) m=+3 ($\Delta\phi_{st}$=15)			•Coherence = 1.0

APPENDIX F--ANALYSES OF UNSTEADY EVENTS

Section	Analyzer	Phase Analysis				Blade Vib. Analysis		comments
		f_p [Hz]	$\Delta\phi_{st}$ [deg]	$\Delta\phi_{st}$ range [deg]	Possible m-values	f_b [Hz]	Possible m-values	
14,000 rpm Rot. Stall, (Occur-rence D, Cut #1)	DIA/ DAGO	45	-27	-27 to 105	**m=-3** ($\Delta\phi_{st}$=**-15**) m=+3 ($\Delta\phi_{st}$=15) **m=-5** ($\Delta\phi_{st}$=**95**) m=-2 ($\Delta\phi_{st}$=110)	151 612 763 913 1064 1211 1238	-- -- **m=-3.00** m=+4.01 -- -- **m=-4.99**	•Cut #1 is slightly smaller than cut #2. •Pressure peaks listed from most to least prominent.
	DIA/ DAGO	89	135	105 to 160	m=-5 ($\Delta\phi_{st}$=95) m=-2 ($\Delta\phi_{st}$=110) **m=+1** ($\Delta\phi_{st}$=**125**) m=+4 ($\Delta\phi_{st}$=140) m=+7 ($\Delta\phi_{st}$=155)	151 612 763 913 1064 1211 1238	**m=+1.00** m=+2.91 -- -- m=-4.08 -- --	

APPENDIX F--ANALYSES OF UNSTEADY EVENTS

Section	Analyzer	Phase Analysis				Blade Vib. Analysis		comments
		f_p [Hz]	$\Delta\phi_{st}$ [deg]	$\Delta\phi_{st}$ range [deg]	Possible m-values	f_b [Hz]	Possible m-values	
14,000 rpm Rot. Stall, (Occur-rence D, Cut #1)	DIA/ DAGO	134	129	129 to 151	m=-2 ($\Delta\phi_{st}$=110) m=+1 ($\Delta\phi_{st}$=125) m=+4 ($\Delta\phi_{st}$=140) m=+7 ($\Delta\phi_{st}$=155)	151 612 763 913 1064 1211 1238	-- m=-2.00 -- -- m=+5.01 -- --	•Cut #1 is slightly smaller than cut #2.
14,000 rpm Rot. Stall, (Occurrenc e D, Cut #2)	DIA/ DAGO	45	-41	105 to 160	same as for cut #1			•Cut #2 is slightly larger than cut #1. •Pressure peaks listed from most to least prominent.
		86	146	99 to150	same as for cut #1	151 612 763 913 1064 1211 1238	m=+0.99 m=+2.92 -- -- m=-4.09 -- --	

APPENDIX F--ANALYSES OF UNSTEADY EVENTS

Section	Analyzer	Phase Analysis				Blade Vib. Analysis		comments
		f_p [Hz]	$\Delta\phi_{st}$ [deg]	$\Delta\phi_{st}$ range [deg]	Possible m-values	f_b [Hz]	Possible m-values	
14,000 rpm Rot. Stall, (Occur-rence D, Cut #2)	DIA/ DAGO	130	138	123 to 166	m=-2 ($\Delta\phi_{st}$=110) m=+1 ($\Delta\phi_{st}$=125) m=+4 ($\Delta\phi_{st}$=140) m=+7 ($\Delta\phi_{st}$=155)	151 612 763 913 1064 1211 1238	-- m=-2.02 -- -- m=+5.00 -- --	•Cut #2 is slightly larger than cut #1. •Pressure peaks listed from most to least prominent.
	DIA/ DAGO	38	104	98 to 183	same as above	151 612 763 913 1064 1211 1238	-- -- m=-3.03 m=+3.98 -- m=-4.91 m=-5.02	

APPENDIX F--ANALYSES OF UNSTEADY EVENTS

Section	Analyzer	Phase Analysis				Blade Vib. Analysis		comments
		f_p [Hz]	$\Delta\phi_{st}$ [deg]	$\Delta\phi_{st}$ range [deg]	Possible m-values	f_b [Hz]	Possible m-values	
14,000 rpm Rot. Stall, (Occur-rence D)	FFT Analyzer	45	-5		m=-3 ($\Delta\phi_{st}$=-15) m=+3 ($\Delta\phi_{st}$=15)			•Coherence = 1.0. •Pressure peaks listed from lowest to highest frequency.
	FFT Analyzer	81	124		m=-2 ($\Delta\phi_{st}$=110) m=+1 ($\Delta\phi_{st}$=125) m=+4 ($\Delta\phi_{st}$=140)			•Coherence = 1.0
	FFT Analyzer	87	147		m=+4 ($\Delta\phi_{st}$=140) m=+7 ($\Delta\phi_{st}$=155)			•Coherence = 1.0

ANALYSIS OF ROTATING STALL

Section	Analyzer	Phase Analysis				Blade Vib. Analysis		comments
		f_p [Hz]	$\Delta\phi_{st}$ [deg]	$\Delta\phi_{st}$ range [deg]	Possible m-values	f_b [Hz]	Possible m-values	
14,000 rpm Rot. Stall, (Occur-rence D)	FFT Analyzer	93	126		m=-2 ($\Delta\phi_{st}$=110) m=+1 ($\Delta\phi_{st}$=125) m=+4 ($\Delta\phi_{st}$=140)			•Coherence = 1.0 •Pressure peaks listed from lowest to highest frequency.
	FFT Analyzer	132	122		same as above			•Coherence = 1.0

LIST OF REFERENCES

LIST OF REFERENCES

Abdel-Hamid, A. N., et al. "Unsteady Flow Characteristics in a Centrifugal Compressor with Vaned Diffuser," ASME Paper No. 87-GT-142, 1987.

Ariga, I., et al. "Inducer Stall in a Centrifugal Compressor with Inlet Distortion," ASME Paper No. 86-GT-139, 1986.

Chen, Y. N., et al. "On the Nature of Rotating Stall in Centrifugal Compressors with Vaned Diffusers. Part II: Karman Vortices as the Controlling Mechanism," Proceedings of the 1987 Tokyo International Gas Turbine Congress, Vol. II, Tokyo Japan, October 26-29, 1987, JSME Paper No. 87-TOKYO-IGTC-23.

Chen, Y. N., et al. "The Vortex-Filament Nature of Reverse Flow on the Verge of Rotating Stall," ASME Paper No. 88-GT-120.

Chen, Y. N., et al. "The Vortex-Filament Nature of Reverse Flow on the Verge of Rotating Stall," Transactions of the ASME, Vol. 111, October 1989, pp. 450-461.

Chen, Y. N., et al. "Experimental Investigation of the Longitudinal-Vortex-Nature of Rotating Stall in Vaneless Diffusers of Centrifugal Compressors," ASME Paper 91-GT-99, 1991(a).

Chen, Y. N., et al. "The Rossby Waves of Rotating Stall in Impellers, Part I: Theoretical Background of the Rossby Waves in Blade Channels," JSME Paper 91-YOKOHAMA-IGTA-91(b).

Chen, Y. N., et al. "The Rossby Waves of Rotating Stall in Impellers, Part II: Application of the Rossby-Wave Theory to Rotating Stall," JSME Paper 91-YOKOHAMA-IGTA-92 (c).

Chen, Y. N., et al. "The Vortex Behavior of the Rotating-Stall Cell of a Centrifugal Compressor with Vaned Diffuser," ASME Paper 92-GT-66.

Cumpsty, N. A. Compressor Aerodynamics, Essex, England: Longman Scientific & Technical, 1989.

Fringe, P. and R. Van Den Braembussche. "Distinction between Different Types of Impeller and Diffuser Rotating Stall in a Centrifugal Compressor with Vaneless Diffuser," ASME Paper 83-GT-61, 1983.

Haupt, U., K. Bammert, and M. Rautenberg. "Blade Vibration on Centrifugal Compressors--Fundamental Considerations and Initial Measurements," ASME Paper 85-GT-92, 1985a.

Haupt, U., K. Bammert, and M. Rautenberg. "Blade Vibration on Centrifugal Compressors--Blade Response to Different Excitation Conditions," ASME Paper 85-GT-93, 1985b.

Haupt, U., et al. "Investigation of Unsteady Flow in a Centrifugal Compressor with Vaneless Diffuser," Proceedings of the Sixth International Conference for Mechanical Power Engineering, Vol. 5, Cairo, Egypt, December 27-30, 1986.

Haupt, U., et al. "On the Nature of Rotating Stall in Centrifugal Compressors with Vaned Diffusers, Part I: Detection of Reverse Flow," Proceedings of the 1987 Tokyo International Gas Turbine Congress, Vol. II, Tokyo Japan, October 26-29, 1987, JSME Paper No. 87-TOKYO-IGTC-23, 1987b.

Haupt, U., et al. "Unsteady Flow in a Centrifugal Compressor with Different Types of Vaned Diffusers," ASME Paper No. 88-GT-22, 1988.

Haupt, U., et al. "Investigation on Rotating Stall Phenomenon of Multitudinous Stall Cells and Its Impact on Blade Excitation of Centrifugal Compressor Impeller," Interfluid, 1st International Congress on Fluid Handling Systems, Essen, Fed. Rep. of Germany, Sept. 10-12, 1990.

Jin, D., et al. "Blade Excitation by Circumferentially Asymmetric Rotating Stall in Centrifugal Compressors," ASME Paper 92-GT-148, 1992a.

Jin, D., et al. "Excitation of Blade Vibration Due to Surge of Centrifugal Compressors," ASME Paper 92-GT-149, 1992b.

Kämmer, N. and M. Rautenberg. "An Experimental Investigation of Rotating Stall Flow in a Centrifugal Compressor," ASME Paper 82-GT-82, 1982.

Kämmer, N. Untersuchung der Strömung durch eine Radialverdichterstufe im Bereich der Ablösegrenze, Doctoral Dissertation, University of Hannover, Hannover, Germany, 1984.

Kämmer, N. and M. Rautenberg. "A Distinction Between Different Types of Stall in Centrifugal Compressor Stage," ASME Paper No. 85-GT-194, 1985.

Kubo, T. and S. Murata. "Unsteady Flow Phenomena in Centrifugal Fans," Bulletin of the JSME, Vol. 19, No. 135, September 1976, pp. 1039-1046.

Lennemann, E. and J. H. G. Howard. "Unsteady Flow Phenomena in Rotating Centrifugal Impeller Passages," Transactions of the ASME: Journal of Engineering for Power, January 1970, pp. 65-71.

Ligrani, P. M., et al. "Rotating Stall Measurements in the Vaneless Diffuser of a Radial Flow Compressor," ASME Paper No. 82-GT-257, 1982.

Mizuki, S., et al. "Reversed Flow Phenomena within Centrifugal Compressor Channels at Lower Flow Rate," ASME Paper No. 76-GT-86, 1976.

Mizuki, S., et al. "Investigation Concerning Rotating Stall and Surge Phenomena within Compressor Channels," ASME Paper No. 78-GT-9, 1978.

Pampreen, R. C. Compressor Surge and Stall, Norwich, Vermont: Concepts ETI, Inc., 1993.

Roth, G. "Unsteady Pressure Measurements in a Rotating Centrifugal Impeller," ASME paper 92-GT-152.

Seidel, U. et al. "Experimental Investigation of Rotating Stall Behavior Influenced by Varying Design and Operation Parameters of Centrifugal Compressors, JSME Paper 91-YOKOHAMA-IGTC-93, 1991a.

Seidel, U., et al. "Rotating Stall Flow and Dangerous Blade Excitation of Centrifugal Compressor Impeller--Part 1: Phenomena of Large-number Stall Cells," ASME paper 91-GT-102, 1991b.

Wachter, J. and K.-H. Rohne, "Centrifugal Compressor Surge Behavior," ASME Paper No. 84-GT-91, 1984.